MOLECULAR DYNAMICS SIMULATION STUDIES OF IONIC LIQUIDS ELECTROLYTES FOR LITHIUM ION BATTERIES

by

Zhe Li

A dissertation submitted to the faculty of
The University of Utah
in partial fulfillment of the requirements for the degree of

Doctor of Philosophy

Department of Materials Science and Engineering

The University of Utah

December 2012

The University of Utah Graduate School

STATEMENT OF DISSERTATION APPROVAL

The dissertation of Zhe Li

has been approved by the following supervisory committee members:

Dmitro Bedrov	, Chair	**10/26/2012** Date Approved
Feng Liu	, Member	**10/26/2012** Date Approved
Valeria Molinero	, Member	Date Approved
Ling Zang	, Member	**10/26/2012** Date Approved
Jules John Magda	, Member	Date Approved

and by **Feng Liu** , Chair of

the Department of **Materials Science and Engineering**

and by Charles A. Wight, Dean of The Graduate School.

ABSTRACT

Molecular dynamics (MD) simulations of various room temperature ionic liquids (RTILs), RTIL/lithium salt mixtures, and RTIL/lithium salt/organic solvents mixtures have been conducted using a well-established polarizable force field which demonstrated unprecedented accuracy and transferability in simulations of liquids, electrolytes, and polymers. The influence of inclusion atom polarizability on the accuracy of properties predicted from MD simulations of RTILs has been systematically investigated. Simulations of RTILs in which the atom-based polarizability was set to zero for all atoms (nonpolarizable model) resulted in changes in thermodynamic and dynamic properties from those predicted by the polarizable force field (polarizable model). Investigation of structural and dynamical correlations using both the polarizalbe and nonpolarizable model allowed us to obtain a mechanistic understanding of the influence of polarization on dynamics in the RTILs investigated. MD simulations of N-methyl-N-propylpyrrolidinium(pyr_{13}) bis(trifluoromethanesulfonyl)imide(Ntf_2) ionic liquid [pyr_{13}][Ntf_2] mixed with [Li][Ntf_2] salt have been conducted at 363 K and 423 K. Mixture simulations with lithium salt mole fractions between 0% and 33% at 363 K and 423 K yield densities, ion self-diffusion coefficients, and ionic conductivities in very good agreement with available experimental data. The concentration dependence of Li^+ solvation structure, conductivity, and diffusion mechanism has been successfully investigated. The organic solvents acetonitrile (ACN) and ethylene carbonate (EC) were

added into the $[pyr_{13}][Ntf_2]/[Li][Ntf_2]$ mixtures at two concentrations (20 mol% and 40 mol%). Ion mobility was found to be improved in the diluted electrolytes. In addition, EC and ACN molecules were found to be able to influence the coordination structure and diffusion mechanism of Li^+ cations. The interfacial structures of the mixtures near charged and uncharged graphite electrode have been exposed as well, using an electroactive interface molecular dynamics simulation methodology. Multilayer structures were observed near the atomically flat graphite electrodes. The orientations of the components in the mixtures near the charged and uncharged surface were discussed thoroughly.

Dedicated to all my family members

TABLE OF CONTENTS

LISTS OF TABLES

Table

ACKNOWLEDGMENTS

The author would like to gratefully acknowledge the enormous support from Dr. Dmitro Bedrov, Dr. Grant D. Smith, and Dr. Oleg Borodin for their teaching, guidance, patience, and help in completing this work. Thanks are also given to Dr. Justin B. Hooper, and Dr. Jenel Vatamanu for the helpful suggestions, opinions, and discussions. Helpful discussions from all colleagues in our group are highly appreciated as well.

I also would like to give my special thanks to the Department of Materials Science and Engineering of the University of Utah, especially to Professor Feng Liu for the great lectures.

Acknowledges are expressed for financial support from the U.S. Department of Energy through DE_ AC02-05CH11231 grant on PO No. 6838611 to University of Utah and ABR DOE program. An allocation of computer time from the Center for High Performance Computing at the University of Utah is acknowledged as well.

CHAPTER 1

INTRODUCTION

1.1. Energy Storage Technologies

Increasing demand for clean energy sources for households, industry, and vehicles which current rely on internal-combustion-engine as the power source, and global concerns about present energy situation have promoted the development of renewable energy technologies, such as wind power, solar power, and bioenergy. The key to the success of those alternative energy technologies is electrical energy storage. Current available electrical energy storage technologies include batteries, electrochemical capacitors, pumped hydro, compressed air, thermal energy storage, hydrogen, flywheels, and superconducting magnetic energy storage (SEMES).[1] However, capacitors and batteries, which minimize energy losses, are the most efficient and widely used electrochemical devices. In particular, lithium batteries are known to have the highest energy efficiency and their development is in an advanced state, as compared to other technologies.[2]

1.2. Batteries

A typical battery consists of electrodes (cathode and anode), a separator (electrolyte), and current collectors (Fig. 1-1). The performance of batteries is strongly dependent on

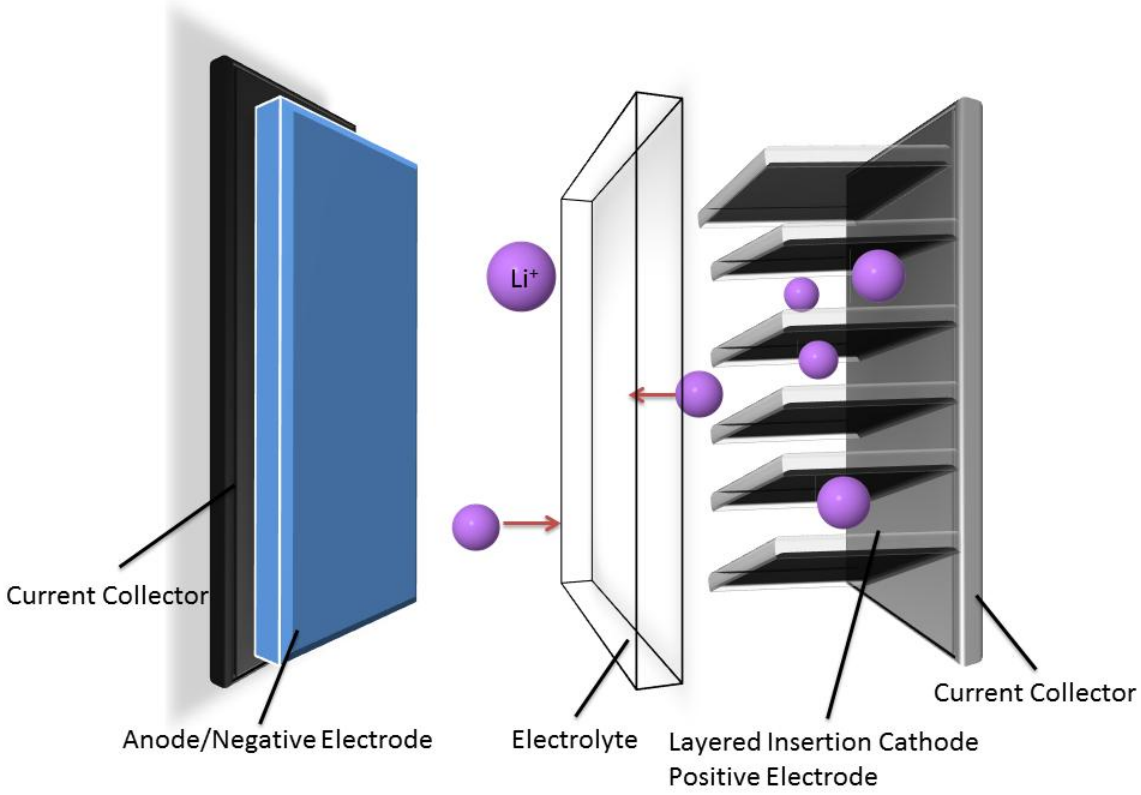

Figure 1-1. Schematic of the components of a lithium ion battery.

the materials and properties of the electrodes and electrolytes. Traditionally, batteries are classified into two broad categories: primary batteries that irreversibly transform chemical energy to electrical energy; secondary batteries that can be recharged.

1.2.1. Lithium Metal as Electrode for Batteries - Lithium Batteries

With a very high specific capacity (3.86 Ah g^{-1}, 7.23 Ah cm^{-3}) and favorable thermodynamic potential Li metal is considered as the optimal anode materials for a battery. Batteries using Li metal as anode can reach a potential in excess of 4 V.[3,4] Primary batteries with Li metal anode are of numerous advantages, including but not limited to, high voltage, high specific energy, high energy density, and wide operating

temperature range.[3,4] Using of lithium metal as anode in rechargeable batteries, however, is problematic. First, dendrite growth at the anode when discharging can result in significant capacity loss.[5,6] Second, the dendrites can possibly reach the cathode leading to internal short-circuit and hence explosion or flaming. Finally, it is difficult to form stable solid electrolytes interphase/interface (SEI) layer on lithium metal in rechargeable batteries.[7] SEI layers are passivation films which formed at the anode and prevent further decomposition of electrolytes at the electrode. Due to the risk of fire, rechargeable batteries using lithium metal as anode were recalled by the producers and all products were terminated in 1989.[8]

1.2.2. Lithium-Ion Batteries – Secondary Lithium Batteries

Rechargeable batteries in which lithium metal were used as electrode pose safety issues. As a result, efforts were made to develop batteries in which both electrodes are made of materials containing lithium ions. Li metal is no longer present in the battery. Li+ ions are instead shuttled through the electrolyte between the intercalated electrodes (Figure 1-1). This type of rechargeable batteries was initially named as "Rocking-chair," "shuttle-cock," or "swing batteries,"[9-11] and later called lithium-ion (Li-ion) batteries. LIBs have the highest energy and power density among rechargeable batteries.[12] After more than 20 years development, LIBs have become indispensable power source for portable electronics (cell phones, personal data assistants and laptops).[13] Their applications in military electronics such as radios, mine detectors and thermal weapon sights also grow rapidly and become significant. In recent years, large-scale LIBs are used in space shuttles, satellites, and electric vehicles as well.[14] Particularly, a recent report of their implementation in a commercial plug in electric vehicles (PHEV) makes

LIBs a promising power sources for PHEV, hybrid electric vehicles (HEV) and the only power for future electric vehicles (EV).[15]

Currently, graphite is widely used as anode for LIBs. Cathode materials are typically made of transitional metal oxide ($LiFePO_4$, $LiMn_2O_2$, or $LiMO_2$, M=Co, Ni). The electrodes are separated by electrolytes which shuttle the Li^+ ions between the intercalation electrodes, thus avoiding the growth of dendrites at the anode surface.[16] The charge/discharge reactions are given by eq 1-1 and 1-2. Li^+ ions moves to the anode during charging and to the cathode when discharging (Figure 1-2). While LIBs possess some merits like high specific energy (~ 150 Wh Kg^{-1}) and energy density (~400 Wh L^{-1}), low self-discharge rate (2-8% per month), long cycle life (more than 1000 cycles), and broad temperature range of operation (-10 ℃ to 50 ℃), there are still some drawbacks[3] that hinder their implementation in more demanding area, such as in energy storage and sustainable transports, where low-cost, reliable large-scale batteries pack is commonly required.[2] The main disadvantage is the safety risk in using large-scale lithium battery pack in which organic liquids electrolyte is used. Moreover, mechanical short circuits or internal short circuits in the batteries may result in localized heating and when the temperature is above 130 ℃ to 150 ℃, exothermic chemical reactions occur in the

Cathode: $$\mathrm{Li}MO_2 \underset{\text{discharging}}{\overset{\text{charging}}{\rightleftharpoons}} Li_{1-x}MO_2 + xLi^+ + xe^- \qquad \text{Eq (1-1)}$$

Anode: $$C + xLi^+ + xe^- \underset{\text{discharging}}{\overset{\text{charging}}{\rightleftharpoons}} Li_xC \qquad \text{Eq (1-2)}$$

Figure 1-2. Electrode and cell reactions in a Li-ion battery.

batteries causing a rapid increase of the temperature and hence thermal runaway.[17-20]

1.2.3. Electrolytes for Lithium-ion Batteries

Electrolytes in LIBs act as the medium for the Li^+ ion transfer but they are electron insulators. [21] Liquid, polymer, gel and ceramic materials are the four principal electrolytes used in Li-ion batteries.[3] Typically, liquid electrolytes are a mixture of organic solvents, such as ethylene carbonate (EC), dimethyl carbonate (DMC), and diethyl carbonate (DEC), doped with lithium salt, such as $LiPF_6$, $LiBF_4$ or $LiClO_4$. Li-ion batteries using this type of electrolyte are well commercialized and dominate the consumer-electronics market. The ionic conductivity of liquid electrolyte is temperature dependence and is around 10 $mS*cm^{-1}$ at room temperature.[12] Nonflammable Inorganic liquid electrolyte based on $LiAlCl_4$ and SO_2 exhibits a good room-temperature ionic conductivity (70 $mS*cm^{-1}$), but its low electrochemical window significantly limits the applications.[22,23] Recently, ionic liquids-based electrolytes which is free of any molecular solvent have been widely investigated and considered as an ideal candidate for next generation (novel) liquid electrolytes.[2,13,24-27] Aiming at improving the safety of LIBs, solvent-free polymer electrolytes are extensively investigated and currently under development. Polymer electrolytes are prepared by directly dissolving lithium salt in a high molecular weight polymer, for instance, poly(ethylene oxide)(PEO).[28-30] The solid-state polymer electrolytes allow the use of lithium metal at negative electrode by repressing dendrite growth and safe operation of batteries using this type of solid-state electrolytes has been demonstrated.[2] Unfortunately, batteries using polymer electrolytes have unacceptable low ionic conductivity (~10^{-4} $mS*cm^{-1}$ in PEO matrix) at room temperature,[12] and can perform well only at temperature above 50 ℃, which seriously

limits their range of application. Introduction of oxide particles (Al_2O_3, TiO_2, SiO_2, or ZrO_2) improves the conductivity and Li-ion transference number,[31-33] but they are still far below the values in OLEs. The conductivity of polysiloxanes modified PEO-based electrolytes can reach as high as ~1 $mS*cm^{-1}$ at room temperature.[34-37] Gel polymer electrolytes, which are regarded as an intermediate state between liquid and solid polymer electrolytes, are prepared by mixing organic solvents and lithium salts with a small portion of high polymer. The polymer in gel electrolytes serves as the mechanical matric which is usually either soaked with or swollen by the liquid solutions. Ionic conductivity of gel polymer electrolytes at room temperature typically falls into the range from 0.1 to 1 $mS*cm^{-1}$.[38] Ceramic electrolytes are solid state electrolytes made of solid-state inorganic materials. Room temperature conductivity obtained from typical ceramic solid electrolytes is from 0.1 to 10-5 $mS*cm^{-1}$.[39] and efforts are still needed for their implementation for Li-ion batteries.

1.2.4. State-of-the-Art Liquid Electrolytes for Li-ion Batteries

Current state-of-the-art liquid electrolytes used in most commercial Li-ion batteries are organic liquid electrolytes (OLEs) and obtained by dissolution of lithium salts in molecular solvents.

An ideal solvent for LIBs should meet the criteria list below:

1. Be able to dissolve sufficient amount of lithium salt, in other words, the solvent should have a high dielectric constant (ε).
2. Be able to efficiently transport the charge carrier – Li+ ions, that is, the solution must be of low viscosity (η).
3. Remain inert to all cell components, especially the charged surfaces of electrodes.

4. Remain liquid phase within a wide operation temperature range

The nature of anodes (reductant) and cathodes (oxidant) materials rules out most organic solvents which have active protons. Therefore, qualified electrolyte solvents can only be those with polar groups such as carbonyl (C=O), nitrile (C≡N), sulfonyl (S=O), and ether-linkage (-O-). Carbonates are good solvents for Li salts and have oxidation/reduction potential 4.7 V/1.0 V (referred to Li^+/Li^0).[21, 40-43] The low viscosity of carbonate solvents enables fast diffusion of working cation (Li^+ ions in LIBs).

An ideal electrolyte for LIBs requires a large electrochemical window E_g, as well as[7]

- Stable SEI layers on electrodes which usually change their volume during cycling.
- A minimum 0.1 mS*cm-1 ionic conductivity contributed by Li+ ions only.
- An electronic conductivity below 10-7 mS*cm-1.
- Li+ ion transference number = 1.
- High chemical stability at elevated temperatures and under high power.
- Chemical stability with respect to the electrode, which is realized by forming rapidly a SEI layers.
- Nonflammable and nonexplosive when overheated.
- Low cost and low toxicity.

$LiPF_6$ dissolved in a mixture of carbonates such as EC, DMC, diethyl carbonate (DEC), propylene carbonate (PC), or ethylmethyl carbonate (EMC) achieved overall ionic conductivity above 1 mS cm^{-3} and lithium ion transference number about 0.35.[21] A stable Li^+ ion conductive SEI film formed by complex and complicated reductive reactions of electrolyte at the anode prevents further decomposition of the electrolyte.[44,45] While being widely used, OLEs are not perfect and of drawbacks which limit the

applications of LIBs and anxiously need to be replaced. OLEs usually suffer from high flammability with flash points below 30 ℃.[46] The hygroscopic $LiPF_6$ can autocatalytic decompose into LiF and PF_5 which produces hydrofluoric acid (HF) when explored to water and reacts with carbonate at temperature above 60 ℃.[47] This makes the working and storage environment of the electrolyte and hence the batteries fastidious. OLEs cannot be effective operated at temperature below -10℃ due to a rapid increase in viscosity of the OLEs. The batteries with OLEs are not able to work properly at temperature higher than 90 ℃ either because of low thermal stability of the SEI layer and other components at high temperatures.[21]

1.2.5. Ion Transport Properties in Organic Liquid Electrolytes

Since ions are the only charge carrier in electrolytes their transport in the solution is crucial to the performance of the batteries. A two-step process is usually used to describe the transport of ions: (1) the lithium salt is solvated and dissociated by polar solvent molecules; (2) transport of the solvated ions in the solution. Various modeling and experiments[48-52] support the conclusion that the small radius of a Li+ ion allows no more than four solvent molecules in its first coordination shell. Molecular Dynamics simulation also revealed that migration of Li+ ions in an electrolyte solution is contributed equally by: 1) the Li+ ions move together with the solvent molecules in its shell; 2) Li+ ion change solvent molecules in its first coordination shell with solvents from the outer shells.[52] Surrounded by neutral solvent molecules this cluster is still positively charged. Solvation, dissociation, and the subsequent migration of ionic clusters can be quantitatively reflected by accurate measurement of ionic conductivity σ:

$$\sigma = \sum_i n_i \mu_i Z_i \qquad (1-3)$$

where Z_i is the valence order of ionic species *i*, n_i and μ_i are the free ion number and the ionic mobility, respectively, and e is the unit charge of electrons. Ionic conductivity has been used as the standard for any prospective electrolytes due to its easy measurement. The measured conductivity is a result of the overall migration of both anions and cations in OLEs. However, for lithium ion batteries, only contribution from Li^+ matters, and thus, lithium ion transference number (t_{Li}) which is defined as following is more important:

$$t_{Li} = \frac{\mu_i}{\sum_i \mu_i} (1-4)$$

Typically, t_{Li} ranges from 0.20 to 0.40, indicating that anions are more mobile in OLEs than the solvated Li^+.

1.2.6. Interface between Electrolyte and Electrode

The operation of lithium ion batteries largely depends on the properties of the interface between electrolyte and electrodes. Decomposition of the electrolyte at the electrode surface will result in the solid electrolyte interphase/interface (SEI) layers that ultimately passivate the electrodes and prevent further decomposition of the electrolytes. The structure of the SEI layers is reported to depend on the composition of the composition of the lithium solvation shell,[53 - 58] highlighting the importance of its characterization near the interface. Moreover, the operation of Li-ion battery requires Li^+ to be transported not only through the electrolyte but also the electrode/electrolyte interface during charging/discharging process. The latter is more essential for the performance of Li-ion batteries and much more complicated. It is therefore clear that

elucidating the properties of the interface between the electrolyte and the electrode is important to understanding the behavior of Li-ion batteries and ultimately to improving cycle life and minimizing the resistance to ion transport.

1.3. High-performance Rechargeable Batteries

The emerging market for batteries in renewable energy technologies and advanced transport technologies is poised to take off, and with the potential to dwarf the consumer-electronics market. In particular, the demands of suitable battery packs for PHEV, HEV and EV are increasing. The cost and performance, in terms of safety, power and energy density, and operation temperature range, of current LIBs is however far away behind the requirements for those demands, and therefore, low-cost, safe, rechargeable batteries of high voltage, capacity, and rate capability are strongly desired. High-energy and high-power batteries (advanced batteries) will require high cell voltage by using extremely active anode and cathode materials that can operate well over a large potential window. Current 3.6 V batteries with $LiCoO_2$ as cathode have an energy density lower than the need for plug-in hybrid electric vehicle (PHEV), leading to numerous researches on finding suitable alternative electrode materials which work well at voltage above 4.3 V. A higher energy density means reduced size and cost of batteries and hence the overall price of the vehicle. Another challenge for advanced batteries is developing suitable electrolytes because, unfortunately, the current state-of-the-art OLEs do not work properly at high voltage and elevated temperature. What is more, the OLEs pose some safety risk, making them not suitable for large-scale battery pack which is of more problems in thermal management. There are, however, quite a limited number of materials available for choices among which a significant amount of attention has been

focused on ionic liquid based electrolytes. The nonflammable and ionic liquids with negligible volatility may help to solve the problems in current OLEs.

1.4. Ionic Liquids

1.4.1. Overview

Ionic liquids (ILs) are salts which are composed solely of ions or short-lived ion pairs with low melting point (generally below 100 ℃) and those with melting temperature lower than room temperature are called room temperature ionic liquids (RTILs). ILs usually consist of asymmetric organic cations such as imidazolium or pyrrolidinium cations and inorganic or organic anions, including Cl^-, Br^-, NO_3^-, BF_4^-, PF_6^-, $B(CN)_4^-$ (TCB), $C(CN)_3^-$(TCM), $C(CN)_2^-$(DCA), CH_3CO_2-, CF_3SO_3-, $N(SFO_2)_2^-$(FSI) and $N(CF_3SO_2)_2^-$(NTF_2). Figure 1-3 shows some examples of typical IL cations and anions together with their abbreviations.

Negligible vapor pressure,[59] good thermal and electrochemical stability,[60] good dissolution with many organic and inorganic compounds, low flammability,[61] and a wide variety of possible anions and cations are a few examples of the unique characteristics that make ILs exciting alternative materials for many applications. Importantly, the properties of ILs can be tailored for specific chemical (separation, catalysis, reactions, propellants, explosives) or electrochemical (battery, actuators, supercapcacitors) applications by tuning the combination of cations and anions to achieve the desired thermodynamic, solvating, and transport properties. For example, higher charge delocalization improves ion transport,[62, 63] and the length and nature of substituted groups affect melting (Tm) and glass transition (T_g) temperatures as well as thermal stability.[64,65]

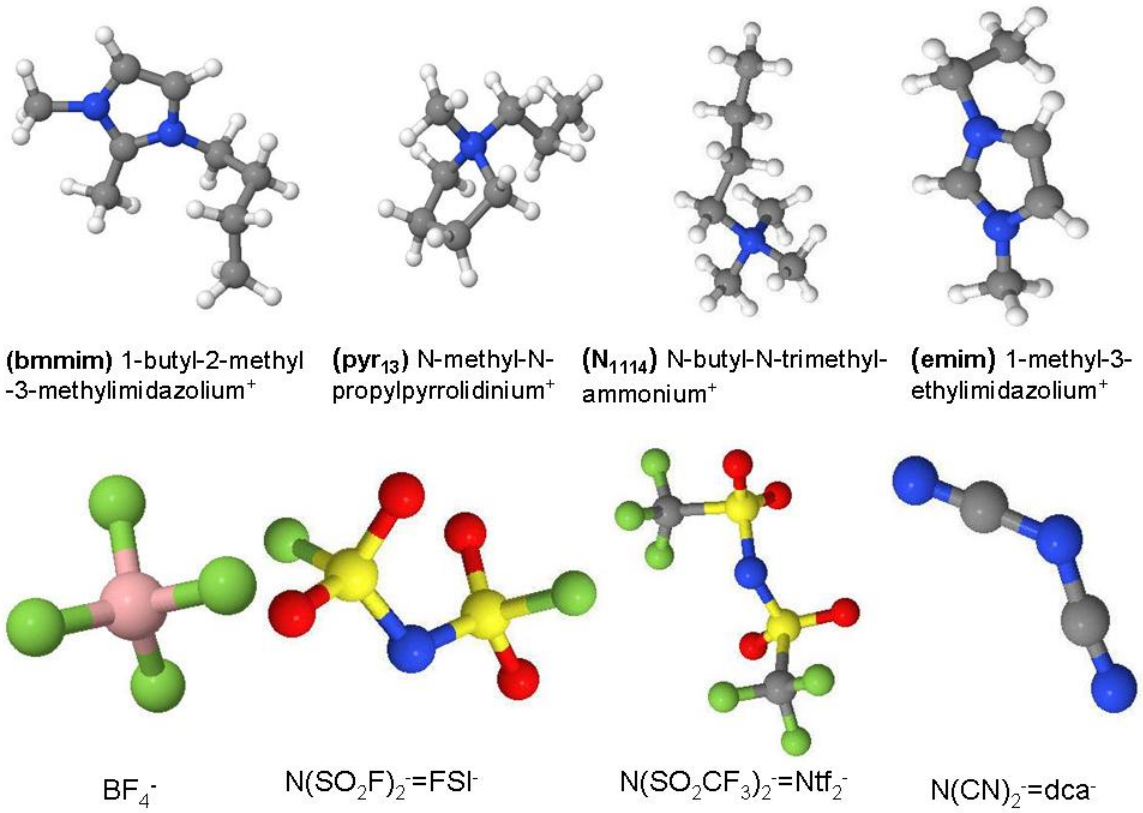

Figure 1-3. Molecular structure of cations and anions of common ionic liquids.

1.4.2. Applications of Ionic Liquids

Due to the favorable properties mentioned above, chemical and electrochemical applications of RTILs have been growing rapidly over the past decades, making them an area of great interest. Biphasic systems for separation, solvents for synthetic and catalytic applications,66 lubricants,[67,68] lithium batteries,[69-72] actuators,[73,74] sensors,[75] reaction media[76] replacement of conventional solvents,[77] active pharmaceutical ingredients,[76] and hypergolic propellants[78] are a few examples. Particularly, the unique properties of RTILs and their ability to dissolve lithium salts make them ideal candidate for lithium ion (secondary) lithium battery electrolyte.[79]

1.4.3. Ionic Liquids Electrolytes (ILEs) for Li-ion Batteries

Free of any molecular solvent, ionic liquids mixed with Lithium salt (LiX) have been widely investigated as electrolytes for electrochemical device,[2,24] including lithium batteries. The negligible vapor pressure of ILs may make capsule of the batteries easy. What's more, ILs can be easily dried, making the manufacture process more cost efficient, both time and money. The most favorable properties of ILEs are their nonflammability and exceptional electrochemical stability. Replacement of the flammable and volatile OLEs with ILEs will enable the batteries to operate safely in large-scale application, with high-voltage electrodes, and at elevated temperatures. Thus, both industrial and academic laboratories[69, 72, 80, 81] have taken efforts in testing ILEs as new electrolytes for LIBs.

1.5. Interface Between Electrode and Electrolyte

Electrolyte/electrode interface is central to the performance and operation of lithium ion batteries. Formation of stable solid electrolyte interface (SEI) layers at the electrode surface by oxidation or reduction of electrolyte will passivate the electrodes and protect the electrolytes from further decomposition.[82-86] It was reported that the structure of SEI depends on the composition of the lithium solvation shell, making characterization and understanding of lithium coordination near surface important. In addition, the operation of LIBs is based not only on the transport of Li^+ cations through electrolytes but also through the electrode/electrolytes interface, giving rise to the importance of understanding the properties of the interface. Classical MD simulation studies of ion transport and structure in ILs doped with lithium salts as bulk electrolytes have been widely performed and have led to an improved understanding of Li^+ solvation and transport mechanism. In contrast, simulations of ILs mixed with lithium salt at the

interface with electrodes have not been reported. Recently, a few literatures reported MD simulations studies of mixed carbonate electrolytes at the electrode surfaces.[87,88] These studies indicate that the composition of the carbonate electrolyte and lithium coordination structure at the electrode surface can differ significantly from the bulk. In addition, extensive MD simulations were conducted in investigating the electric double layer structure and differential capacitance of the ionic liquid-electrode interface.[89-93]These studies provide valuable insight into the properties of ILs/electrode interface. However, none of them has been extended to ILEs that would include investigation of the influence of the electrode potential on the structure of electrolyte near surface, lithium solvation shell, ion aggregation, ion surface enrichment, and so on. It is then clear that elucidating the properties of the interface between the ILEs and the electrode is important to understanding the behavior of IL-based lithium ion batteries and, ultimately, improving the performance of such novel lithium ion batteries.

1.6. Dissertation Overview

The research in this dissertation has been to explore, by molecular dynamics (MD) simulation method, the thermodynamics, structural, and transport properties of ionic liquids and their mixtures with organic solvents doped with lithium salts. In particular, the work is focused on the micro-structure and transport of ions in the mixture which are limited reported in literatures. These data, however, are crucial for developing ionic liquid based electrolytes with acceptable performance, and ultimately high performance lithium ion batteries.

Accurate prediction of any properties of materials from MD simulations is extremely depending on the quality of the force field employed. Recently, an Atomistic Polarizable

Potential for Liquids, Electrolytes, & Polymers (APPLE&P) developed in our group demonstrated accurate description of thermophysical and transport properties for a large number of ILs. Moreover, the APPLE&P database shows a high degree of transferability. The unprecedented accuracy and transferability of this force field raise a fundamental question: What role does the inclusion of polarizability play in the success of the APPLE&P force field in prediction the dynamics accurately? Thus, in first, the influence of many-body polarization on several important properties of a series of ILs, as predicted from MD simulations, is systematically investigated in this work. The role of polarization playing on predicting representative structural, thermodynamic, and dynamic properties of selected ILs are thoroughly studied by comparing results from MD simulations using the polarizable APPLE&P force field and nonpolarizalbe version of the APPLE&P force field in which polarization interactions were simply turned off (i.e., atom-based dipole polarizabilities were set to zero).

Utilizing the transferable quantum-chemistry-based APPLE&P force field, extensive MD simulations were also conducted to calculate the thermodynamics, transport, and structural properties of $[pyr_{13}][Ntf_2]$ IL and its mixture with $[Li][Ntf_2]$ at different concentrations. In particular, the concentration dependence of lithium solvation structure is elucidated in such mixtures. Ternary pyrrolidinum-based ionic liquid electrolytes involving organic solvents, such as ethylene carbonate (EC) and acetonitrile (ACN) are simulated as well and improved transport properties are observed in these ternary mixtures. Influence of those organic solvent on the lithium solvation structure and lithium diffusion mechanism is also reported and compared with neat electrolytes in this work. Moreover, MD simulations of the mixtures near graphite electrodes have also been

performed as a function of electrode potential. This work immediately proves that MD simulation is a good complementary to experimental study of IL and ILEs and the MD simulations using the APPLE&P force field is a powerful tool in exploring and understanding properties and performance of ILEs. This research will result in improved understanding of ILEs performance, and promote their development. The broader impact will be realized upon their implementation in large-scale, high-energy lithium ion battery pack which may become the power source for PHEV, EV, and other applications.

1.7. References

(1) Heinrich, M. *Executive Summary: Electric Energy Storage.* California Energy Commission Efficiency Committee Workshop, **2008**, CA.

(2) Armand, M.; Endres, F.; MacFarlane, D. R.; Ohno H.; Scrosati, B. *Nature Materials* **2009**, 8,621.

(3) Linden, D.; Reddy, T. B., Eds. *Handbook of Batteries*, 3rd edition, McGraw-Hill: New York, **2001**.

(4) Vincent, C. A.; Scrosati, B., Eds. Modern Batteries: An Introduction to*Electrochemical Power Sources*, 2nd edition, John Wiley & Sons, Inc.: New York, **1997**.

(5) Koch, V. R.; Young, J. H. *J. Electrochem. Soc.* **1978**, *125*, 1371.

(6) Yoshimatsu, I.; Hirai, T.; Yamaki, J. *J. Electrochem. Soc.* **1988**, *135*, 2422.

(7) Goodenough J. B.; Kin, Y. *Chem. Mater.* **2010**,22,587.

(8) Dominey, L. A. *Nonaqueous Electrochemistry*; Aurbach, D., Ed.; Marcel-Dekker: New York, 1999.

(9) Armand, M. *Materials for Advanced Batteries*; Murphy, D. W., Broadhead, J., Steele, B. C. H., Eds.; Plenum Press: New York, 1980, p 145.

(10) Ohzhku, T.; Ueda, A.; Nagayama, M. *J. Electrochem. Soc.* **1993**, *140*, 1862.

(11) Bittihn, R.; Herr, R.; Hoge, D. *J. Power Sources* **1993**, *43/44*, 223.

(12) Hayner, C. M.; Zhao, X.; Kung, H. H. *Annu. Rev. Chem. Biomol. Eng.***2012**, 3, 445.

(13) Guerfi, A.; Dontigny, M.; Charest, P.; Petitclerc, M.; Lagacé, M.; Vijh, A.; Zaghib, K. *J. Power Sources* 2010, 195, 845.

(14) Broussely, M. *11th International Meeting on Lithium Batteries,* Monterey, CA, June 23-28, 2002; Abstract No. 415; Electrochemical Society: Pennington, NJ.

(15) Anon., *The Ecnomist* **2009**, 390, 81.

(16) Scrosati, B. *Nat. Nanotechnol.* **2007**, *2*, 598.

(17) Balakrishnan, P. G.; Ramesh, R.; Kumar T. P. *J. Power Sources* **2006**, *155*, 401.

(18) von Sacken, U.; Nodwell, E.; Sundher, A.; Dahn, J. R. *Solid State Ionics* **1994**, *69*, 284.

(19) Levy, S. C.; Bro, P. *Battery Hazards and Accident Prevention*, Plenum Press: New York, 1994.

(20) Tobishima, S.; Yamaki, J. I. *J. Power Sources* **1999**, *882*, 81.

(21) Xu, K. *Chem. Rev.* **2004**, 104, 4303.

(22) Stassen, I.; Hambitzer, G. *J. Power Sources* **2002**, 105, 145.

(23) Zinck, L.;Borck, M.' Ripp, C.' Hambitzer, G. *J. Appl. Electrochem.* **2006**, 36, 1291.

(24) Galiński, M.; Lewandowski, A.; Stepniak, *I. Electrochim. Acta* **2006**, 51, 5567.

(25) Mum, J.; Jung, Y. S.; Yin, T.; Lee, H. Y.; Kin, H. *J. Power Sources* **2009**, 194, 1068.

(26) Egashira, M.; Tanaka-Nakagawa, M.; Watanabe, I.; Okada, S.; Yamaki, J. *J. Power Sources* **2006**, 160, 1387.

(27) Umebayashi, Y.; Mitsugi, T.; Fukuda, S.; Fujimori, T.; Fujii, K.; Kanaki, R.; Takeuchi, M.; Ishiguro, S. *J. Phys. Chem. B* **2007**, 111, 13028.

(28) Wright, P. V. Brit. *Polym. J.* **1975**, 7, 319.

(29) Armand, M. B.; Chagbano, J. M.; Duclot, M. J. *In Fast Ion Transport in Solid*; Vashishta, P., Mundy, J. N., Shenoy, G. K., EDs.; Elsevier N Holland: New York, **1979**; p131.

(30) Nishinoto, A.; Watanabe, M.; Ikeda, Y.; Kojiya, S. *Electrochim. Acta* **1998**, 43, 1177.

(31) Croce, F.; Appetecchi, G. B.; Persi, L.; Scrosati, B. *Nature* **1998**, 394, 456.

(32) Croce, F.; Curini, R.; Martinelli, A.; Persi, L.; Ronci, F.; Scrosati, B. *J. Phys. Chem. B* **1999**, 103, 10632.

(33) Croce, F.; Settimi, L. Scrosati, B. *Electrochem. Commun*. **2006**, 8, 364.

(34) Zhang ZC, SherlockD, West R, West R, Amine K, Lyons LJ. *Macromolecules 2003, 36, 9176.*

(35) Claes P, Simonis L, Glibert J. *Electrochim. Acta 1986, 31, 1525.*

(36) Williams ME, Lyons LJ, Long JW, Murray RW. *J. Phys. Chem. B 1997, 101, 7584.*

(37) Zhang, L. Z.; Zhang, Z. C.; Harring, S.; Straughan, M.; Butorac, R.; et al. *J. Mater. Chem.2008, 18, 3713.*

(38) Li, G.; Li, Z.; Zhang, P.; Zhang, H.; Wu, Y. *Pure Appl*. *Chem*. **2008**, 80, 2553.

(39) Nazri, G.; Pistoia, G.; Eds. *Lithium Batteries Science and Technology*, Springer Science+Business Media, LLC: New York, **2003**.

(40) Hayashi, K.; Nemoto, Y.; Tobishima, S.; Yamaki, J. *Electrochim*. *Acta* **1999**, 44, 2337.

(41) Imhof, R.; Novak, P. J. *Electrochem*. *Soc*. **1999**, 146, 1702.

(42) Egashira, M.; Takahashi, H.; Okada, S.; Yamaki, J. *J. Power Sources* **2001**, 92, 267.

(43) Zhang, X.; Kostecki, R.; Richardson, T. J.; Pugh, J. K.; Ross, P. N. *J. Electrochem. Soc.* **2001**, 148, A1341.

(44) Fong, R.; van Sacken, U.; Dahn, J. R. *J. Electrochem*. *Soc*. **1990**, 137, 2009.

(45) Yazami, R. *Electrochim*. *Acta* **1999**, 45, 87.

(46) Vogdanis, L.; Martens, B.; Uchtmann, H.; Hensel, F.;Heitz, W.Makromolekul. *Chem*. **1990**, 191, 465.

(47) Sloop, S. E.; Pugh, J. K.; Wang, S.; Kerr, J. B.; Kinoshita, K. Electrochem. *Solid-State Lett*. **2001**, 4, A42.

(48) Ue, M. *J. Electrochem. Soc.* **1994**, *141*, 3336.

(49) Wang, Y.; Nakamura, S.; Ue, M.; Balbuena, P. B. *J. Am. Chem.Soc*. **2001**, *123*, 11708.

(50) Blint, J. R. *J. Electrochem. Soc.* **1995**, *142*, 696.

(51) Yanase, S.; Oi, T. *J. Nucl. Sci. Technol.* **2002**, *39*, 1060.

(52) Borodin, O.; Smith, G. D. *J. Phys. Chem. B* **2006**, 110, 4971.

(53) Von cresce, A.; Xu, K. Solid-State Lett. **2001**, 14, A154.

(54) Xu, K.; von Cresce A.; Lee, U.; *Langmuir* **2010**, 26, 11538.

(55) Jung, Y. S.; Cavanagh, A. S.; Riley, L. A.; Kang, S. H.; Dillon, A. C.; Groner, M. D.; George, S. M.; Lee, S. H. *Adv. mater*. **2010**, 22, 2172.

(56) Mancini, M.; Nobili, F.; Dsoke, S.; D'Amico, F.; Tossici, R.; Croce F.; Marassi, R. *J. Power Sources* **2009**, 190, 141.

(57) Choi, N.; Yew, K.; Lee, K.; Sung, M.; Kim H.; Kim, S. *J. Power Sources* **2006**, 161, 1524.

(58) Choi, N.; Yew, K.; Kim, H.; Kim, S.; Choi, W. *J. Power Sources* **2007**, 172, 404.

(59) Xue, H.; Verma, R.; Shreeve, J. N. M. *J. Fluorine Chem*, **2006**, 127, 159.

(60) Egashira, M.; Todo, H.; Yoshimoto, N.; Morita, M.; Yamaki, J. I. *J. Power Sources* **2007**, 174, 560.

(61) Fox, D. M.; Awad, W. H.; Gilman, J. W.; Maupin, P. H.; De Long, H. C.; Trulove, P. C. *Green Chem*. **2003**, 5, 724.

(62) Tokuda, H.; Tabata, S. I.; Susan, M. A. B. H.; hayamizu, K.; Watanabe, M. *J. Phys. Chem. B* **2004**, 108, 11995.

(63) Tokuda, H.; Hayamizu, K.; Ishii, K.; Susan, M. A. B. H.; Watanabe, M. *J. Phys. Chem. B* **2004**, 108, 16593.

(64) Singh, R. P.; Verma, R. D.; Meshri, D. T.; Shreeve, J. M.; *Angew. Chem. Int. Ed.* **2006**, 45, 3584.

(65) Tokuda, H.; Hayamizu, K.; Ishii, K.; Susan, M. A. B. H.; Watanabe, M. *J. Phys. Chem. B* **2005**, 109, 6103.

(66) Forsyth, S. A.; Pringle, J. M.; MacFarlane, D. R. *Australian Journal of Chemistry* **2004,** *57*, 113.

(67) Jin, C. M.; Ye, C. F.; Phillips, B. S.; Zabinski, J. S.; Liu, X. Q.; Liu, W. M.; Shreeve, J. M. *Journal of Materials Chemistry* **2006,** *16*, 1529.

(68) Zeng, Z.; Phillips, B. S.; Xiao, J. C.; Shreeve, J. M. *Chemistry of Materials* **2008,** *20*, 2719.

(69) Shin, J. H.; Henderson, W. A.; Passerini, S. *Electrochemistry Communications* **2003,** 5, 1016.

(70) Galinski, M.; Lewandowski, A.; Stepniak, I. *Electrochimica Acta* **2006,** *51*, 5567.

(71) De Long, H. C.; Trulove, P. C.; Sutto, T. E. *Ionic Liquids as Green Solvents: Progress and Prospects* **2003,** *856*, 478.

(72) Garcia, B.; Lavallee, S.; Perron, G.; Michot, C.; Armand, M. *Electrochimica Acta* **2004,** *49*, 4583.

(73) Ding, J.; Zhou, D.; Spinks, G.; Wallace, G.; Forsyth, S.; Forsyth, M.; MacFarlane, D. In *Chem. Mater.*, **2003**; Vol. *15*, pp 2392.

(74) Cho, M. S.; Seo, H. J.; Nam, J. D.; Choi, H. R.; Koo, J. C.; Song, K. G.; Lee, Y. *Sensors and Actuators B: Chemical* **2006,** *119*, 621.

(75) Liu, Y.; Shi, L. H.; Wang, M. J.; Li, Z. Y.; Liu, H. T.; Li, J. H. *Green Chemistry* **2005,** *7*, 655.

(76) Hough, W. L.; Rogers, R. D. *Bull. Chem. Soc. Jpn.* **2007,** *80*, 2262.

(77) Marsh, K. N.; Deev, A.; Wu, A. C. T.; Tran, E.; Klamt, A. *Korean Journal of Chemical Engineering* **2002,** *19*, 357.

(78) Schneider, S.; Hawkins, T.; Rosander, M.; Vaghjiani, G.; Chambreau, S.; Drake, G. *Energy & Fuels* **2008,** *22*, 2871.

(79) Bayley, P. M.; Lane, G. H.; Rocher, N. M.; Clare, B. R.; Best, A. S.; MacFarlane, D. R.; Forsyth, M. J. *Phys. Chem.* Che. Phys. **2009**, 11, 7202.

(80) Matsumoto, H., Sakaebe, H. & Tatsumi, K. J. *Power Sources* **2006**, 160, 1308

(81) Seki, S.; et al. *J. Phys. Chem. B* **2006**, 110, 10228.

(82) Xu, K.; von Cresce, A. *J. Mater. Chem.* **2011**, 21,9849.

(83) Liu, J.; Manthiram, A. *J. electrochem. Soc.* **2009**, 156, A66.

(84) Guo, J.; Chen, X.; Wang, C. *J. Mater. Chem.* **2010**, 20, 5035.

(85) Guo, J.; Wang, C. *Chem. Commun.* **2010**, 46, 1428.

(86) Xu, M.; Zhou, L. Chalasani, D.; Dalavi, S.; Lucht, B. L. *J. Electrochim. Soc.* **2011**, 158, A1202.

(87) Smith, G. D.; Borodin, O.; Russo, S. P.; Rees, R. J.; Hollenkamp, A. F. *Phys. Chem. Chem. Phys.* **2009**, 11, 9884.

(88) Vatamanu, J.; Borodin, O.; Smith, G. D. *J. Phys. Chem. C* **2012**, 116 1114.

(89) Vatamanu, J,; Borodin, O.; Smith, G. D. *J. Phys. Chem. B* **2011**, 115,3073.

(90) Vatamanu, J.; Cao, L.; Borodin, O.; Bedrov, D.; Smith, G. D. *J. Phys. Chem. Lett.* **2011**, 2, 2267.

(91) Vatamanu, J.; Borodin, O.; Smith, G. D.; Smith, G. D. *J. Am. Chem. Soc.* **2010**, 132, 14825.

(92) Borodin, O.; Vatamanu, J.; Smith, G. D. *ECS Trans.* **2010**, 33, 583.

(93) Georgi, N.; Kornyshev, A. A.; Fedorov, M. V. *J. Electroanal. Chem.* **2010**, 649, 261.

CHAPTER 2

MOLECULAR DYNAMICS (MD) SIMULATIONS OF BULK AND INTERFACIAL IONIC LIQUIDS

2.1. Molecular Dynamics Simulations

Molecular dynamics (MD) simulation is realized by numerically solving the classical equations of motion for a system with N interacting molecules, in which forces between molecules and potential energy (U) are defined by force fields. Thermodynamic properties as well as other macroscopic properties of the systems can be calculated from the results of molecular dynamics simulations.

2.1.1. Potential Functions in Molecular Dynamics Simulations

In the classical MD simulation, a force field which is presented in forms and parameters of mathematical functions is used to describe the total potential energy U^{tot} for an ensemble of atoms. The total energy is generally split into nonbonded interactions U^{NB} which includes electrostatic $U^{electrostatic}$ and van der Waals U^{VDW} interactions, and bonded contributions U^{B} from vibrations of bond U^{BOND}, bends U^{BEND}, dihedrals $U^{DIHEDRAL}$, and out-of-plane bending improper dihedrals U^{IMP}.

$$U^{tot} = U^{NB} + U^{B} \tag{2-1}$$

$$U^{NB}(\mathbf{r}) = U^{electrostatic} + U^{VDW} \quad (2\text{-}2)$$

$$U^{B} = \sum_{bonds} U^{BOND} + \sum_{bends} U^{BEND} + \sum_{dihedrals} U^{DIHEDRAL} + \sum_{\substack{improper \\ dihedrals}} U^{IMP} \quad (2-3)$$

where the sums are over all bonds, bends, dihedrals, and improper dihedrals in the ensemble.

2.1.2 Molecular Dynamics Simulation Algorithm

The total energy in a system can be obtained by solving eq (2-1). The velocity and position of particles are then determined by numerically solving the Newton's equation of motion as given by

$$\boldsymbol{F}_i = -\nabla_i U = m_i \frac{d^2 \boldsymbol{r}_i}{dt^2} \text{ (2-4)}; \quad a_i = \frac{F_i}{m_i} \text{ (2-5)}; \quad r_i^{(t+\Delta t)} = r_i^t + v_i^t \nabla t + 1/2 a_i \nabla t^2 \text{ (2-6)}$$

where m_i, F_i, r_i, a_i, and v_i are mass, force, coordinate vector, acceleration, and velocity of atom i. The trajectories of particles in MD simulations, therefore, can be obtained by giving the initial positions and velocities of the particles. The MD simulation proceeds iteratively by alternatively calculating system potential energy and solving the above equations. Figure 2-1 shows a highly simplified description of the MD simulation algorithm.

1) Read in initial configuration ($\vec{r}, \vec{v}$), which is used to solve the equations of motion.

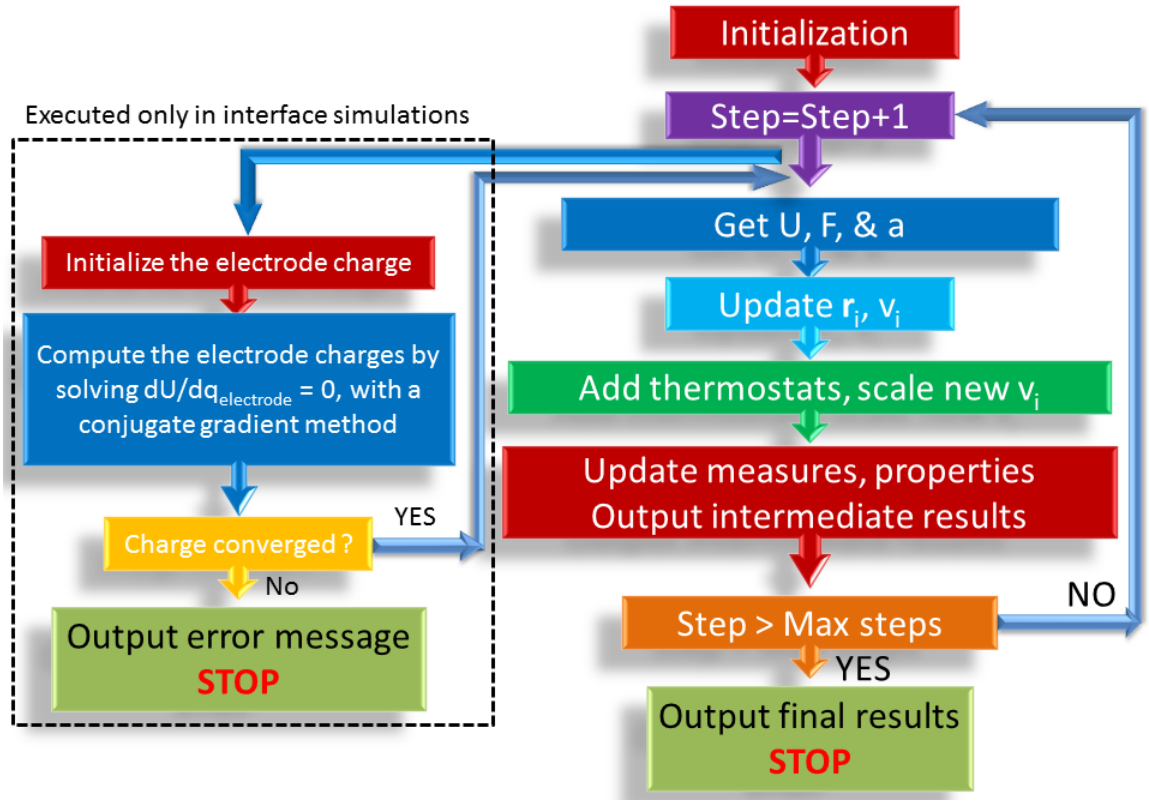

Figure 2-1. Molecular Dynamics Simulation Algorithm.

2) Obtain current step. The initial step is set to zero and increase by one at every following iteration.
3) Calculate the potential energy and force/acceleration employed to each particle.
4) Update the positions and velocities of particles.
5) Scale the new velocities by selected thermostats to implement constant temperature to the systems if required.
6) Print intermediate information/results of the systems.
7) Repeat step 2 to 7 until maximum step reached.
8) Print all the final results.

2.2 Molecular Dynamics Simulations of Bulk ILs and ILEs

By tuning the combination of cations and anions, the properties of ionic liquids can be easily tailored for different applications. The availability of a large number of cations and anions for ILs presents tremendous opportunities for finding optimal cation/anion pairs for the design of ILs and IL mixtures targeted toward specific applications. Screening and testing a large number of possible cation/anion combinations, however, presents an enormous challenge for product design as well since synthesis, purification, and characterization of a large number of ILs are expensive. Thus, efficient and reliable predictive tools are desired to provide expedient predictions of properties for specific ILs and IL mixtures. Attempt to build up empirical correlations for IL properties have been carried out such as the dependence of the degree of dynamic ion correlation on anionic donor ability (Lewis basicity), hydrogen bond donor acidity,[1] and relationship between solvent polarity and molar volumes.[2] Studies have also been undergoing in order to find out the relationship between various molecular orbital, thermodynamic, and electrostatic descriptors and IL melting temperature (T_m), density, and dielectric properties.[3-5] Other study also tried to correlate the heat of vaporization with surface tension of ILs.[6] Some success in describing density and viscosity of ILs has been made in group contribution method as well.[7] Although success of those investigations, they also prove challenging to develop generic correlations between chemical structure and thermodynamic and particularly transport properties of ILs, indicating a need for new methods in prediction of ILs.

Molecular Dynamics (MD) simulations are emerging as a good complementary (to both empirical correlations and experiments) option for prediction of various properties

of ILs. The potential advantages of MD simulation in predicting structural, thermodynamic, and transport properties of ILs and their mixtures have sparked tremendous interest in this field, leading to numerous MD simulation studies of ILs with imidazolium,[8-25] pyridinium,[26] pyrrolidinium,[27,28] triazolium,[29,30] tetraalkylphosphonium,[31] tetraalkylammonium,[32,33,34] cations and a variety of anions. IL mixtures were also simulated by MD simulations, including [N-alkyl-N-methylpyrrolidinium (pyr_{1R})][Bis(trifluorodimethanesulfonyl)imide (Ntf_2)] /[Li][Ntf_2],[35] [1-ethyl-2,3-dimethyl-imidazolim]/[Li][PF_6],[36] [1-butyl-2- methylimidazolim(bmim)]/[Li] [Ntf_2].[37,38]

Although reported MD simulation studies, including those discussed above, have provided valuable insight into molecular level correlations in ILs, they also have demonstrated that accurate prediction of thermodynamic and transport properties for this class of materials is challenging. Central to accurate prediction of any property of ILs from MD simulations is the quality of the force field employed. The predicted thermodynamics and transport properties of ILs from MD simulations are often inconsistent with or in much poorer agreement with experiments than has been typically observed for nonionic liquids. This is particularly true for prediction of transport properties (viscosity, self-diffusion coefficients, and ionic conductivity), for which deviation by almost an order of magnitude from experimental data are typical in MD studies of ILs. For example, the self-diffusion coefficients obtained from simulations using the force field of Padua et al. were a factor of 5 smaller than experimental values for [1-ethyl-3-methylimidazolium][bis(trifluoromethylsulfonyl)imide] (or [emim][Nt-f_2])[39] and significantly slower than in experiment for [1,3-dimethylimiazolium][chloride] (or [mmim][Cl]) and [1-butyl-3-methylimidazolium] [hexafluorophosphate] (or

[bmim][PF_6]).[40] Similarly, a sluggish ion transport has been found in simulations by Picałek et al.[41] of [emim][PF_6] and [bmim][BF_4] utilizing five different force fields. Maginn's simulations of alkylpyridinium-based ionic liquids predicted apparent self-diffusivities that are roughly 10 times lower than experimental values.[42] Recent simulations of 13 ILs by Tsuzuki et al.[43] using modified OPLS force field predicted self-diffusion coefficients with deviations from experiments ranging from a factor of almost 10 up to as much as a factor of 40.

2.2.1. Polarizable Force Field VS. Nonpolarizable Force Field

Most simulations of ionic liquids, including those mentioned above, have not included the polarizable terms in the force fields, resulting in significant deviations between properties predicted from simulations and measured in experiments, especially, in thermodynamic and transport properties. The ability of Nonpolarizable (two-body) force fields to accurately predict transport properties of ionic liquids is therefore less established. Only in a few instances have transport coefficients of ionic liquids been validated against experimental data. For instance, using a two body force field, MD simulations of [pyr_{1R}][Ntf_2] yielded ion self-diffusion coefficients that were an order of magnitude lower than those obtained from pfg-NMR experiments.[44] Voth et al. investigated the influence of including polarizability on the structure and dynamics of ionic liquids for [emim][NO_3] at 400K and concluded that significant effect was observed on structure and viscosity predictions for ILs by MD simulations using polarizable force field.[45] MD simulations using a two-body force field also predicted slower Li^+ transport in polymer electrolytes as compared to results from polarizable models and experimental data.[46,47,48] An atomic dipole polarizable model has been proved to better describes the

electrostatic response than the fluctuating charge model.[49,50] We, therefore, conclude that it is necessary to include many-body polarizable terms in force fields for ionic liquids to ensure accurate predictions of ILs properties.

2.2.2. An Atomic Dipole Polarizable Model for Ionic Liquids

An Atomistic Polarizable Potential for Liquids, Electrolytes, & Polymers (APPLE&P) force field that includes the dipole polarizability terms has been developed in our group and demonstrated accurate prediction, as compared to experimental values, of properties for various ILs.[51] Moreover, the APPLE&P database uses the same repulsion-dispersion nonbonded parameters for the same type atoms, in most cases independently of their chemical environment, indicating a high degree of transferability of this force field. Utilizing the APPLE&P force fields, 30 ILs containing 1-methyl-3-alkylimidazolium, 1-alkyl-2-methyl-3-alkyl-imidazolium, N-methyl-N-alkylpyrrolidinium, N-alkylpyridinium, N-alkyl-N-alkylpiperidinium, N-alkyl-N-alkylmorpholinium, tetraalkylammonium, tetraalkyl-phosphonium, N-methyl-N-oligoetherpyrrolidiniu, cations and BF_4^-, $CF_3BF_3^-$, $CH_3BF_3^-$, $CF_3SO_3^-$, PF_6^-, dicyanamide, tricyanomethanide, tetracyanoborate, Ntf_2, bis(flurosulfonyl)imide (FSI), and nitrate anions have been successfully simulated at 298 K, 333 K, 393 K and results are extensively compared with available experiments. The IL density, heat of vaporization, ion self-diffusion coefficient, conductivity, and viscosity are comparable with available experimental values, indicating MD simulations using this force field have the ability to extract IL properties accurately. All the MD simulations conducted in this work utilize the APPLE&P database.

2.2.3 Force Field Functional Forms in APPLE&P Force Field

The following form of the force field relating the potential energy $U^{tot}(\boldsymbol{r})$ to atomic coordinates $\boldsymbol{r}$ for the ensemble of atoms has been chosen. It is represented as a sum of nonbonded interactions $U^{NB}(\boldsymbol{r})$ and energy contributions from vibrations of bonds, bends, dihedrals, and out-of-plane bending (improper dihedrals) and given by

$$U^{tot}(\mathbf{r}) = U^{NB}(\mathbf{r}) + \sum_{bonds} U^{BOND}(\mathrm{r}_{ijk}) + \sum_{bends} U^{BEND}(\theta_{ijk}) + \sum_{dihedrals} U^{DIHEDRAL}\left(\phi_{ijkl}\right) + \sum_{\substack{improper \\ dihedrals}} U^{IMP}\left(\phi_{ijkl}^{imp}\right) \quad (2-7)$$

where the sums are over all bonds, bends, dihedrals, and improper dihedrals in the system. The contribution to the potential energy due to bonds, bends, dihedrals, and out-of-plane bending (improper dihedrals) are

$$U^{BOND}(\mathrm{r}_{ij}) = \frac{1}{2} k_{\alpha\beta}^{BOND}(r_{ij} - r_{ij}^{0})^2 \quad (2\text{-}8)$$

$$U^{BEND}(\theta_{ijk}) = \frac{1}{2} k_{\alpha\beta\gamma}^{BEND}(\theta_{ijk} - \theta_{ijk}^{0})^2 \quad (2\text{-}9)$$

$$U^{DIHEDRAL}\left(\phi_{\boldsymbol{ijk}}\right) = \frac{1}{2} k_{\alpha\beta\gamma\delta,n}^{DIHEDRAL}[1 - \cos(n\phi_{ijkl})] \quad (2\text{-}10)$$

$$U^{IMP}\left(\phi_{\boldsymbol{ijkl}}\right) = \frac{1}{2} k_{\alpha\beta\gamma\delta}^{IMP}(\phi_{ijkl}^{imp})^2 \quad (2\text{-}11)$$

where r_{ij} and r_{ij}^{0} are the instantaneous and equilibrium bond length. θ_{ijk} and θ_{ijk}^{0} are the instantaneous and natural bending angles for atoms i, j and k; ϕ_{ijkl} is the dihedral angle for $i, j, k,$ and l; and ϕ_{ijkl}^{imp} is the out-of-plane bending angle for an sp^2 center at atom j.

The strength of these interactions is characterized by the corresponding force constants $k_{\alpha\beta\gamma}^{BEND}$, $k_{\alpha\beta\gamma\delta,n}^{DIHEDRAL}$, and $k_{\alpha\beta\gamma\delta}^{IMP}$, respectively. The subscripts α, β, γ, and δ denote atom type for atoms i, j, k, and l, respectively. The nonbonded energy $U^{NB}(\mathbf{r})$ consists of the sum of two-body repulsion and dispersion energy terms $U^{RD}(\mathbf{r})$, the energy due to interactions of fixed charges $U^{coul}(\mathbf{r})$, and the polarization energy $U^{pol}(\mathbf{r})$ arising from the interaction of induced dipoles with fixed charges and other induced dipoles,

$$U^{NB}(\mathbf{r}) = U^{RD}(\mathbf{r}) + U^{coul}(\mathbf{r}) + U^{pol}(\mathbf{r})$$

$$= \sum_{i>j}\left(A_{\alpha\beta}\exp\left(-B_{\alpha\beta}r_{ij}\right) - C_{\alpha\beta}r_{ij}^{-6} + D\left(\frac{12}{B_{\alpha\beta}r_{ij}}\right)^{12}\right) + U^{coul}(\mathbf{r})$$

$$+ U^{pol}(\mathbf{r}) \qquad (2-12)$$

where $A_{\alpha\beta}$ and $B_{\alpha\beta}$ are the repulsion parameters and $C_{\alpha\beta}$ is the dispersion parameter for interaction between atoms i and j with atom types α and β. The term $D(12/\beta_{ij}r_{ij})^{12}$, with $D=5\times10^{-5}$ kcal/mol for all pair interactions, is essentially zero at typical nonbonded atomic separations, but become the dominant term at r_{ij} < 1 Å, ensuring that $U^{RD}(r)$ is repulsive at distances much smaller than the size of an atom.

The Coulomb interactions are represented in liquids by assigning partial charges (q_i, q_j) to atomic centers and off-atom sites (eq 2-13).

$$U^{coul}(\mathbf{r}) = \sum_{i>j}\left(\frac{q_i q_j}{4\pi\varepsilon_0 r_{ij}}\right) \qquad (2-13)$$

where ε_0 is the dielectric permittivity of vacuum. The off-atom site is added to improve the electrostatic potential description near electron lone-pairs. Instead of introducing two additional force centers to model the long-pair contribution to the electrostatic potential

around ether oxygen atoms, APPLE&P force field uses a single "extended charge" that is situated at 0.5 Å from the oxygen atom, as shown in Figure 2-2. An extended charge in the plane of S-N-S bend of FSI and NTF2 may also be included in order to improve the description of electrostatic potential around the anions. Intramolecular nonbonded interactions are included for atoms separated by three or more covalent bonds.

The atom dipole polarizability model is used to represent many-body polarizable interaction in the force field. The potential energy due to dipole polarization is not pair wise additive and is given by eq 2-12 using the Ponder's notation for damping functions, given by eq 2-13 to 2-16.[52] A modified Thole model[53] is used to prevent the so-called "polarization catastrophe" from occurring at close atom approaches. In this model, the induced dipoles are damped as though one of the point dipoles in each pairwise interaction is replaced by a smeared charge distribution.

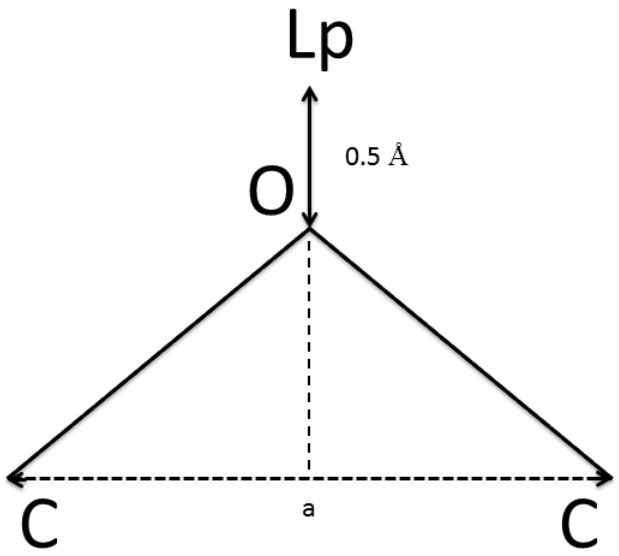

Figure 2-2. Location of the "extended charge" at ether oxygen atoms. The "extended partial charge" denoted as Lp is located at the continuation of the O-a median.

$$U^{pol}(\mathbf{r}) = -\sum_i \mu_i \cdot E_i^0 - 0.5\sum_i\sum_j \mu_i \cdot T_{ij} \cdot \mu_j + \sum_i \left(\mu_i \cdot \frac{\mu_i}{2\alpha_i}\right)$$

$$= -\frac{1}{2}\sum_i \vec{\mu}_i \cdot \vec{E}_i^0 \qquad (2-14)$$

where $\vec{\mu}_i = \alpha_i \vec{E}_i^{tot}$ is an induced dipole at force center i, α_i is the isotropic atomic polarizability fitted to reproduce polarization response of a molecule due to a test charge, , $\vec{E}_i^{tot}$ is the total electrostatic field at the atomic site *i* due to permanent charges $q_j$and induced dipoles $\vec{\mu}_j$, $\vec{E}_i^0$ is the electric field due to fixed charges only, and the second-order dipole tensor T_{ij} is given by

$$T_{ij} = \frac{1}{4\pi\epsilon_0 r_{ij}^3}\left[\lambda_5(r_{ij})\frac{3\boldsymbol{r}_{ij}\boldsymbol{r}_{ij}}{r_{ij}^2} - \lambda_3(r_{ij})\right] \qquad (2-15)$$

$$\lambda_5(r_{ij}) = 1 - (1 + a_T u^3)\exp(-a_T u^3) \qquad (2-16)$$

$$\lambda_3(r_{ij}) = 1 - \exp(-a_T u^3) \qquad (2-17)$$

$$u = \frac{r_{ij}}{\alpha_i \alpha_j} \qquad (2-18)$$

The Thole screening parameter a_T defines the width of the smeared charge distribution. Atoms connected by bonds and bends were excluded from a list of nonbonded interactions. The intramolecular interaction between an induced dipole and a partial charge separated by three bonds was scaled by 0.8 because it provided improved description of electrostatic potential around molecules.Screening of the induced dipole-

induced dipole interactions at short distance is included in all simulations to improve the stability of our simulations.

2.2.4. Force Field Fitting Methodology

Since the aim of this work is not to develop force field, the force field fitting methodology is briefly summarized here. The atomic polarizabilities are determined by fitting to the molecular polarizability in the gas phase determined from quantum chemistry (QC) calculations and by fitting the polarization contribution to the binding energy for the interaction of anions with a 1e charge and cations with the -1e charge. Partial charges are fit to describe the electrostatic potential on a grid of points around a molecule, as well as molecular gas phase dipole moment, all obtained from QC calculations. Bond lengths and natural bending angles are fit to reproduce the gas-phase geometries obtained from quantum chemistry, while bending force constants are either taken from previously developed force fields or fit to the energy for the bending angle distortions obtained from quantum chemistry. Finally, dihedral angle parameters are determined by fitting the gas phase conformational-energy surface of model molecules as determined from quantum chemistry.

2.3. Molecular Dynamics Simulations of Electrolyte/Electrode Interfaces

Simulations studies of electrode-electrolyte interfaces have been largely performed utilizing a constant charge distribution on the electrode surfaces.[54 - 57] This method, however, has two obvious drawbacks. First, the model is not able to control the electrostatic potential between the electrodes during simulations. Second, the local charge distribution at the electrode surface is not able to adjust to the structure fluctuation of the

electrolyte near the surfaces. A more realistic representation of the charge distribution on an electrode can be obtained if the electrode charges are allowed to fluctuate according to the imposed electrostatic potential and the local electrode/electrolyte structure, through which all electrode atoms are able to maintain constant, controlled electrostatic potential. Madden and co-workers developed an "electroactive interface" methodology to perform MD simulations under constant and controlled potential on an infinitely conductive electrode.[58] The methodology allows equilibrium fluctuations of the electrode charges by which the total electrostatic energy is minimized. Electrid double layer (EDL) capacitance predicted from simulations of metal confined molten salts LiCl/KCl and LiCl/$MgCl_2$ using the "electroactive interface" model are found in consistent with experimental data. This methodology was also validated and utilized by our group in simulations of ILs[59] and carbonates mixed with lithium salts.[60] In this dissertation, we extend the simulations to understanding the behavior of ionic liquid electrolytes which contain lithium salts and organic solvents.

2.3.1. Constant and Controlled Potential on Electrode

Rather than imposing a certain charge density on electrode surface and measuring the generated (fluctuant) potential, the electrode charges and electrostatic energy in the present simulations are modified to maintain the electrostatic potential on each electrode as a constant and desired value for each integration step by an "electroactive interface" methodology developed in our group.[61] The charge of each electrode atom was modeled as a Gaussian distributed charge centered on the atom,[62]

$$\rho_i(r - R_i) = q_i \left(\frac{\varepsilon_i^2}{\pi}\right)^{3/2} \exp(-\varepsilon_i^2 |r - R_i|^2) \qquad (2\text{-}19)$$

where $\rho_i(r - R_i)$ is the electric charge density on an electrode atom i placed at the position R_i and $1/\varepsilon_i$ is the width of distribution. The charges on electrodes were modified at each time-step, such that the electrode atoms are subjected to the same electrostatic potential V_i^0 imposed on the electrodes, therefore, ensuring control of the electrostatic potential difference between electrodes during the simulations.

2.3.2. Electrostatic Energy of the System

The total electrostatic energy of the system with two electrodes and electrolyte is then given by

$$U = \frac{1}{2}\sum_{\boldsymbol{k}}^{*}\sum_{i,j}\frac{q_i q_i}{|\boldsymbol{R}_{ij} + k\boldsymbol{L}|} - \frac{1}{2}\sum_{\boldsymbol{k}}^{*}\sum_{i,j}\frac{q_i q_i}{|\boldsymbol{R}_{ij} + k\boldsymbol{L}|}erfc(\varepsilon_{ij}|\boldsymbol{R}_{ij}| + k\boldsymbol{L})$$

$$+\sum_i \frac{q_i^2}{\sqrt{\pi}}\varepsilon_{ij}\delta(i,G) \quad (2-20)$$

where $\boldsymbol{R}_{ij}$ is the distance vector between two ions *i* and *j* in the initial box (corresponding to $\boldsymbol{k}$=0), $\boldsymbol{k}$ is the multiplicity of the initial cell, and $\boldsymbol{k}$L is a multiplicity factor of the distance $\boldsymbol{R}_{ij}$ between ions *i* and *j*. The restriction labeled with * in the summation over $\boldsymbol{k}$ indicates that the sum over atomic pairs *ij* is constrained as I ≠ j when $\boldsymbol{k}$ =0. The Gaussian cross-widths $1/\varepsilon_{ij}$ are given by

$$\frac{1}{\varepsilon_{ij}^2} = \frac{1}{\varepsilon_i^2} + \frac{1}{\varepsilon_j^2} \quad (2\text{-}21)$$

The delta symbol, $\delta(i,G)$, is zero for a point charge and one if the charge is Gaussian distributed, ad it explicitly excludes the Gaussian self-interactions$\sum_i \frac{q_i^2}{\sqrt{\pi}}\varepsilon_{ij}$ for charges that are not Gaussian distributed.

The first term in the expression of the electrostatic energy was solved using the standard Ewald summation techniques for a system of point charges in a 2D-periodic geometry[63] employing the computatinally expedient smooth particle mesh Ewald (SMPE) version.[64] For the specific widths $1/\varepsilon_{ij}$ used in this work, the contribution of the second term is essentially negligible beyond a cut-off of 9-11 Å, therefore the complementary error function in eq 2-18 was approximated as short ranged:

$$\frac{1}{2}\sum_{\boldsymbol{k}}^{*}\sum_{i,j}\frac{q_i q_i}{|\boldsymbol{R}_{ij}+k\boldsymbol{L}|}erfc(\varepsilon_{ij}|\boldsymbol{R}_{ij}|+k\boldsymbol{L}) \approx \frac{1}{2}\sum_{\boldsymbol{k}}^{*}\sum_{i,j,i\neq j}\frac{q_i q_i}{|\boldsymbol{R}_{ij}|}erfc(\varepsilon_{ij}|\boldsymbol{R}_{ij}|)(2-22)$$

that is, contribution from the Gaussian distributed character of electrode charges to the electrostatic energy is within a short range. This approximation, however, is not appropriate when the Gaussian widths are larger than about 1/3 of the short-ranged cut-off. In such case, a Ewald-like procedure could be employed to evaluate the long range contribution.[58]

2.4. General Properties Calculations from Molecular Dynamics Simulations

Heat of vaporization (ΔH^{vap}) is usually used as a reflection of the strength of intermolecular interactions, cohesion energy, and defined as a heat required to evaporate an ion pair from a liquid phase to the gas phase at constant pressure as indicated by,

$$\Delta H^{vap} = E_g - E_l + RT \qquad (2\text{-}23)$$

where the subscript l or g indicates liquid or gas phase, E is the internal energy at temperature T and pressure P, and R is the universal gas constant.

The local structure of liquid is obtained by calculating Radial Distribution Function (RDF or g(r)) given by

$$\rho g(r_{ij}) = \frac{1}{N}\langle \sum_{i}^{N} \sum_{j \neq i}^{N} \delta[r - r_{ij}] \rangle \qquad (2-24)$$

where N is the number of atoms/molecules, ρ=N/V is the liquid number density, r_{ij} is a vector between centers of atoms/molecules *i* and *j*, and <> denotes time average.

The self-diffusion coefficient D_i of species *i* from MD simulations was calculated using the Einstein relation

$$D_i = \lim_{t \to \infty} D_i^{app}(t) = \lim_{t \to \infty} \frac{< MSD_i(t) >}{6t} \qquad (2-25)$$

where $MSD_i(t) = (r(t) - r(0))^2$ is the mean-square displacement of the center of mass of a molecule of species i during time t, < > denotes an ensemble average, and $D_i^{app}(t)$ is the time-dependent apparent diffusion coefficient.

The ionic conductivity from MD simulations can be calculated using the Einstein relation

$$\lambda = \lim_{t \to \infty} \lambda^{app}(t)$$

$$= \lim_{t \to \infty} \frac{e^2}{6tVK_BT} \sum_{ij}^{N} Z_i Z_j < [R_i(t) - R_i(0)][R_j(t) - R_j(0)] > \qquad (2-26)$$

where e is the electron charge, V is the volume of the simulation box, K_B is Boltzmann's constant, T is the temperature, t is time, Z_i and Z_j are the charges over ions i and j in electrons, $R_i(t)$ is the displacement of the ion *i* during time t, the summation is performed

over all ions, < > denotes the ensemble average, N is the total number of ions in the simulation box and $\lambda^{app}(t)$ is the apparent time-dependent conductivity. Determining the long-time limit of $\lambda^{app}(t)$ using equation (2-26) is, however, problematic even at higher temperatures where the diffusion coefficients can be accurately determined because $\lambda^{app}(t)$ has poor statistics and a higher uncertainty compared to MSD(t). Fortunately, conductivity can be decomposed into an "ideal" conductivity that would be realized if ion motion were uncorrelated, denoted λ_{uncorr}, and the degree to which ion motion is in fact correlated, or α.

$$\lambda_{uncorr} = \lim_{t\to\infty} \lambda_{uncorr}^{app}(t) = \lim_{t\to\infty} \frac{e^2}{6tVK_BT} \sum_{i}^{N} {Z_i}^2 < [R_i(t) - R_i(0)]^2 >$$

$$= \frac{e^2}{VK_BT} (n_{Li^+} D_{Li^+}^{app} + n_{pyr_{13}} D_{pyr_{13}}^{app} + n_{Ntf_2} D_{Ntf_2}^{app}) \qquad (2\text{-}27)$$

where, n_i is the number of atoms of type *i*. The degree of uncorrelated ion motion (α) is typically measured as the ratio of the collective (total) charge transport (given by λ) to the charge transport due to self-diffusion only (the limit of uncorrelated motion), λ_{uncorr}, and is given by

$$\alpha = \frac{\lambda}{\lambda_{uncorr}} = \lim_{t\to\infty} \alpha(t) = \lim_{t\to\infty} \frac{\lambda^{app}(t)}{\lambda_{uncorr}^{app}(t)} \qquad (2\text{-}28)$$

thus, α=1 corresponds to uncorrelated ion motion, while α=0 if all of the cations only move together with anions. The reported conductivities in this dissertation are all calculated using eq (2-28) by first obtain α and λ_{uncorr}.

The equilibrium (zero shear rate) viscosity was calculated for the selected ILs using the Einstein relation including both diagonal and nondiagonal elements to enhance statistics,

$$\eta = \lim_{t\to\infty} \eta(t) = \lim_{t\to\infty} \frac{V}{20k_BTt}(< \sum_{\alpha,\beta}(L_{\alpha\beta}(t) - L_{\alpha\beta}(0))^2 >) \quad (2\text{-}29)$$

where $L_{\alpha\beta} = \int_0^t P_{\alpha\beta}(t')dt'$, k_B is the Boltzmann constant, T is temperature, *t* is time, V is the volume of the simulation box, and $P_{\alpha\beta}$ is the stress sensor given by

$$P_{\alpha\beta} = \frac{\sigma_{\alpha\beta}+\sigma_{\alpha\beta}}{2} - \frac{\delta_{\alpha\beta}}{3} tr(\sigma) \quad (2\text{-}30)$$

where $\sigma_{\alpha\beta}$ is the stress tensor, $\delta_{\alpha\beta}$=1 for α=β, $\delta_{\alpha\beta}$=0 for α≠β.

2.5. References

(1) Tokuda, H.; Tsuzuki, S.; Susan, M. A. B. H.; Hayamizu, K.; Watanabe, M. *J. Phys. Chem. B* **2006**, 110, 19593.

(2) Kobrak, M. N. *Green Chem.* **2008**, 10, 80.

(3) Trohalaki, S.; Pachter, R.; Drake, G. W.; Hawkins, T.; *Energy Fuels* 2005, 19, 279.
(4) Krossing, I.; Slattery, J. M. Daguenet, C.; Dyson, P. J.; Oleinikova, A.; Weingartner, H. *J. Am. Chem. Soc.* **2006**, 128, 13427.

(5) Gardsa, R. L. Coutinho, J. *A. P. Fluid Phase Equilib.* **2008**, 267, 188.

(6) Verevkin, S. P. *Angew. Chem., Int. Ed.* **2008**, 47, 5071.

(7) Gardas, R. L.; Coutinho, J. A. P. *Fluid Phase Equilib.* **2008**, 266, 195.

(8) Wang, L.; Huang, Y.; Jia, D. *Electrochimica Acta* **2006,** *51*, 4950.

(9) Bhargava, B. L.; Balasubramanian, S. *J. Chem. Phys.* **2005,** *123*, 144505.

(10) (a) Shah, J. K.; Maginn, E. J. *J. Phys. Chem. B* **2005,** *109*, 10395; (b) Morrow, T. I.; Maginn, E. J. *J. Phys. Chem. B* **2002,** *106*, 12807-12813; (c) Shah, J. K.; Brennecke, J. F.; Maginn, E. J. *Green Chemistry* **2002,** *4*, 112; (d) Cadena, C.; Anthony, J. L.; Shah, J. K.; Morrow, T. I.; Brennecke, J. F.; Maginn, E. J. *J. Am. Chem. Soc.* **2004,** *126*, 5300.

(11) (a) Del Popolo, M. G.; Lynden-Bell, R. M.; Kohanoff, J. *J. Phys. Chem. B* **2005,** *109*, 5895 ; (b) Lynden-Bell, R. M.; Kohanoff, J.; Del Popolo, M. G. *Faraday Discussions* **2005,** *129*, 57; (c) Del Popolo, M. G.; Voth, G. A. *J. Phys. Chem. B* **2004,** *108*, 1744; (d) Yan, T. Y.; Burnham, C. J.; Del Popolo, M. G.; Voth, G. A. *J. Phys. Chem. B* **2004,** *108*, 11877.

(12)Kunsagi-Mate, S.; Lemli, B.; Nagy, G.; Kollar, L. *J. Phys. Chem. B* **2004,** *108*, 9246.
(13) Antony, J. H.; Mertens, D.; Breitenstein, T.; Dolle, A.; Wasserscheid, P.; Carper, W. R. *Pure and Applied Chemistry* **2004,** *76*, 255.

(14) (a) de Andrade, J.; Boes, E. S.; Stassen, H. *J. Phys. Chem. B* **2002,** *106*, 13344 ; (b) de Andrade, J.; Boes, E. S.; Stassen, H. *Ionic Liquids Iiia: Fundamentals, Progress, Challenges, and Opportunities, Properties and Structure* **2005,** *901*, 118.

(15) Jensen, M. P.; Neuefeind, J.; Beitz, J. V.; Skanthakumar, S.; Soderholm, L. *J. Am. Chem. Soc.* **2003,** *125*, 15466.

(16) (a) Lopes, C. J. N.; Deschamps, J.; Padua, A. A. H. *J. Phys. Chem. B* **2004,** *108*, 2038; (b) Lopes, J. N. C.; Deschamps, J.; Padua, A. A. H. *Ionic Liquids Iiia: Fundamentals, Progress, Challenges, and Opportunities, Properties and Structure* **2005,**

901, 134; (c) Deschamps, J.; Padua, A. A. H. *Ionic Liquids Iiia: Fundamentals, Progress, Challenges, and Opportunities, Properties and Structure* **2005,** *901*, 150; CanongiaLopes, J. N. A.; (d) Padua, A. A. H. *J. Phys. Chem. B* **2006,** *110*, 7485; (e) Deetlefs, M.; Hardacre, C.; Nieuwenhuyzen, M.; Padua, A. A. H.; Sheppard, O.; Soper, A. K. *J. Phys. Chem. B* **2006,** *110*, 12055; (f) CanongiaLopes, J. N.; CostaGomes, M. F.; Padua, A. A. H. *J. Phys. Chem. B* **2006,** *110*, 16816.

(17) Wu, X. P.; Liu, Z. P.; Huang, S. P.; Wang, W. C. *Phys. Chem. Chem. Phys.* **2005,** *7*, 2771.

(18) Hunt, P. A. *Molecular Simulation* **2006,** *32*, 1.

(19) Micaelo, N. M.; Baptista, A. M.; Soares, C. M. *J. Phys. Chem. B* **2006,** *110*, 14444.
(20) Rey-Castro, C.; Vega, L. F. *J. Phys. Chem. B* **2006,** *110*, 14426.

(21) Siqueira, L. J. A.; Ribeiro, M. C. C. *J. Phys. Chem. B* **2007,** *11*, 11776.

(22) Bhargava, B. L.; Balasubramanian, S. *J. Chem. Phys.* **2007,** *127*, 114510.

(23) Koddermann, T.; Paschek, D.; Ludwig, R. *ChemPhysChem* **2007,** *8*, 2464.

(24) Bhargava, B. L.; Balasubramanian, S.; Klein, M. L. *Chem. Comm.* **2008**, 3339.
(25) Picálek, J.; Kolafa, J. *J. Mol. Liq.* **2007,** *134*, 2.

(26) Cadena, C.; Zhao, Q.; Snurr, R. Q.; Maginn, E. J. *J. Phys. Chem. B* **2006,** *110*, 282.
(27) CanongiaLopes, J. N.; Padua, A. A. H. *J. Phys. Chem. B* **2004,** *108*, 16893.

(28) Borodin, O.; Smith, G. D. *J. Phys. Chem. B* **2006,** *110*, 11481.

(29) Cadena, C.; Maginn, E. J. *J. Phys. Chem. B* **2006,** *110*, 18026.

(30) Jiang, W.; Yan, T. Y.; Wang, Y. T.; Voth, G. A. *J. Phys. Chem. B* **2008,** *112*, 312.
(31) Zhou, G. H.; Liu, X. M.; Zhang, S. J.; Yu, G. G.; He, H. Y. *J. Phys. Chem. B* **2007,** *111*, 7078.

(32) Adebahr, J.; Grozema, F. C.; deLeeuw, S. W.; MacFarlane, D. R.; Forsyth, M. *Solid State Ionics* **2006,** *177*, 2845.

(33) Schurhammer, R.; Wipff, G. *J. Phys. Chem. B* **2007,** *111*, 4659.

(34) Siqueira, L. J. A.; Ribeiro, M. C. C. *J. Phys. Chem. B* **2007,** *111*, 11776

(35) Borodin, O.; Smith, G. D.; Henderson, W. *J. Phys. Chem. B* **2006,** *110*, 16879.

(36) Niu, S.; Cao, Z.; Li, S.; Yan, T. *J. Phys. Chem. B* **2010**, 114, 877.

(37) Monteiro, M. J.; Bazito, F. F. C.; Aiqueira, L. J. A.; Ribiro, M. C. C.; Torresi, R. M. *J. Phys, Chem. B* **2008**, 112, 2102.

(38) Umebayashi, Y.; Hamano, H.; Seki, S.; Minofar, B.; Fujii, K.; Hayamizu, K.; Tsuzuki, S.; Kameda, Y.; Kohara, S.; Watanabe, M. *J. Phys. Chem. B* **2011**, 115, 12179.

(39) Koddermann, T.; Paschek, D.; Ludwig, R. *ChemPhysChem* **2007**, 8, 2464.

(40) Bhargava, B. L.; Balasubramanian, S. *J. Chem. Phys.* **2007**, 127, 114510.

(41) Picâek, J.; Kolafa, J. *J. Mol. Liq.* **2007**, 134, 29.

(42) Cadena, C.; Zhao, Q.; Snurr, R. Q.; Maginn, E. J. *J. phys. Chem. B* **2006**, 110, 2821.
(43) Tsuzuki, S.; Shinoba, W.; Saito, H.; Mikami, M.; Tokuda, H.; Watanabe, M. *J. Phys. Chem. B* **2009**, 113, 10641.

(44) Cadena, C.; Zhao, Q.; Snurr, R. O.; Maginn, E. J. *J. Phys. Chem. B* **2006**, 110, 2821.

(45) Yan, T. Y.; Burnham, C. J.; Del Popolo, M. G.; Voth, G. A. *J. Phys. Chem. B* **2004**, 108, 11877.

(46) Borodin, O.; Smith, G. D.; Douglas, R. J. *Phys. Chem. B* **2003**, 107, 6824.

(47) Borodin,; Smith, G.D.; Jaffe, R. L. *J. Comput. Chem.* **2001**, 22, 641.

(48) Borodin, O.; Smith, G. D. *Macromolecules* **2000**, 33, 2273.

(49) Stern, H. A.; Kaminshi, G. A.; Banks, J. A.; Zhou, R.; Berne, B. J.; Friesner, R. A. *J. Phys. Chem. B* **1999**,103 4730.

(50) Masia, M.; Probst, M.; Rey, R.*J. Chem.Phys.* **2004**, 121, 7362.

(51) Borodin, O. *J. Phys. Chem. B* **2009**, 113, 11463.

(52) Ren, P.; Ponders, J. W. *J. Chem. Phys.* **1994**, 100, 2838.

(53) Thole, B. T. *Chem. Phys.* **1981**, 59, 341.

(54) Fedorov, M. V.; Kornyshev, A. A. *J. Phys. Chem. B* **2008**, 112, 11868.

(55) Spohr, E. *Electrochim. Acta* **1998**, 44, 1697.

(56) Pinilla, C.; Del Popolo, M. G.; Lynden-Bell, R. M.; Kohanoff, J. J. *Phys. Chem. B* **2005**, 109, 17922.

(57) Fedorov, M. V.; Kornyshev, A. A. *Electrochim. Acta*, **2008**, 53, 6835.

(58) Reed, S. K.; Lanning, O. J.; Madden, P. A. *J. Chem. Phys.* **2007**, 126, 084704.

(59) (a)Vatamanu, J,; Borodin, O.; Smith, G. D. *J. Phys. Chem. B* **2011**, 115,3073; (b) Vatamanu, J.; Cao, L.; Borodin, O.; Bedrov, D.; Smith, G. D. *J. Phys. Chem. Lett.* **2011**, 2, 2267; (c) Vatamanu, J.; Borodin, O.; Smith, G. D.; Smith, G. D. *J. Am. Chem. Soc.* **2010**, 132, 14825; (d) Borodin, O.; Vatamanu, J.; Smith, G. D. *ECS Trans.* 2**010**, 33, 583; (e) Vatamanu, J.; Borodin, O.; Bedrov, D.; Smith, G. D. *J. Phys. Chem. C* **2012,** 116, 7940; (f) Xing, L.; Vatamanu, J.' Smith, G. D.; Bedrov, D. *J. Phys. Chem. Lett.* **2012**, 3, 1124.

(60) (a) Smith, G. D.; Borodin, O. ; Russo, S. P.; Rees, R. J.; Hollenkamp, A. F. *Phys. Chem. Chem. Phys.* **2009**, 11, 9884. (b) Vatamanu, J.; Borodin, O.; Smith, G. D. *J. Phys. Chem. C* **2012**, 116, 1114.

(61) Vatamanu, J.; Borodin, O.; Smith, G. D.; *Phys. Chem. Chem. Phys.* **2010**, 12, 170.
(62) Siepmann, J. I.; Sprik, M. *J. Chem. Phys.* 1995, 102, 511.

(63) (a) Kawata, M.; Mikami, M. Chemi. Phys. Lett. 2001, 340, 157; (b)Kawata, M.; Nagashima, U. *Chem. Phys. Lett.* **2001**, 340, 165. (c)

(64) (a) Essmann, U.; Perera, L. Berkowitz, M. L.; Darden, T. Lee, H.; Pedersen, L. G. J. *Chem. Phys.* 1995, 103, 8577; (b) Kawata, M.; Mikami, M.; Nagashima, U. *J. Chem.Phys.* 2002, 116, 3430; (c) Kawata, M.; Mikami, M.; Nagashima, U. *J. Chem. Phys.* **2002**, 117, 3526.

CHAPTER 3

INFLUENCE OF POLARIZATION ON STRUCTURAL, THERMODYNAMICS, AND DYNAMIC PROPERTIES OF IONIC LIQUIDS OBTAINED FROM MOLECULAR DYNAMICS SIMULATIONS

Note that this chapter is under preparation for the Journal of Physical Chemistry B.

3.1. Introduction

The majority atomistic nonpolarizable force fields used in simulations of ILs, including those mentioned before, have been tuned to reproduce experimental density and sometimes heat of vaporization. Such tuning is usually sufficient to allow reasonable prediction of transport properties in nonionic liquids. Yet, as illustrated by the examples in Chapter 2, this approach does not work very well in simulations of ILs and is further complicated by the paucity of available experimental data on heats of vaporization for ILs. In some studies, an improved description of dynamical properties was even obtained by reducing the ion charges to 0.9*e* or 0.8*e* (*e*= electron charge).[1,2,3] Moreover, most of the nonpolarizable force fields reported in the literature are specific for the systems they were developed for, and therefore, even when there are instances of force fields that accurately reproduce transport and thermodynamic properties for the IL of interest (e.g., the force field of Loddermann, Paschek, and Ludwig[4] for [alkylimidazolium][Ntf_2]), and

Chaban[5] for [1-butyl-3-methylimidazolium(bmim)][BF_4] mixed with acetonitrile, the transferability of such force field to other cations and anions is questionable.

The recently developed Atomic Polarizable Potential for Liquids, Electrolytes, & Polymers (APPLE&P) force field in our group shows its ability to accurately predict various properties of interest, as well as its high degree of transferability.[6] This model overcomes most of the problems of the conventional nonpolarizable force fields. The unprecedented accuracy and transferability of this force field, however, raise a fundamental but interesting question: What role does the inclusion of polarizability play in the success of the APPLE&P force field in predicting the dynamics accurately?

There have been several works that investigated the influence of polarization effects on properties of ILs predicted from MD simulations. Madden and co-workers have simulated several simple molten salts using both polarizable and nonpolarizalbe models.[7,8] In their investigation of KI/vacuum interfaces,[7] inclusion of polarization widens the interfacial region and therefore results in ~20% lower values of the surface tension as compared to simulations with nonpolarizable force field. In another study of LiCl and KCl liquids,[8] it was found that inclusion of polarization did not influence the structure of the molten salts but increased the self-diffusion coefficients of all ions by about 10-20% as compared to those obtained from simulations using the same force field with atom-based polarizabiities set to zero. The influence of polarization on structural, thermodynamic, and dynamical properties was already investigated for [emim][NO_3][9,10] and [emim][BF_4].[11] These studies found a significant difference in anion-anion pair distribution functions as well as transport properties obtained from simulations using the polarizable force field and those obtained from simulations using nonpolarizable force

field. The self-diffusion coefficients for both ions at 400 K were found to be a factor of 2-3 larger and viscosity ~30% lower in simulations with the polarizable model as compared to those from simulations with the nonpolarizable force fields[6,9] The surface tension obtained for the [emim][NO_3]/vacuum interface from simulations that included polarization was more consistent with experimental data and was about 30% lower than predictions from simulations using nonpolarizable force field. Hansen and McDonald suggested that inclusion of polarization effects provide additional screening mechanisms that do not require movement of ion cores to provide local charge neutrality. These additional mechanisms cause the cage effect to be smaller for polarizable ions, which should lead to increased damping of oscillations in the velocity auto-correlation function and increased self-diffusion coefficients.

In this chapter, we systematically investigate the influence of many-body polarization on several important properties of a series of typical ILs, as predicted from MD simulations. Structures and notation for cations and anions are shown in Figure 3-1. We investigate the influence of polarization on representative structural, thermodynamic, and dynamic properties of selected ILs by comparing results from MD simulations using the polarizable APPLE&P force field and a nonpoarizable version of the APPLE&P force field in which polarization interactions were simply turned off (i.e., atom-based dipole polarizabilities were set to zero). In particular, the influence of polarization on the properties of these ILs containing cyano group is compared with that obtained from simulations of other ILs.

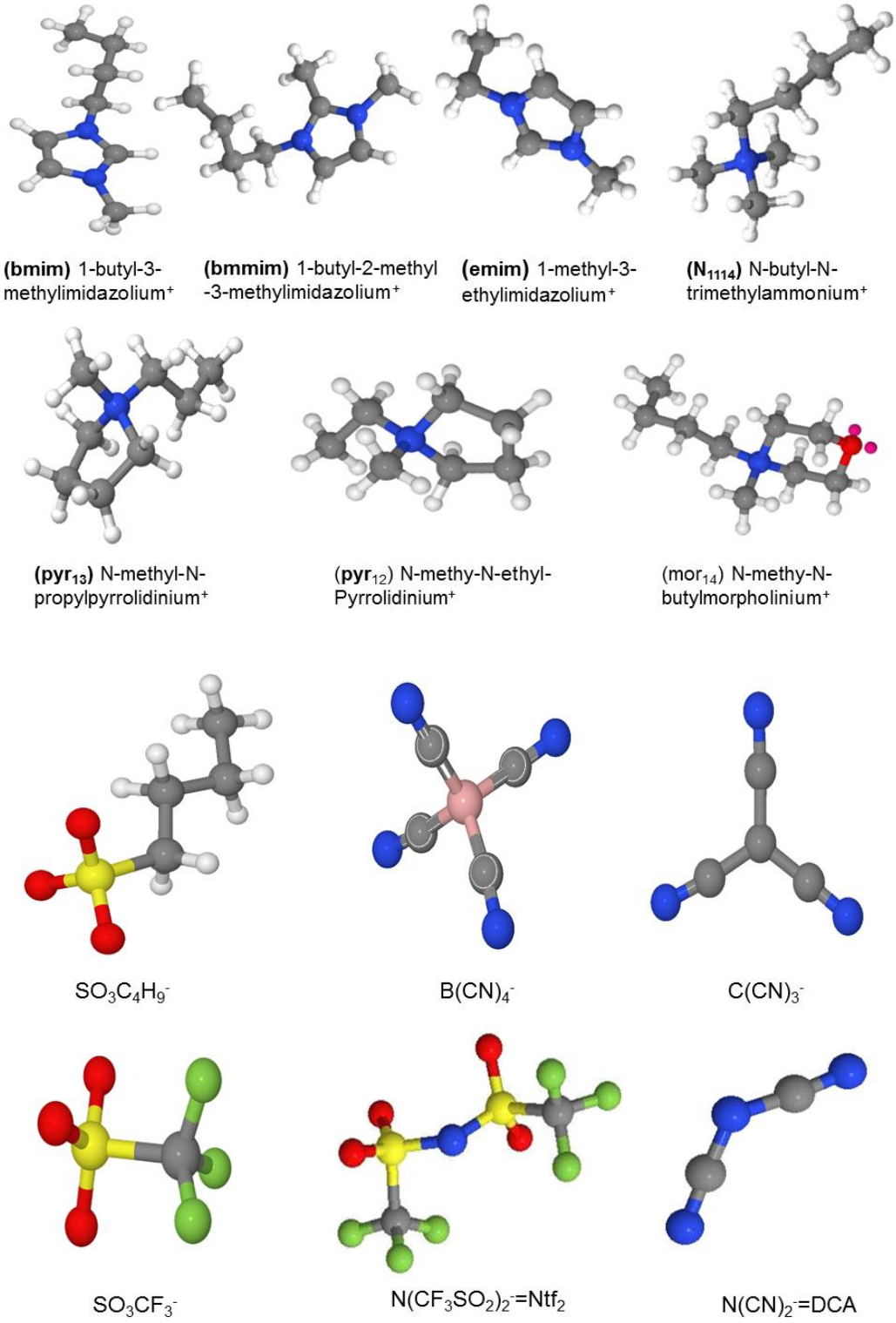

Figure 3-1. Molecular structure and notation for cations and anions used in the simulations.

3.2. Simulation Details

3.2.1. Systems Studied

The investigated ILs are listed in Table 3-1, together with available experimental data for density (ρ), viscosity (η), and conductivity (λ) from experiments. The molecular structure and simplified notation of cations and anions are shown in Figure 3-1. All the ILs systems were running at two temperatures, 298 K and 393 K. As can be seen from Table 3-1, the viscosity (η) of selected ILs at 298 K ranges from 16 mPa·S for [emim][DCA] up to as much as 99 mPa·S for $[N_{1114}][Ntf_2]$. Here, we focused on relatively low viscosity ILs to reduce computational costs. Moreover, we note that ILs with low viscosity are highly desired for numerous applications, including batteries, super capacitors, and hypergolic fuels. Taking into account significant difference in chemical structure and physical properties of the selected ILs, we believe that trends and phenomena investigated in this work will be generically applicable to a wide range of ILs.

To determine whether the inclusion of many-body polarization effects is particularly important for ILs, our results are also compared with influence of polarization on polar but nonionic compound, such as water, dimethyl ketone (DMK), and ethylene carbonate. Simulations of those nonionic compounds were done by Dr. Dmitry and details can be found in ref. 12.

3.2.2. Polarizable and Nonpolarizable Force Fields

We employed the APPLE&P force field for all the Ionic Liquids investigated in this work. Details of the APPLE&P force field functional forms and parameterization procedure can be found in Chapter 2. Here we only briefly highlight the conceptual

Table 3-1. List of Ionic Liquids Investigated in This Study Together with Available in the Literature Experimental Data on Density (ρ), Viscosity (η), Self-Diffusion Coefficient (D), and Conductivity (λ).

IL	$\rho/10^3$ Kg/m^3	η/mPa*s	D / 10^{-10} m^2/s		$\lambda/10^{-3}$ S cm^{-1}
			cation	anion	
[emim][C(CN)$_3$][13,14]	1.110^{293K} 1.060^{298K}	18^{295K}			18^{293K} 21.7^{298K}
[emim][B(CN)$_4$][15-17]	1.036^{298K} 1.005^{338K}	19.8^{293K} 6.8^{333K}			15.7^{298K} 25.8^{333K}
[emim][DCA] [18]	1080^{298K}	17$^{293.15K}$ 6.5^{333K}			28.4^{298K} 55.7^{333K}
[bmim][DCA][18-20]	1.058^{298K} 1.019^{363K}	33.2 $^{293.15K}$ 3.8$^{363.15K}$			11^{298K} 24.1^{333K}
[pyr$_{12}$][DCA] [18]	1.060^{298K}	25.8^{298K} 9.8^{333K}			20.1^{298K} 39^{333K}
[emim][BF$_4$][21,22]	1.280^{298K}	38.0^{298K}	0.497^{298K}	0.416^{298K}	13.6-15.7^{298K}
[emim][FSI][23]		15.5^{298K}			15.4^{298K}
[bmmim][Ntf$_2$][24]	1420^{298K}		0.198^{298K}	0.152^{298K}	1.6^{298K}
[N$_{1114}$][Ntf$_2$][25,18]	1393^{298K}	99.0^{298K}	0.131^{298K}	0.117^{298K}	2.05^{298K}
[mor1,4][Ntf$_2$][26]	1.440^{298K}	532^{298K}			0.40^{298K}
[emim][SO$_3$C$_4$H$_9$][27]	1.14287^{298K} 1.13343^{313K} 1.12097^{333K}	531.41^{296K} 175.52^{312K} 23.88^{359K}			
[bmim][CF$_3$SO$_3$][28]	1.302^{298K} 1.274^{333K} 1.226^{393K}	84.2^{298K} 21.7^{333K}	0.179^{298K} 0.690^{298K}	0.143^{298K} 0.590^{298K}	2.88^{298K} 9.49^{333K}
[pyr$_{13}$][FSI][23,29]		39-40^{298K}			6.4^{298K}, 8.2^{298K}
[pyr$_{13}$][Ntf$_2$][30-32]	1384^{333K} 1343^{393K}	61^{298K}	0.26^{298K}	0.17^{298K}	3.9^{298K} 3.55^{297K} 6.42^{333K}

difference of this polarizable force field with other nonpolarizable force field. As for most atomistic force fields, the APPLE&P force field includes terms describing valence interactions (bond and bends vibrations, dihedral potential, and out-of-plane deformation) and nonbonded interactions (all intermolecular and intramolecular for atoms separated by three bonds or more). The nonbonded interactions include van der Waals interactions (expressed by Buckingham exponential-6 potential) and electrostatic interactions. The latter, in addition to typical interactions due to fixed partial atomic charges, also include interactions between and with induced point dipoles centered on each atom (see eq (2-10)), making APPLE&P potential different from other nonpolarizable force fields. Below, we will refer to all polarizable models as "POL".

For the nonpolarizable model in this work, all valence and van der Walls interactions were kept the same as in a polarizable force field; only the description of electrostatic interactions was approximated differently using pair wise interactions, i.e., the partial atomic charges were kept the same as in the pol force field while atomic polarizablilities were set to zero (α_i=0). In this case, no induced dipoles are created on the atoms, and therefore, electrostatic interactions are reduced only to interactions between fixed partial atomic charges. We refer this force field as "NP".

3.2.3. Simulation Protocol

A version of the MD simulations package *Lucretius*, which has the capability to handle polarization effects, was used for all MD simulations. Three dimensional, periodic cubic simulation cells consisting of 100 – 180 ion pairs were simulated for all ILs. The exact number of ion pairs in each simulation is given in the Table 3-2. Covalent bond lengths were constrained using the velocity-Verlet form of the SHAKE algorithm.[33] The

Table 3-2: Density (ρ) and heat of vaporization ($\Delta H_{vap,}$) obtained from MD simulations using polarizable (POL) and nonpolarizable (NP) force fields at specified temperature and atmospheric pressure[a]

Ionic Liquids (# of ion pairs)	T,K	ρ(exp) Kg/m^3		δ, %	ΔH_{vap} KJ/mole		δΔH_{vap}, %
		POL	NP		POL	NP	
[emim][C(CN)$_3$]	298	1071	1043	-2.6	134.9	153.0	13.4
(125)	393	1007	978	-2.9	126.5	144.3	14.1
[emim][B(CN)$_4$]	298	1059	1030	-2.7	137.7	152.5	10.7
(150)	393	990	960	-3.0	127.8	143.5	12.3
[emim][DCA]	298	1077	1059	-1.66	125.9	153.3	21.8
(180)	393	1018	1000	-1.78	/	145.2	/
[bmim][DCA]	298	1042	1028	-1.4	132.1	159.4	20.7
(150)	393	986	969	-1.7	122.7	149.1	21.5
[pyr$_{12}$][DCA]	298	1032	1019	-1.3	133.3	172.5	29.4
(150)	393	977	964	-1.3	127.9	165.2	29.2
[emim][BF$_4$]	298	1262	1259	-0.24	135.1	174.1	29.1
(150)	393	1196	1187	-0.75	/	120.5	/
[emim][FSI]	298	1379	1371	-0.57	144.3	178.9	24.8
(125)	393	1312	1295	-1.30	/	168.6	/
[bmmim][Ntf$_2$]	298	1411	1403	-0.59	132.9	152.7	19.4
(150)	393	1332	1318	-1.07	/	145.2	/
[N$_{1114}$][Ntf$_2$]	298	1408	1397	-0.75	153.1	179.2	17.7
(150)	393	1325	1316	-0.71	/	167.5	/
[mor1,4][Ntf$_2$]	298	1433	1422	-0. 8	159.6	182.8	14.6
(150)	393	1356	1342	-1.0	147.0	170.0	15.6
[emim][SO$_3$C$_4$H$_9$]	298	1134	1117	-1.4	143.5	177.2	23.4
(100)	393	1069	1056	-1.5	131.8	165.6	25.7
[bmim][CF$_3$SO$_3$]	298	1291	1279	-0. 9	-142.7	-171.8	20.3
(150)	393	1217	1205	-1.0	-132.2	-162.2	22.7
[pyr$_{13}$][FSI]	298	1302	1290	-0.92	147.1	177.8	21.1
(216)	393	1233	1221	-0.97	/	/	
[pyr$_{13}$][Ntf$_2$]	298	1424	1417	-0.49	152.7	177.1	16.0
(216)	393	1352	1336	-1.2	132.8	164.7	24.0

[a] Deviations δX is defined as (X_{NP}-X_{POL})/X_{POL}*100. Also specified is the number of molecules or ion pairs (*N*) used in MD simulations. Uncertainties for reported properties are less than 2.0 kg/m^3 for densities and less than 0.5 kJ/mol for $\boldsymbol{\Delta H_{vap}}$.

Ewald summation method was used for treatment of long-range electrostatic forces between partial charges and between partial charges and induced-dipoles (for polarizable models) using κ^3 from 6^3 to 8^3 κ–vectors, and α from 8.5 to 9 Å. In simulations using polarizable models, a tapering function[34] was used to drive the induced-dipole/induced-dipole interactions to zero at a cutoff of 11 Å. A cutoff of R_{cutoff} = 10.5 or 11 Å was used for van der Waals interactions and the real part of electrostatic interactions in the Ewald summation. A multiple time step integration[35] with an inner time step of 0.5 fs (bonded interactions), a central time step of 1.5 fs for all nonbonded interactions with a truncation of $R1_{cutoff}$ = 6.0 Å or 6.5 Å, and outer time step of 3.0 fs for all nonbonded interactions between $R1_{cutoff}$ and distance of 10.5 Å or 11.0 Å, as well as for the reciprocal part of Ewald was employed. Each system was initially equilibrated in the NPT ensemble for at least 1 ns and the average box size from the NPT runs were utilized in the subsequent NVT production runs for all ILs. The length of production run was always long enough to achieve the diffusive regime in ILs and ranged from 50 to 150 ns. A Nose-Hoover thermostat[36] (NPT and NVT simulations) and a barostat[37] (NPT simulations) were used to control the temperature and pressure with the associated frequencies of 0.01 fs^{-1} and 0.005 fs^{-1}. Induced dipoles were calculated via a direct interaction with a predictor method.

Brownian dynamics simulations of ion pairs were performed for 1-4 ns to yield gas phase ion pair energies. The number of simulated ion pairs was the same as in the simulation box used for simulating the liquid phase.

3.3. Results and Discussion

3.3.1 Thermodynamic Properties

Table 3-2 summarizes the density (ρ) and heat of vaporization (ΔH_{vap}) (defined as a heat required to evaporate an ion pair from a liquid phase) of the selected ILs predicted from MD simulations using the POL and NP force fields at specified temperature and atmospheric pressure. As can be seen from Table 3-2, underestimation of density and heat of vaporization typically observed for nonionic liquids from MD simulations using NP models is also noticed in results from nonpolarizable ionic liquid models but to a smaller extend. The inability to induce additional dipoles in simulations with the NP force field is blamed to result in the reduction of the average molecular dipole moments (Table 3-3) and hence reduced intermolecular interactions in these liquids, which in turn leads to lower density and ΔH_{vap}. The relatively small reduction ($\leq$ 3%)of density in ILs predicted from NP models are expected because, in ILs, ionic interactions are much more dominant than the dipole-dipole interactions, therefore, the reduction of average dipoles would not significantly affect the strength of intermolecular interactions, resulting in much smaller changes in density. Interestingly, compared with other ILs, those containing cyano group show larger deviations between densities from POL model and NP model, indicating that inclusion of polarization may be relatively important in MD simulation study of ILs containing cyano group.

Considering the reduction of average molecular dipole moments (Table 3-3) and density, heat of evaporation for the NP model would be smaller compared to simulations with the POL force field. Table 3-2, however, shows that upon turning off polarization interactions, ΔH_{vap} increases by about 10-30%, a trend qualitatively opposite to what we

have observed for nonionic liquids. To fully understand this trend, it is instructive to compare average molecular dipoles in the liquid and gas phases from two force fields.

In Table 3-3, we list the average molecular dipoles obtained from liquid phase MD simulations at 393 K using both NP and POL models. Also shown is the average molecular dipoles obtained from the gas phase simulations of [pyr_{13}][NTF2] at 393 K using NP and POL models. Other ILs in gas phase showed similar trends, and therefore, are not shown. For the NP force field, the molecular dipole moment (defined relative to the ion center of mass) is determined by the distribution of fixed partial atomic charges (the same for all models) and population of molecular conformations. For the POL force field, an additional contribution from induced atomic dipoles should also be taken into account in the calculation of molecular dipoles. The average molecular dipole moments obtained from simulations using the NP force field do not show any noticeable changes between the two phases due to very similar population of molecular conformations in both phases. A relatively large difference of the average molecular dipole moments, however, is noticed between the two phase simulated using POL model. Here we take [pyr_{13}][Ntf_2] IL as an example to understand the increase of ΔH_{vap} upon turning off polarization. As can be seen in Table 3-3, the NP model predicts slightly lower average molecular dipole moments in liquid phase than POL model for both cations and anions. However, turning off polarization in gas phase simulations leads to significant changes in average molecular dipole moments, -27.2% and -64.7% for pyr_{13} and FSI, respectively, resulting in significant reduce in interactions between ion pairs. In the condensed phase, polarization between a pair of ions is compensated by polarization effects from other surrounding ions, leading to partial cancellation of the polarization contribution to

Table 3-3: Average Molecular Dipole Moment in Debye, As Obtained from Liquid Phase and Gas Phase Simulations for [pyr_{13}][FSI] IL at 393K and Atmospheric Pressure

ILs	Molecular Dipole Moment in Debye					
	Cation			Anion		
	POL	**NP**	**POL/NP**	**POL**	**NP**	**POL/NP**
[pyr_{13}][FSI]	2.21	2.11	**1.05**	1.34	0.86	**1.56**
[pyr_{13}][FSI] (gas)	2.83	2.06	**1.37**	3.12	1.10	**2.92**

molecular dipoles, whereas in gas phase ions are only influenced by the paired one. Other ILs in gas phase showed similar trends and, therefore, are not shown. The relatively weak interactions for the cation-anion pairs in gas phase simulations is the primary reason for the substantially larger values of ΔH_{vap} from the NP models listed in Table 3-2.

3.3.2. Transport Properties

In order to investigate the influence of turning off polarization on dynamic properties obtained from MD simulation, we start our analysis with comparison self-diffusion coefficient (D) of ions calculated from the Pol and NP force fields. Table 3-4 reports the self-diffusion coefficients of ions obtained from simulations using POL and NP force fields. Different from results for the nonionic liquids where absence of polarization results in faster dynamics, ion self-diffusion coefficient calculated from simulations using the NP force field are slower (D_{POL}/D_{NP} ranging from 1.3 to 7.4) than those obtained from simulations using the POL force field. Interestingly, the reduced liquid density and weaker intermolecular interactions in NP model do not necessarily lead to a fast dynamics in ionic liquid systems. There was attempt to correlate thermodynamic properties to the transport properties,[38] that is, the faster dynamics predicted by the POL

Table 3-4: Self-Diffusion Coefficients (D, in 10^{-10} m^2/s) Obtained from MD simulations Using Polarizable (POL) and Nonpolarizable (NP) Force Fields[a]

IL	T K	Cation			Anion		
		POL	NP	D_{POL}/D_{NP}	POL	NP	D_{POL}/D_{NP}
[emim][$C(CN)_3$]	298	0.649	0.337	1.93	0.702	0.356	1.88
	393	5.48	3.95	1.35	6.08	4.16	1.47
[emim][$B(CN)_4$]	298	0.318	0.237	1.30	0.292	0.215	1.27
	393	4.24	3.69	1.24	3.62	3.21	1.23
[emim][DCA]	298	0.91	0.46	2.0	1.08	0.47	2.3
	393	6.63	3.87	1.7	6.90	4.51	1.5
[bmim][DCA]	298	0.37	0.137	2.47	0.45	0.166	2.80
	393	4.08	2.40	1.60	4.60	2.95	1.60
[pyr12][DCA]	298	0.230	0.043	5.35	0.478	0.107	4.47
	393	2.45	0.993	2.35	4.09	1.93	2.22
[emim][BF_4]	298	0.48	0.12	4.0	0.36	0.12	3.0
	393	3.95	2.09	1.9	3.34	1.52	2.4
[emim][FSI]	298	0.76	0.21	3.6	0.68	0.21	3.2
	393	4.20	2.58	1.6	3.85	2.11	1.8
[bmmim][Ntf_2]	298	0.22	0.059	3.73	0.18	0.048	3.75
	393	2.68	1.24	2.2	2.33	0.87	2.7
[N_{1114}][Ntf_2]	298	0.12	0.027	4.44	0.11	0.025	4.40
	393	1.96	0.71	2.8	1.61	0.87	1.9
[mor1,4][TFSI]	298	0.038	0.010	3.80	0.043	0.009	4.88
	393	1.21	0.536	2.37	1.31	0.590	2.20
[emim][$SO_3C_4H_9$]	298	0.050	0.011	5.36	0.032	0.005	7.40
	393	1.68	0.641	2.55	1.19	0.331	3.47
[bmim][CF_3SO_3]	298	0.112	0.025	4.46	0.093	0.016	5.72
	393	2.06	0.917	2.19	1.68	0.680	2.48
[pyr_{13}][TFSI]	298	0.183	0.043	4.52	0.125	0.043	5.39
	393	2.49	1.00	2.24	1.79	0.826	2.20
[pyr_{13}][FSI]	298	0.18	0.041	4.39	0.20	0.050	4.00
	393	1.85	0.62	3.0	2.20	0.84	2.6

[a] Also shown is the ratio of self-diffusion coefficients, D_{pol}/D_{NP}, obtained from simulations using polarizable and nonpolarizable force fields. Uncertainty of reported self-diffusion coefficients is <10%

model is consisting with the lower ΔH_{vap} obtained from this model, as compared to the NP model. However, as illustrated before, the smaller values of ΔH_{vap} obtained from POL model is primarily due to the stronger ionic pair interaction in the gas phase. The interactions within ion pairs in liquid phase are similar, with a slightly stronger interaction in the POL model. This apparent contradiction indicates that correlations between thermodynamic and transport properties might be more complex than suggested.

Compared with other ILs, ILs containing cyano group show similar or even much smaller changes ($\mathbf{D_{POL}/D_{NP}}$) in dynamics when polarization is turned off. Interestingly, among those cyano containing ILs, those consisting of DCA^- anion show relatively larger change in the self-diffusion coefficients calculated from MD simulations using the POL and NP force fields, in the sequence: $[emim][B(CN)_4] < [emim][C(CN)_3] < [emim][DCA] < [bmim][DCA] < [pyr_{12}][DCA]$. Table 3-4 also shows that the $\mathbf{D_{POL}/D_{NP}}$ has noticeable temperature dependence, that is, the ratio significantly increases as the temperature decreases. This observation also supports the conclusion that turning off polarization not only results in systematic slowing down of ion translational motion but also changes its temperature dependence. If temperature dependence of self-diffusion coefficients follows the rule of Arrhenius behavior ($D(T)=D_0\exp(-E_a/RT)$, then different activation energies (E_a) will be expected from POL and NP models.

Before move to next discussion, it would be interesting to discuss the computational expense by using this APPLE&P force field. Generally, simulations with polarizable force fields are a factor of 3-4 computational more expensive than with nonpolarizable force fields. However, if dynamics in simulations using NP force field is a factor of 2-4 slower, then accessing the same extent of structural relaxation (characterized by

molecular displacements) with the NP model would require 2 - 4 times longer trajectories than those with POL model. Hence, computational expenses for the POL and NP models are almost equivalent, albeit more accurate dynamics are predicted using the POL model.

To further understanding the role of polarization in dynamics of ILs, we also calculated the ion rotational dynamics. For each molecule, a local coordinate system has been defined, and a rotational autocorrelation function (ACF) for each unit vector $\mathbf{e}_i$ (i= {x, y,z}) defining this local coordinate system has been calculated as

$$\mathrm{ACF}_i(\mathrm{t}) = < [e_i(0) \cdot e_i(\mathrm{t})] > \tag{3-1}$$

where $e_i(0)$ and $e_i(\mathrm{t})$ are the values of the unit vectors at time zero and *t*, respectively, and brackets denote the ensemble average over all molecules of the same type and time origins. The obtained ACFs were fitted with Kohlrausch-Williams-Watts (KWW) functions given by

$$P_{KWW}(t) = A \exp(-\left(\frac{t}{t_r}\right)^{\beta}) \tag{3-2}$$

where t_r is a relaxation time parameter, parameter β determines the degree of stretching and characterizes the broadness of the relaxation process, and prefactor A allows us to account for decay that occurs on time scales faster than 1 ps^{-1}. Rotational relaxation time (τ) were obtained by integrating eq 3-2 over time from zero to infinity and are given in Table 3-5 for all ILs at 393K. For all the selected ILs, the rotational relaxation time increase when polarization effect is removed, i.e. the rotational dynamics slows down. However, slowing down of rotational dynamics upon tuning off polarization is significantly less pronounced than what was observed for translational motion characterized by the ion self-diffusion coefficients in Table 3-4. Interestingly, when polarization is turned off anions containing cyano groups show less change in rotational

Table 3-5: Rotational Relaxation Time t (ps) Obtained from MD Simulation at 393K using POL and NP Force Fields[a]

IL		Cation			Anion		
		τ_x	τ_y	τ_z	τ_x	τ_y	τ_z
[emim][$C(CN)_3$]	POL	33.5	14.2	16.8	21.4	21.2	18.9
	NP	38.0	15.2	19.3	25.1	24.9	22.7
	τ_{POL}/τ_{NP}	**0.88**	**0.93**	**0.87**	**0.85**	**0.85**	**0.83**
[emim][$B(CN)_4$]	POL	37.4	14.7	17.8	28.6	28.7	28.2
	NP	38.7	14.6	18.8	28.6	28.5	28.6
	τ_{POL}/τ_{NP}	**0.97**	**1.01**	**0.95**	**1.0**	**1.01**	**0.99**
[emim][DCA]	POL	34.9	14.8	16.6	17.1	1.29	1.20
	NP	46.9	17.6	21.1	24.4	1.51	1.41
	τ_{POL}/τ_{NP}	**0.74**	**0.84**	**0.78**	**0.70**	**0.85**	**0.85**
[bmim][DCA]	POL	33.9	73.3	28.1			
	NP	43.4	109.6	34.0			
	τ_{POL}/τ_{NP}	**0.78**	**0.67**	**0.83**			
[pyr_{12}][DCA]	POL	9.8	17.8	12.0			
	NP	11.9	25.1	15.0			
	τ_{POL}/τ_{NP}	**0.82**	**0.71**	**0.80**			
[emim][BF_4]	POL	48.1	20.9	22.4	1.3		
	NP	78.2	28.4	31.0	1.6		
	τ_{POL}/τ_{NP}	**0.62**	**0.74**	**0.72**	**0.81**		
[emim][FSI]	POL	39.7	14.6	16.5	13.3	4.0	4.2
	NP	55.1	18.0	21.2	18.8	4.5	4.3
	τ_{POL}/τ_{NP}	**0.72**	**0.81**	**0.78**	**0.71**	**0.89**	**0.97**
[bmmim][Ntf_2]	POL	61.3	78.1	57.2	50.7	12.8	16.1
	NP	97.8	131.2	84.6	81.8	16.7	18.9
	τ_{POL}/τ_{NP}	**0.63**	**0.60**	**0.68**	**0.62**	**0.77**	**0.85**
[N_{1114}][Ntf_2]	POL	97.6			62.1	14.9	21.4
	NP	192.0			126.3	22.0	26.3
	τ_{POL}/τ_{NP}	**0.51**			**0.49**	**0.68**	**0.81**

Table 3-5. Continued

IL		Cation			Anion		
		τ_x	τ_y	τ_z	τ_x	τ_y	τ_z
$[mor_{14}][TFSI]$	POL	50.8	172.7	118.6	93.5	20.8	29.6
	NP	69.4	293.8	212.4	173.6	29.7	33.9
	τ_{POL}/τ_{NP}	**0.73**	**0.59**	**0.56**	**0.54**	**0.70**	**0.87**
$[emim][SO_3C_4H_9]$	POL	144.7	85.9	79.0			
	NP	265.2	120.7	116.3			
	τ_{POL}/τ_{NP}	**0.55**	**0.71**	**0.68**			
$[bmim][CF_3SO_3]$	POL	171.1	49.3	47.1			
	NP	305.7	71.3	65.2			
	τ_{POL}/τ_{NP}	**0.56**	**0.69**	**0.72**			
$[pyr_{13}][TFSI]$	POL	19.2	48.4	34.4	60.9	13.7	16.3
	NP	20.9	72.5	45.8	106.1	18.2	19.1
	τ_{POL}/τ_{NP}	**0.92**	**0.67**	**0.75**	**0.57**	**0.75**	**0.85**
$[pyr_{13}][FSI]$	POL	18.7	50.6	29.9	18.3	5.6	4.8
	NP	22.1	87.9	41.6	32.8	6.2	5.9

[a]Also shown are the ratios of rotational relaxation times.

dynamics than other anions does, indicating that rotational dynamics is relatively less contributed by induced dipole moments. Actually, rotational dynamics of $B(CN)_4^-$ in the NP models almost keeps the same as in POL models and the rotational relaxation time for $C(CN)_3^-$ in the POL models is about only 0.15 times shorted than that in NP models.

Viscosity extracted from MD simulations using NP and POL force fields are summarized in Table 3-6. Upton turning off the polarization, viscosity is significantly overestimated for all the selected ILs. It is interesting to note that the viscosity of [emim][$B(CN)_4$] predicted from NP model is slightly higher than that from POL model, with deviation of only 3%. For other ILs, however, viscosities calculated from simulations using NP force field increase by factors ranging from 1.5 to 5. Viscosity of

Table 3-6: Viscosity (in mPa*s) of ILs predicted from MD Simulations Using POL and NP Force Fields.

ILs	T, K	η_{POL}	η_{NP}	η_{NP}/η_{POL}
[emim][$C(CN)_3$]	393	2.4	3.5	1.5
	298	19.8	29.5	1.5
[emim][$B(CN)_4$]	393	3.3	3.4	1.0
	298	37.8	42.5	1.1
[emim][DCA]	393	2.2	4.77	2.2
	298	13.3	25.2	1.9
[bmim][DCA]	393	3.1	5.4	1.7
	298	24.6	67.3	4.1
[P12][DCA]	393	4.85	16.8	3.5
	298	45	210.7	4.7
[mor_{14}][TFSI]	393	9.5	23.3	2.5
	298	235	903.4	3.8
[emim][$SO_3C_4H_9$]	393	10.1	25.6	2.5
	298	264.4	908.2	3.4
[bmim][CF_3SO_3]	393	7.8	18.1	2.3
	298	90	273.4	3.0
[pyr_{13}][TFSI]	393	6.1	12.1	2.0
	298	61	176.4	2.9

[emim][NO_3] obtained from a nonpolarizable model developed by Yan also showed ~ 50% larger than that extracted from polarizable model. Therefore, we believe the electronic polarization effects decrease the viscosity in the system and bring the predicted viscosity into much closer agreement with the experimental results.

3.3.3 Structural Properties

In this section we will discuss the difference in structural correlations obtained from MD simulations using the POL and NP force fields. Here we are focusing on the analysis of molecular structure, by which we hope to find explanations for observed differences in dynamical correlations obtained from simulations using the two models. Figure 3-2 shows cation-cation ($g^{++}(r)$), cation-anion ($g^{+-}(r)$), and anion-anion ($g^{--}(r)$) center-of-mass radial distribution functions for the ILs investigated in this work, at 393K and atmospheric pressure. As can be seen, in Figure 3-2, for almost all correlations the peaks of g(r) obtained from simulations using the NP model are narrower and higher as compared to those obtained using the POL model except the g(r) of emim-anion, indicating systems modeled with the NP force field showed more structuring or stronger spatial correlations between ions. In particular, significant deviations are noticed in $g^{--}(r)$ from simulations using POL force field and NP force field. The stronger spatial correlation is generally contributed by stronger intermolecular interactions between ions. However, the inability to induce additional dipoles in simulations with the NP force field actually results in weaker interactions between ions as we discussed before due to reduced average molecular dipole moments, therefore, as in the case of dynamics, the more structuring of ILs in simulations with the NP force field is unexpected. Interestingly, $g^{--}(r)$ obtained from simulations using POL and NP force fields for anions containing

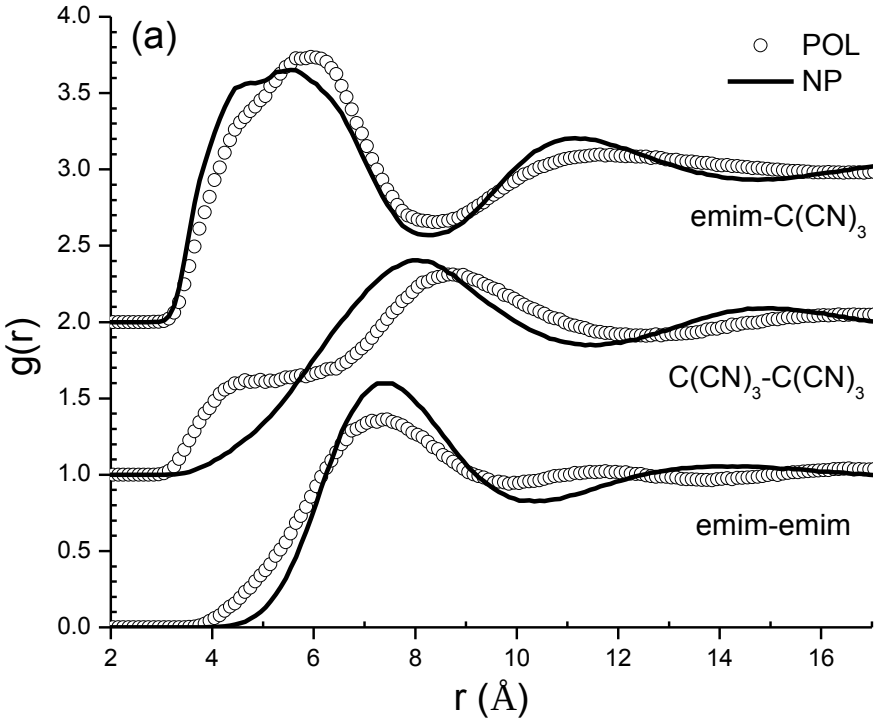

Figure 3-2. Molecular center-of-mass cation-cation, cation-anion, and cation-anion radial distribution functions (g(r)) obtained from simulations using POL and NP force fields for [emim][$C(CN)_3$] (a), [emim][$B(CN)_4$] (b), [emim][DCA] (c), [bmim][DCA] (d), [P12][DCA] (e), [mor1,4][TFSI] (f), [emim][$SO_3C_4H_9$] (g), [P13][TFSI] (h), [bmim][CF_3SO_3] (i) at 393K and atmospheric pressure.

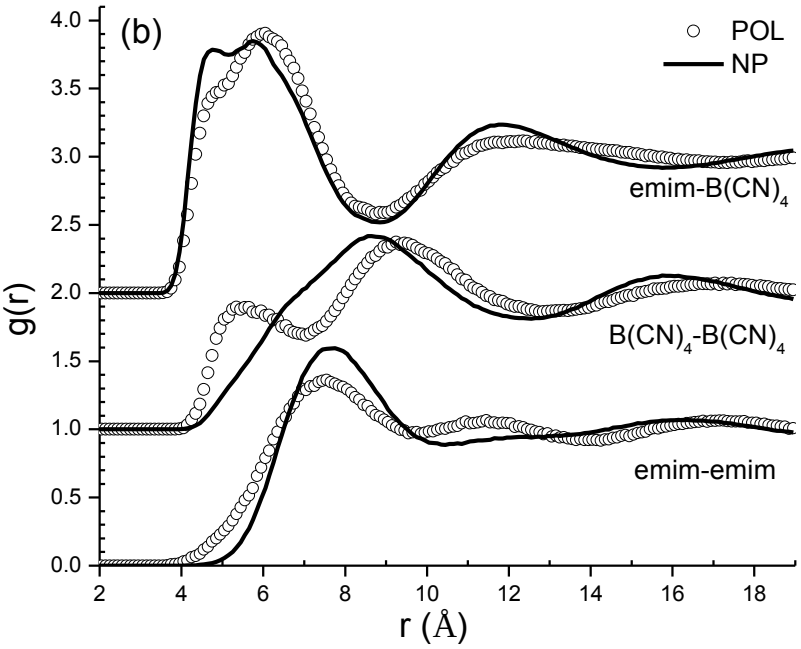

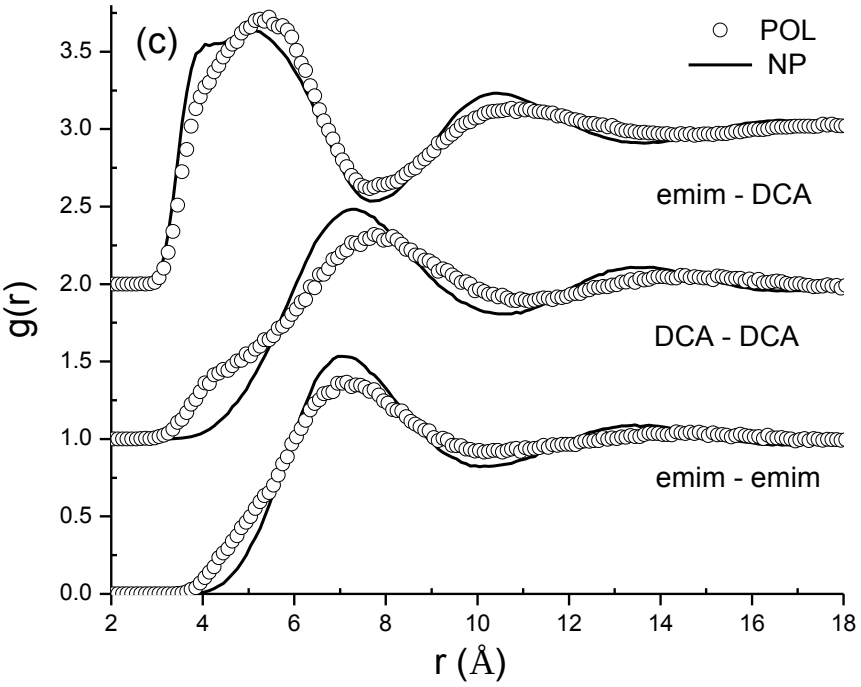

Figure 3-2. Continued

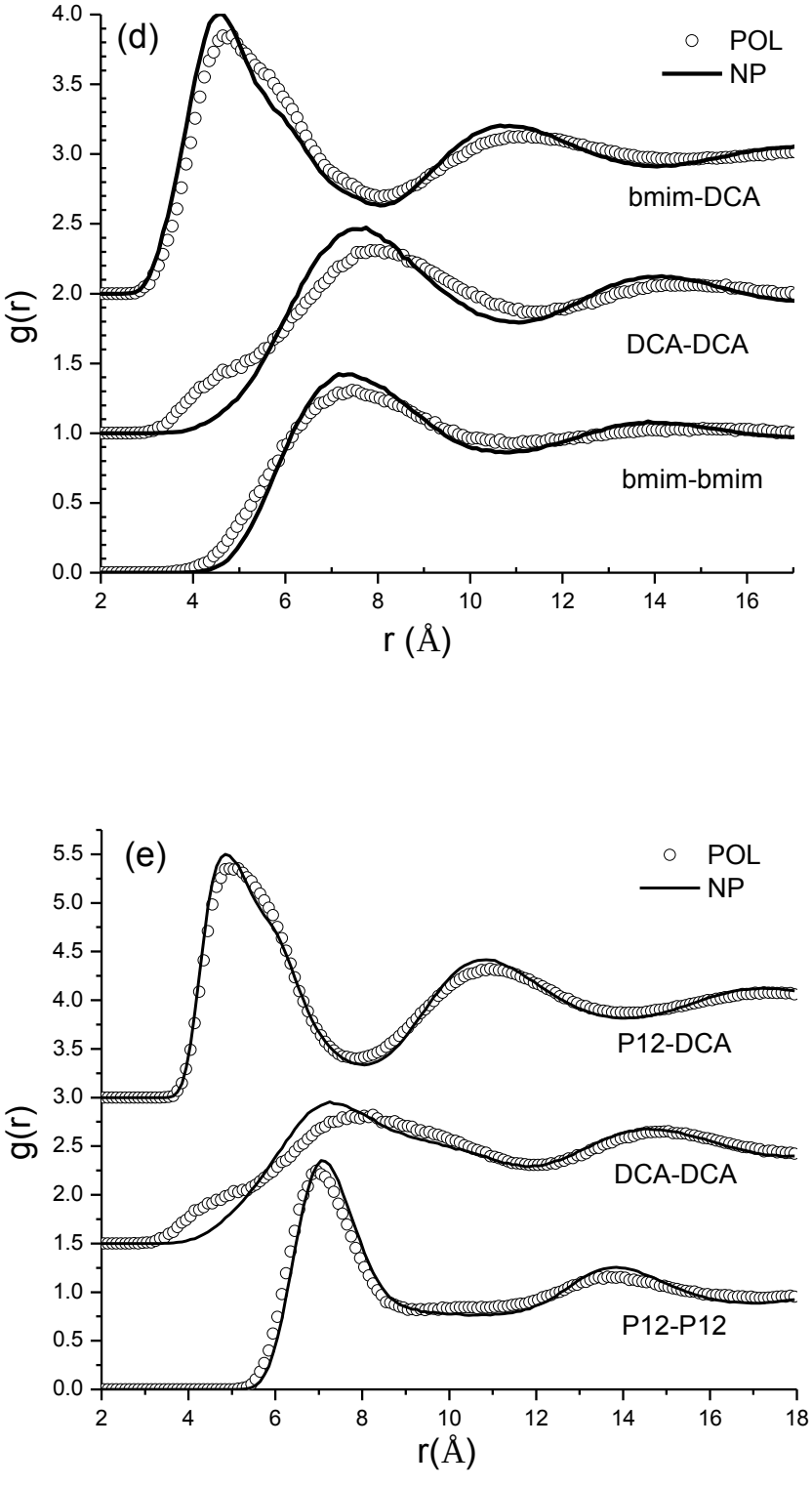

Figure 3-2. Continued

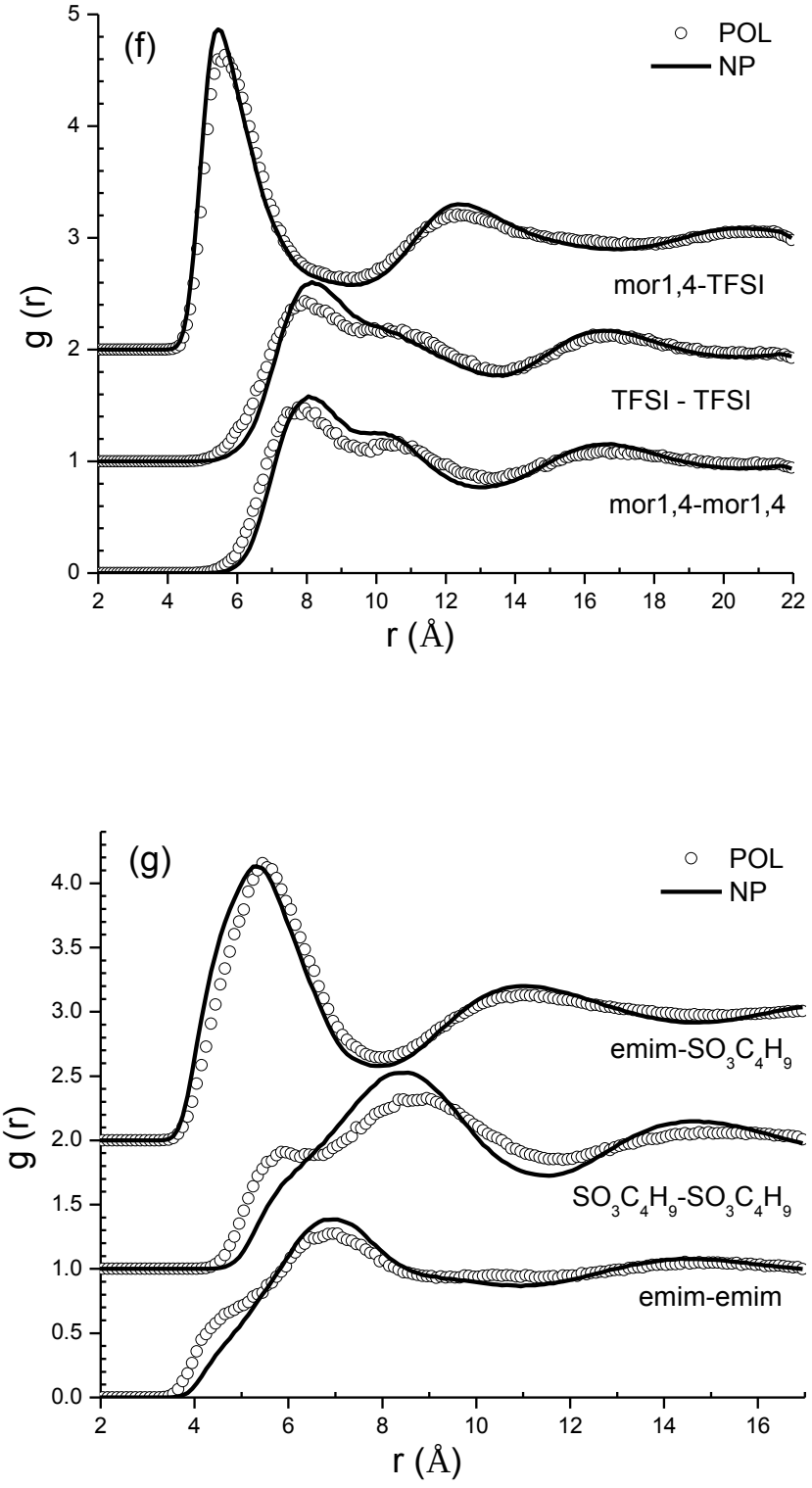

Figure 3-2. Continued

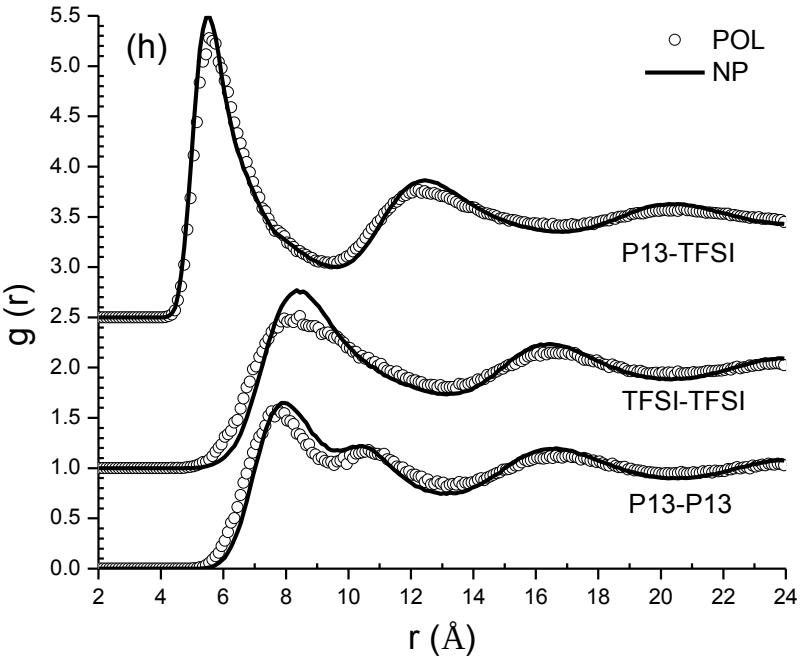

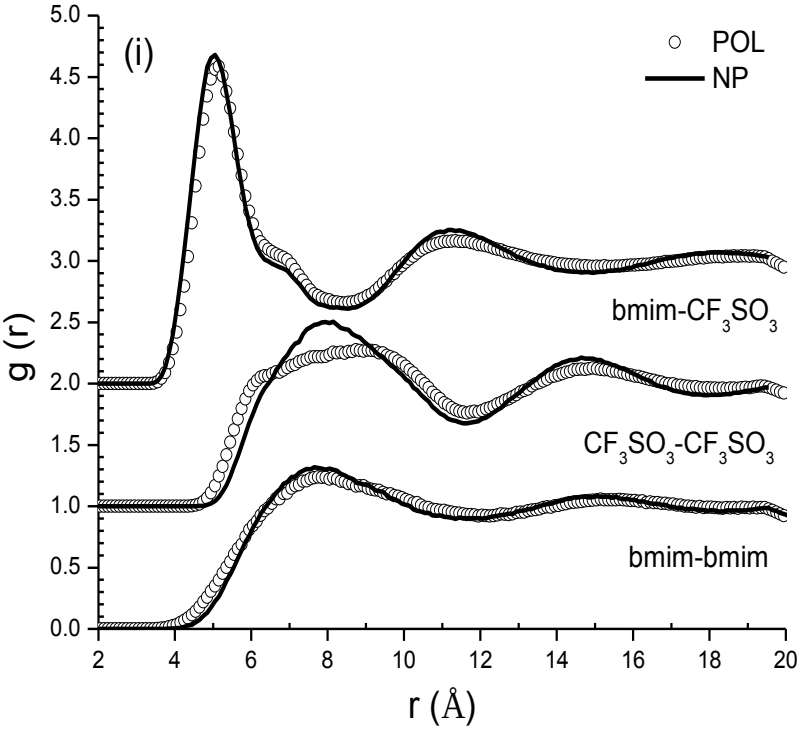

Figure 3-2. Continued

cyano group shows more significant changes, as compared with $g^{-}(r)$ for other anions, a completely opposite trend as observed in dynamics upon turning off polarization.

A further comparison of three dimensional (3-D) density distributions of selected anion atoms around a cation helps us well understanding the influence of turning off polarization on ILs' structure. Figure 3-3 shows isosurfaces for distribution of the anion's center atoms (N, B, C) around the relative cations. We compare several representative isosurfaces with different $\rho i/\langle\rho\rangle$, ranging from 3.0 to 5.0. The results shown here positively support our previous summation that the POL model provides more asymmetric interaction of ions in the bulk ILs, as compared to the NP model. At higher free energy isosurface $\rho_i/\langle\rho\rangle = 3.0$), for [bmim][DCA], simulations with the POL provide a continuous path above the N-C-N bend from one side of bmim to another, and simulations with the NP model have two disconnected isosurfaces. Besides this, a double layer of isofurface is noticed in the POL models above the N-C-N bend and under the two functional group methyl- and butyl-. The NP model does not show this double layer at all. At $\rho_i/\langle\rho\rangle = 4.0$, the double layer of isosurfaces calculated from the POL model almost disappears, making isofurfaces between two force fields are similar. However, at lower free energy isosurface, $\rho_i/\langle\rho\rangle = 5.0$, a pronounced difference between force fields appears. The POL model predicts that only two small regions besides the N-C-N bend are populated for this isosurface, and the other two regions under the two tail group are gone. As can be seen in Figure 3-3, similar behavior is observed for other ILs.

Correlations between the 3-D density distributions to dynamics predicted from simulations using the two different force fields have been proposed.[11] It suggests that the continuous path observed at the higher free energy (low density) isosurface should

Figure 3-3. Isosurface of 3-D density distribution of ions' center atoms around cation for[bmim][DCA] (a), [emim][$B(CN)_4$] (b), [emim][$C(CN)_3$] (c), [pyr_{12}][DCA](d), [mor1,4][TFSI] (e), [emim][$SO_3C_4H_9$] (f), [pyr_{13}][TFSI] (g), [bmim][CF_3SO_3] (h) obtained from simulations at 393K using POL (red wireframe) and NP(solid grey) models.

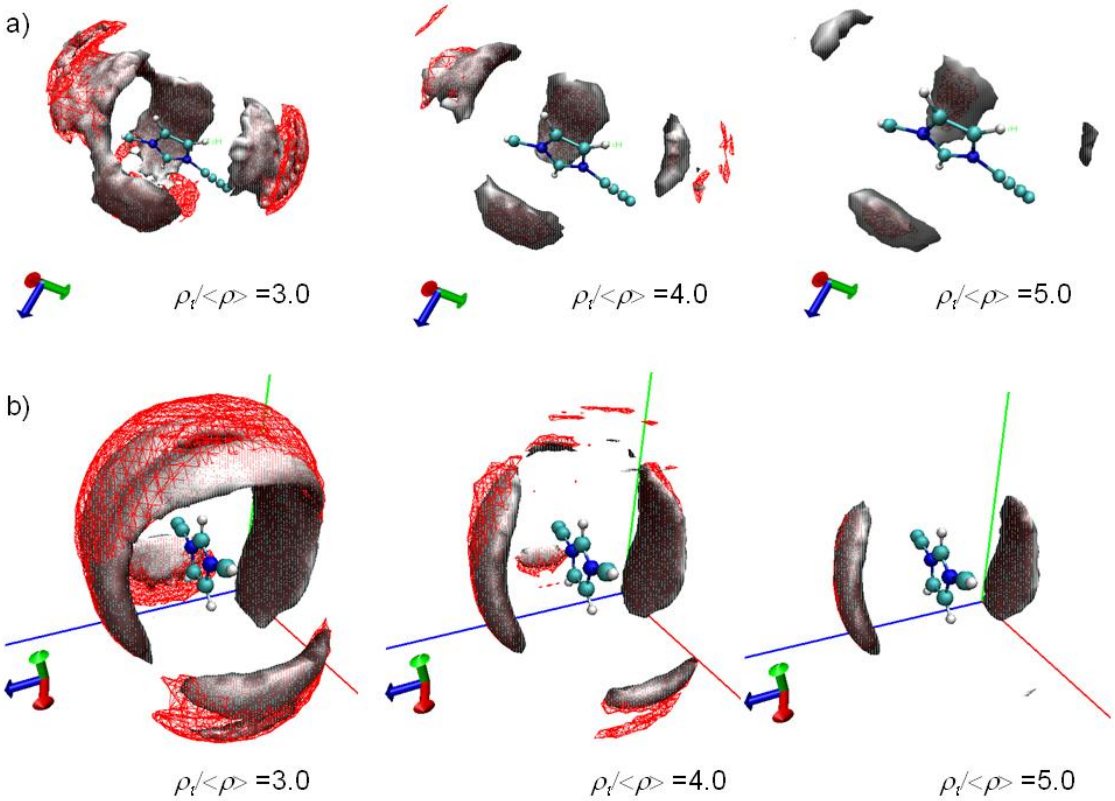
a)
$\rho_t/\langle\rho\rangle$ =3.0
$\rho_t/\langle\rho\rangle$ =4.0
$\rho_t/\langle\rho\rangle$ =5.0
b)
$\rho_t/\langle\rho\rangle$ =3.0
$\rho_t/\langle\rho\rangle$ =4.0
$\rho_t/\langle\rho\rangle$ =5.0

c)

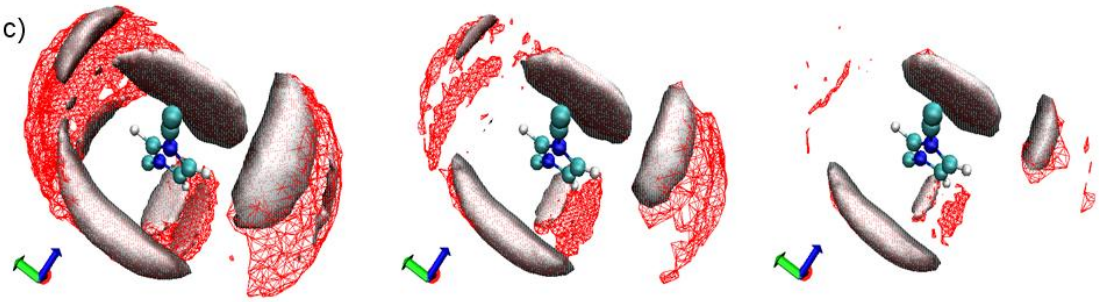

$\rho_t/\langle\rho\rangle$ =3.0 $\rho_t/\langle\rho\rangle$ =3.5 $\rho_t/\langle\rho\rangle$ =4.0

d)

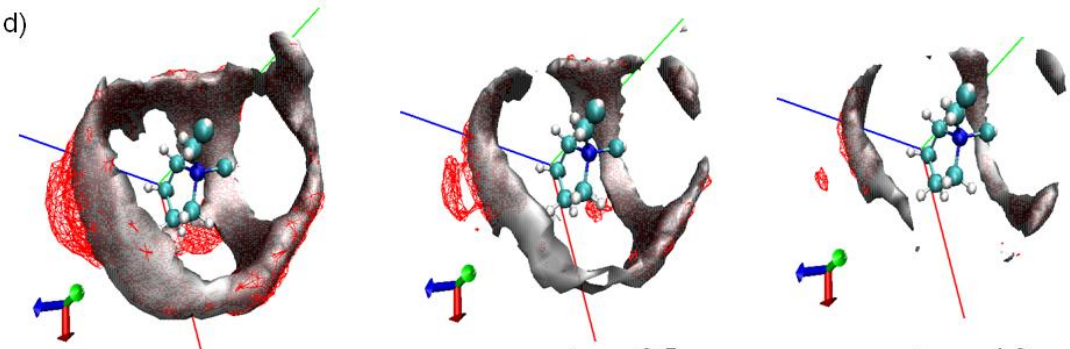

$\rho_t/\langle\rho\rangle$ =3.0 $\rho_t/\langle\rho\rangle$ =3.5 $\rho_t/\langle\rho\rangle$ =4.0

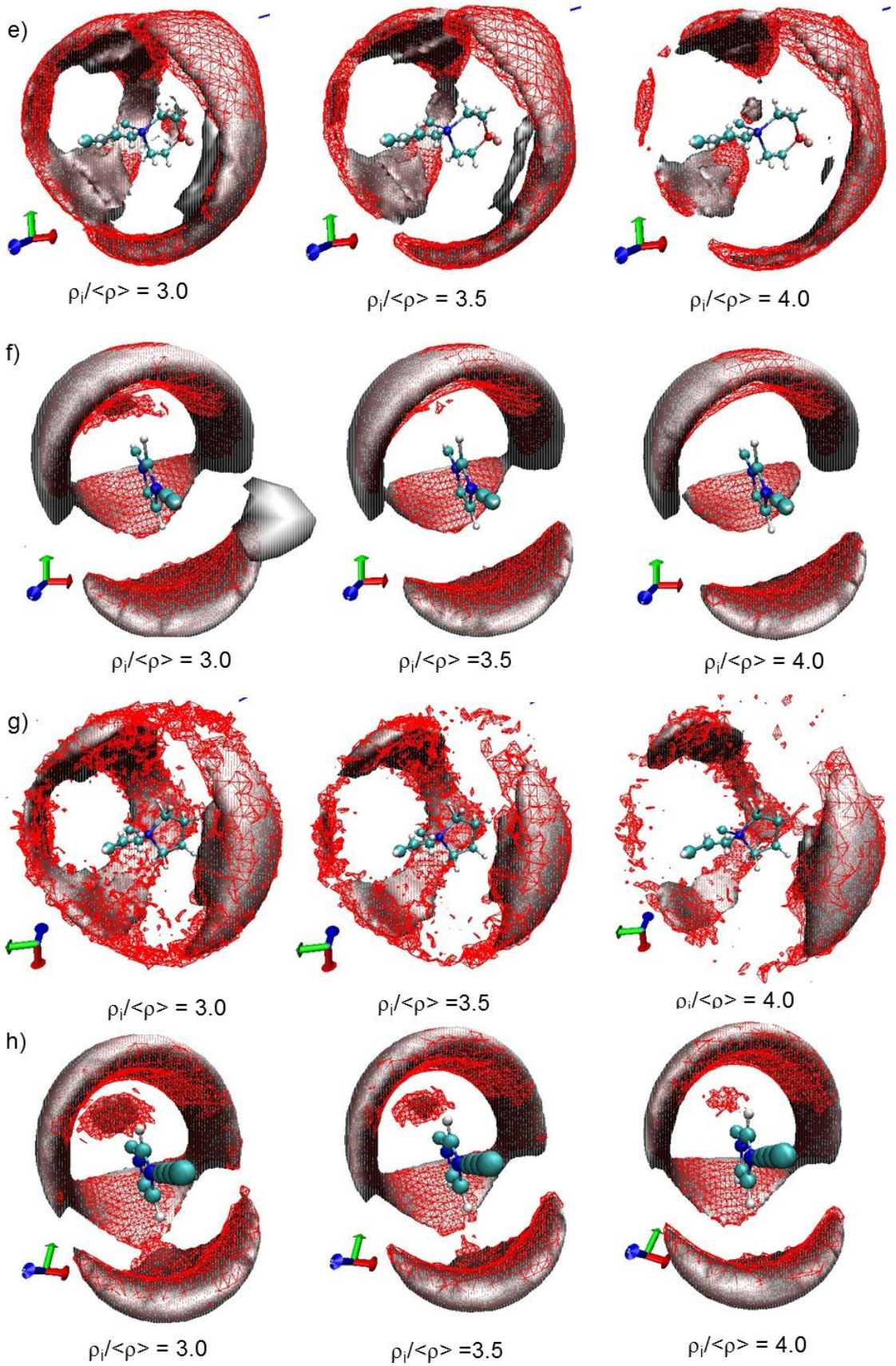
e)
$\rho_i/\langle\rho\rangle$ = 3.0
$\rho_i/\langle\rho\rangle$ = 3.5
$\rho_i/\langle\rho\rangle$ = 4.0
f)
$\rho_i/\langle\rho\rangle$ = 3.0
$\rho_i/\langle\rho\rangle$ =3.5
$\rho_i/\langle\rho\rangle$ = 4.0
g)
$\rho_i/\langle\rho\rangle$ = 3.0
$\rho_i/\langle\rho\rangle$ =3.5
$\rho_i/\langle\rho\rangle$ = 4.0
h)
$\rho_i/\langle\rho\rangle$ = 3.0
$\rho_i/\langle\rho\rangle$ =3.5
$\rho_i/\langle\rho\rangle$ = 4.0

facilitate the mobility of anions around the cation molecule for the POL model, while in the NP model the anion would need to overcome a larger free energy barrier to cross free energy isosurface $\rho_i/\langle\rho\rangle = 3.0$), for [bmim][DCA], simulations with the POL provide a continuous path above the N-C-N bend from one side of bmim to another, and simulations with the NP model have two disconnected isosurfaces. Besides this, a double layer of isofurface is noticed in the POL models above the N-C-N bend and under the two functional group methyl- and butyl-. The NP model does not show this double layer at all. At $\rho_i/\langle\rho\rangle = 4.0$, the double layer of isosurfaces calculated from the POL model almost disappears, making isofurfaces between two force fields are similar. However, at lower free energy isosurface, $\rho_i/\langle\rho\rangle = 5.0$, a pronounced difference between force fields appears. The POL model predicts that only two small regions besides the N-C-N bend are populated for this isosurface, and the other two regions under the two tail group are gone. As can be seen in Figure 3-3, similar behavior is observed for other ILs.

3.4. Conclusion

Utilizing the transferable, quantum-chemistry-based, Atomistic Polarizable Potential for Liqiuds, Electrolytes & Polymers (APPLE&P) force field, we have systematically investigated the influence of polarization effects on the MD simulation study of ionic liquids. Thermodynamic, dynamic, and structural properties predicted from the simulations using polarizable force field and nonpolarizable force field were thoroughly compared, from which we noticed that turning off polarization effects in ILs containing cyano group results in 10-30% increase in the enthalpy of vaporization but only 1.3-3.0% reduction in density. A factor of 2-5 slowing down in translational dynamics as compared to results from simulations using the polarizable force field was also observed. A factor

up to 5 increase of viscosity extracted from NP model are noticed for the cyano-containing ILs except [emim][$B(CN)_4$], whose viscosity is only 0.1 times larger than that calculated from POL model. This overestimation is expected based on reported viscosities predicted from simulations using the nonpolarizable force fields.

3.5. References

(1) Bhargava, B. L.; Balasubramanian, S. *J. Chem. Phys.* **2007**, 127, 114510.

(2) Cadena, C.; Anthony, J. L.; Shah, J. K.; Morrow, T. I.; Brennecke, J. F.; Maginn, E. J. *J. Am. Chem. Soc.* **2004**, 126, 5300.

(3) Zhao, W.; Leroy, F.; Heggen, B.; Zahn, S.; Kirchnner, B.; Balasubramanian, S.; Muller-Plathe, F. *J. Am. Chem. Soc.* **2009**, 131, 15825.

(4) Koddermann, T.; Paschek, D.; Ludwig, R. *ChemPhysChem* **2007**, 8, 2464.

(5) Chaban, V. V.; Prezhdo, O. V. Phys. *ChemPhys Chem* **2011**, 13, 19345.

(6) Borodin, O. *J. Phys. Chem. B* **2009,** 113, 11463.

(7) Aguado, A.; Wilson, M,; Maddane, P. A. *J. Chem. Phys.* **2001**, 115,8603.

(8) Morgan, B.; Maddane, P. A. *J. Chem. Phys.* **2004**, 120, 1402.

(9) Yan, T.; Burnhan, C. J.; Del Popolo, M. G.; Voth, G. A. *J. Phys. Chem. B* **2004**, 108, 11877.

(10) Yan, T.; Li, S.; Jiang, W.; Gao, X.; Xiang, B.; Voth, G. A. *J. Phys. Chem. B* **2006**, 110, 1800.

(11) Borodin, O. Materials Research Society Spring Meeting, San Francisco, **2008**; pp Q06-04.

(12) Bedrov, D. Borodin, O.; Li, Z.; Smith, G. D. *J. Phys. Chem. B* **2010**, 114, 4984.

(13) Zhang, S.; Sun, N.; He, X.; He, X.; Lu, X.; Zhang, X. *J. Phys. Chem. Ref. Data* **2006**, 35, 1475-1571.

(14) Yoshida, Y.; Moroi, K.; Otsuka, A.; Saito, G.; Takahashi, M.; Yoko, T. *Inorg. Chem.* **2004**, 43, 1458-1462.

(15) Tong, J.; Liu, Q. S.' Kong, Y. X.; Fang, D. W.; Welz-Biermann, U.; Yang, J. Z. *J. Chem. Eng. Data* **2010**, 55, 3693-3696.

(16) Pitner, W. R.; Ignat'ev, N. Ionic Liquids for Electrochemical Applications. 214th Electrochemical Society Meeting, Honolulu, Hawaii, October, 12-17,**2008**.

(17) Bai, Y.; Cao, Y. M.; Zhang, J.; Wang, M.; Li, R. Z.; Wang, P.; Zakeeruddin, S. M.; Gratzel, M. *Nat. Mater*. **2008**, 7, 626-630.

(18) Yoshida, Y.; Baba, O.; Saito, G. *J. Phys. Chem. B* **2007**, 111, 4742.

(19) Fredlake, C. P.; Crosthwait, J. <.; Hert, D. G.; Aki, S.; Brennecke, J. F. *J. Chem. Eng. Data* **2004**, 49 954-964.

(20) Sanchez, L. G.; Espel, J. R.; Onink, F.; Meindersma, W.; Haan, A. B. *J. Chem. Eng. Data* **2009**, 54, 2803-2812.

(21) Shiflett, M. B.; Yokozeki, A. *J. Chem. Eng. Data* **2007**, 52, 1302.

(22) Zhou, Z. B.; Matsumoto, H.; Tatsumi, K.; *ChemPhysChem* **2005**, 6, 1324.

(23) Matsumoto, H.; Sakaebe, H.; tatsumi, K.; Kikita, M.; Ishiko, E.; Kono, M. *J. Power Sources* **2006**, 160, 1308.

(24) Bazito, F. F. C.; Kawano, Y.; Torresi, R. M. *Electrochim. Acta* **2007**, 52, 6427.

(25) Tokuda, H.; Ishiii, K.; Susan, M. A. B. H.; Tsuzuki, S.; Hayamizu, K.; Watanabe, M. *J. Phys. Chem. B* **2006**, 110, 2833.

(26) Zhou, Z. B.; Matsumoto, H.; Tatsumi, K. *Chem.-Eur. J.* **2006**, 12, 2196.

(27) Blesic, M.; Swadźba-Kwaśny, M.; Belhocine, T.; Gunaratne, H. Q. N.; Lopes, J. N. C.; Gomes, M. F. C.; Pádua, A. A. H.; Seddon, K. R.; Rebelo, L. P. N. *Phys. Chem. Chem. Phys.* **2009**, 11, 8939.

(28) Tokuta, H,; Hayamizu, K.; Ishii, K.; Abu Bin Hasan Susan, M.; Watanabe, M. *J. Phys. Chem. B* **2004**, 108,16593.

(29) Wang, Y. D.; Zaghib, K.; Guerfi, A.; Bazito, F. F.C.; Torresi, R. M.; Dahn, J. R. *Electrochim. Acta* **2007**, 52, 6346.

(30) Nicotera, I.; Oliviero, C.; Henderson, W. A.; Appetecchi, G. B.; Passerini, S. *J. Phys. Chem. B* **2005**, 109, 22814.

(31) MacFarlane, D. R.; Meakin, P.; Sun, J.; Amini, N.; Forsyth, M. *J. Phys. Chem. B* **1999**, 103, 4164.

(32) Bayley, P. M.; Lane, G. H.; Rocher, N. M.; Clare, B. R.; Best, A. S.; MacFarlane, D. R.; Forsyth, M. *Phys. Chem. Chem. Phys.* **2009**, 11, 7201.

(33) Palmer, B. J. *J. Comput. Phys.* **1993**, 104, 470.

(34) Steinhauser, O. *Mol. Phys.* **1982**, 45, 335.

(35) Martyana, G. J.; Tuckerman, M.; Tobias, D. J. Klein, M. L. *Mol. Phys.* **1996**, 87, 1117.

(36) Nose, S. In Computer Simulation in Materials Science; Meyer, M., Pontikis, V., Eds.; Kluwer Academic Publishers: Netherlands, **1991**; p 21.

(37) Martyna, G. J.; Tuckerman, M.; Tobias, D. J.; Klein, M. L. *Mol. Phys.* **1996**, 87, 1117.

(38) Borodin, O. *J. Phys. Chem. B* **2009**, 113, 12353.

CHAPTER 4

LI^+ SOLVATION AND TRANSPORT PROPERTIES IN IONIC LIQUID/LITHIUM SALT MIXTURES: A MOLECULAR DYNAMICS SIMULATION STUDY

Note that the work presents in this chapter was reproduced from the paper accepted by The Journal of Physical Chemistry B (DOI: http://dx.doi.org/10.1021/jp3052246).

4.1. Introduction

Although RTILs consist solely of ions, these ions are typically not electroactive and thus for lithium ion battery applications must be doped with suitable lithium salts, such as [Li][PF_6], [Li][BF_4], [Li] [Ntf_2], or [Li][FSI]. The ability of RTILs to dissolve lithium salts and transport Li^+ cations positions them as competitors with liquid, gel and polymer electrolytes for secondary lithium batteries.[1,2]

Howlett and MacFarlane investigated [pyr_{13}] [Ntf_2] doped with [Li][Ntf_2] as an electrolyte for battery applications and found great cycling efficiency and uniform, non-dendritic deposition of lithium.[3] The phase behavior of (1-x)[pyr_{1R}][Ntf_2] (R=2-4)/x[Li][Ntf_2] mixtures was also investigated by Henderson et al.[4] The authors suggested that strong Li^+- Ntf_2 interactions, most likely between the Li^+ cations and anion oxygen,

exist in the crystal structures for all of the mixed $[pyr_{1R}][Ntf_2]/[Li][Ntf_2]$ phases. It is interesting to see that all the investigated pyrrolidinium-based RTILs formed stoichiometric 2/1 and 1/2 (pyr_{1R}/Li^+) crystalline phases with $[Li][Ntf_2]$. NMR characterization of $[pyr_{13}][Ntf_2]$ was later carried out by Nicotera et al. to investigate interactions between the RTIL and $[Li][Ntf_2]$ salt as well as transport properties of the electrolyte.[5] By examination of ^1H, ^1F, and^7 Li NMR spectra, the investigators noticed that interactions of the organic cations with Li^+ and anions is very weak compared to the interactions between Li^+ and the anions resulting in strong coordination between anions and Li^+. By evaluating the diffusion coefficient ratios of the cation and anion species D_{Li}^{obs}/D_F^{obs} of the lithium salt and D_H^{obs}/D_F^{obs} of the ionic liquid solvent, Saito et al. concluded that Li^+ cations are coordinated approximately by 3-4 anions, forming stable $(Li^+(Ntf_2)_n)^{(n-1)-}$ clusters in [1-butyl-2,3-dimethylimidazolium]$[Ntf_2]/[Li][Ntf_2]$ electrolytes.[6]

Borodin et al. conducted the first molecular dynamics (MD) simulation study of an RTIL doped with a lithium salt, specifically $[pyr_{13}][Ntf_2]$ RTIL doped with 25% mol fraction of $[Li][Ntf_2]$, and reported analysis of the Li^+ cation environment and its transport mechanism.[7] This work showed that Li^+ cations are typically coordinated on average by about four oxygen atoms with each oxygen atom being contributed by different Ntf_2 anions. It was also found that Li^+ transport in this system is heavily dependent on Li^+ coordination and occurs primarily through Ntf_2 exchange (structure-diffusion mechanism) in the first coordination shell. The investigators claimed that only ~30% of the total diffusion of Li^+ cations results from their movement together with the coordination shell (vehicular mechanism).

MD simulations by Niu et al. showed that the stability of the Li^+ first coordination shell in [1-ethyl-2,3-dimethylimidazolium][PF_6]/[Li][PF_6] electrolyte is important for Li^+ transport.[8] Li^+ cations were observed to be strongly coordinated, on average, by six fluorine atoms from the PF_6^- anions. By changing its conformation, a PF_6^- anion can donate up to three fluorine atoms to coordinate with Li^+ cations. The number of anions around each Li^+ cation was found to be about four and increases slightly at higher [Li][PF_6] concentration. The first coordination shell of Li^+ cations in the investigated systems was found to be very stable and Li^+ was observed to diffuse together with its first coordination shell. A combined experimental and MD simulation study of [Li][Ntf_2] doped [1-buty-2-methylimidazolium(BMIM)][Ntf_2] indicated that Li^+ were coordinated by 5 oxygen atoms and there were on average three anions around each Li^+ in 0.24 [Li][Ntf_2]/0.66 [BMIM][Ntf_2][9] and 0.15 [Li][Ntf_2]/0.85 [BMIM][Ntf_2][10] electrolytes, with two in bidentate structure and one in monodentate structure. The investigators also noticed that as the lithium salt concentration increased to x=0.38 the average number of Ntf_2 anions around the Li^+ also increased due to the reason that there were more monodentate and less bidentate at higher lithium salt concentration.[9] In contrast, IR and DFT evidence from Lassègues lead to the conclusion that the number of Ntf_2 anions coordinating lithium in [Li][Ntf_2]/[EMIM][Ntf_2] and [Li][Ntf_2]/[BMIM][Ntf_2] electrolytes decreases with increasing salt concentration.[11] At lower salt concentrations these investigators claim bidentate coordination of Li^+ with two oxygen atoms from each anion, leading to $(Li^+(Ntf_2)_2)^-$ clusters. Simultaneous existing of two Li^+ solvation structures ($(Li^+(Ntf_2)_n)^{-(n-1)}$, n=3, 4) was also observed by Qian in a study of phase behavior of 0.67[Li][Ntf_2]/0.33[pyr_{1R}][Ntf_2] electrolytes (R = 4, 5).[12]

While the number of Li^+ charge carriers does increase with increasing lithium salt concentration, it is also observed that the electrolyte viscosity increases with increasing salt concentration,[8, 13 , 14] leading to reduced ion mobility and hence overall ionice conductivity in ionic liquid electrolytes (ILEs). However, it is the Li^+ contribution to ionic conductivity that is most important for battery applications. In this work, we have conducted MD simulations of $[pyr_{13}][Ntf_2]$/$[Li][Ntf_2]$ mixtures in order to investigate the influence of $[Li][Ntf_2]$ concentration on structural and transport properties. The molecular structure of the ionic liquid can be found in Figure 3-1 in Chapter 3. As we discussed above, this system has been studied previously by simulations and experiments, however, no detailed analysis and understanding of influence of lithium salt concentration on properties of this ILE has been reported. Hence, we focus on the Li^+ solvation structure and the influence of lithium salt concentration on both Li^+ solvation and the contribution of Li^+ to ionic conductivity in the electrolyte.

4.2. Molecular Dynamics Simulation Methodology

A version of the MD simulation code *Lucretius* that includes treatment of many-body polarization interactions was used for all MD simulations. The simulated three-dimensional, periodic cubic simulation cells consisted of 24 or 25 $[Li][Ntf_2]$ molecules and 48, 100, 132, 175 and 225 pyr_{13}/Ntf_2 ionic pairs, yielding ILEs with lithium salt mole fractions of 33%, 20%, 16%, 13% and 10 %, respectively. Also a pure (undoped) $[pyr_{13}][Ntf_2]$ RTIL has been investigated for comparison. The ILEs were initially created with box/cell size of ~ 57-107 Å. The dimensions of the simulation cells were then reduced to yield estimated densities at 423 K. All of the ILEs were simulated at both 423 K and 363 K (the pure ionic liquid and 15.8% systems were also run at 333 K and 298 K

to check the temperature dependence of electrolyte properties). All the systems were run in an NPT ensemble using integration scheme proposed by Martyna et al.[15] with frequencies of 10^{-2} and 0.5×10^{-3} fs for the thermostat and a barostat control, respectively. Production runs were more than 30 ns in length for each system. Starting configurations of the electrolytes at 363 K were taken from corresponding electrolytes at 423 K after more than 1.5ns NPT runs.

Bond lengths were constrained using the Shake algorithm[16] to utilize a larger time step. The long-range electrostatic forces, including forces between partial charges with partial charges and partial charges with induced dipoles, were treated by the Ewald summation method. The induced dipole-induced dipole interactions were tapered to zero at cutoff distance of 11.0 Å by a tapering function, with scaling starting at 9.5 Å. We also employed a multiple time step reversible reference system propagator algorithm.[15] Time step of 0.5 fs, 1.5 fs, and 3.0 fs for bonding, bending, and torsional motions, for nonbonded interactions within a 7.0 Å cutoff radius, and for nonbonded interactions between 7.0 and 11.0 Å and reciprocal space part of the Ewald summation were adopted in all the simulations, respectively.

4.3. Results and Discussion

4.3.1. Thermodynamic and Structure Properties

The densities of each system at 423 K and 363 K are given in Table 4-1 along with available experimental data. As can be seen, densities predicted from MD simulations are in reasonable agreement with available experimental values (at 353 K). The density of the ILE increases with increasing lithium salt concentration. For example, compared to the pure $[pyr_{13}][Ntf_2]$, density of the 0.33 $[Li][Ntf_2]$/0.67 $[pyr_{13}][Ntf_2]$ ILE obtained from MD

Table 4-1. Densities of investigated systems at 423K and 363K.

T (K)	(kg/m^3)					
	33%	**20%**	**16%**	**13%**	**10%**	**Pure IL**
423	1435	1387	1377	1366	1358	1323
363	1486	1437	1428	1415	1408	1347
353(exp [5])	1488	1436	1419 (15%)	/	1407	1369

simulations increased by 10.3% at 363 K and 8.46 % at 423 K. It is interesting to see that the density increase is temperature dependent, that is, the lower the temperature the more the density increases. The increased densities of the ILEs are mainly result from the very high density of [Li][Ntf_2] (2152 kg/m^3 at 20 ℃, Merck). This is due to the small size of the Li^+ cation and very strong Li^+/Ntf_2 interactions, which also influence the mixture density.

We began our analysis of the structural properties of the [Li][Ntf_2] doped RTIL by calculating ion-ion radial distribution functions (RDFs, g(r)). Shown in Figure 4-1 are RDFs of the center of mass of pyr_{13} cations, Ntf_2 anions, and the cross term in x [Li][Ntf_2]/(1-x) [pyr_{13}][Ntf_2] ILEs at 423 K. It is interesting to see that the typical strong cation-anion ($g^{+-}(r)$) correlation extends to a few nanometers in the pure ionic liquid, which corresponds to several anion diameters. Upon adding lithium salt into the IL, the intensity of the first peak of $g^{+-}(r)$ drops, indicating that the correlation between pyr_{13} cations and Ntf_2 anions were reduced due to strong Li^+-Ntf_2 interactions. Convincing evidence of the existence of strong Li^+/Ntf_2 interactions and their influence on IL structure can be seen in the dependence of $g^{--}(r)$ on salt concentration. With the addition

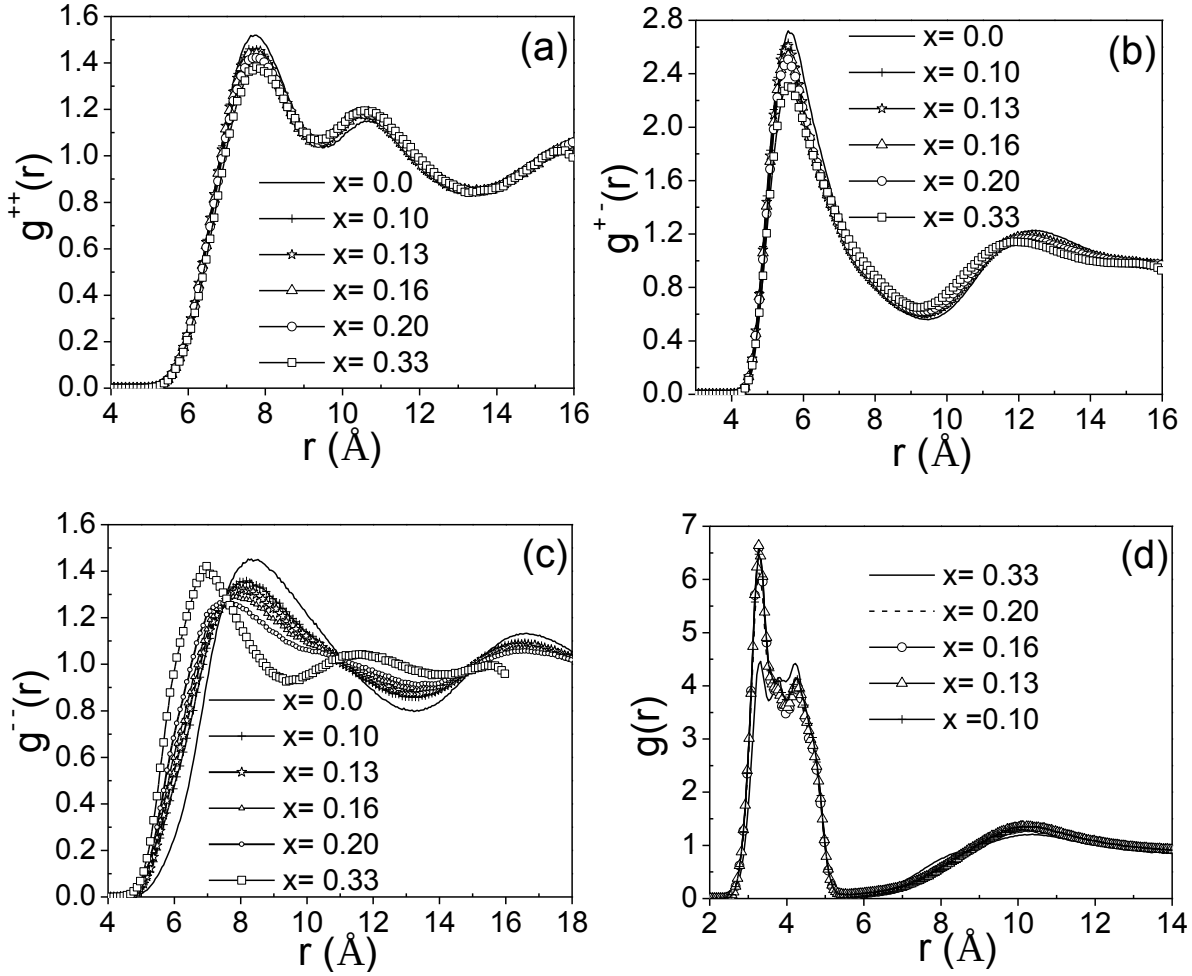

Figure 4-1. Molecular center-of-mass pyr_{13} - pyr_{13} (a), pyr_{13}- Ntf_2 (b), Ntf_2 - Ntf_2 (c), and Li^+ - Ntf_2 (d) radial distribution functions (RDFs) for x $[Li][Ntf_2]$/(1-x) $[pyr_{13}][Ntf_2]$ ILEs at 423K.

lithium salt, the first peak in the Ntf_2-Ntf_2 moves to shorter distances, indicating that the anions pack more tightly around Li^+ than in the pure RTIL. Second, the magnitude of the first peak in $g^{--}(r)$ decreases with increasing salt concentration except for the highest concentration investigated. In the 0.33 $[Li][Ntf_2]$/0.67 $[pyr_{13}][Ntf_2]$ electrolyte a dramatic increase in the magnitude of the first peak in $g_{--}(r)$ is seen, indicating a significant change in IL structure (see discussion below).

The RDF between the center of mass of Li^+ and Ntf_2 indicates that the coordination structure of Li^+ does not strongly depend on lithium salt concentration except at the highest concentration. The first peak in the Li^+-Ntf_2 RDF exhibits two maxima. The higher magnitude maximum (except at the highest concentration) occurs at a smaller separation and corresponds to Ntf_2 anions that contribute two oxygen atoms to the coordination of the Li^+ (bidentate configuration) as shown in Figure 4-2a. The maximum at the greater separation corresponds to Ntf_2 anions that contribute only a single oxygen atom to Li^+ coordination (monodentate configuration, see Figure 4-2b). At the highest salt concentration, there is a dramatic decrease in the magnitude of the first maximum, indicating a significant decrease in the amount of bidentate coordination of the Li^+ cations.

The end of the first peak in the Li^+-Ntf_2 RDF occurs at a separation of about 5.6 Å. We consider the coordination number of Ntf_2 around each Li^+ to correspond to the number of anions whose center-of-mass lies within this distance of the Li^+, as shown in Figure 4-3. For concentrations below x = 0.33 the number of anions coordinating each Li^+ is around 3.3 and independent of salt concentration. Interestingly, the number of anions coordinating each Li^+ increases at the highest salt concentration (x = 0.33), to

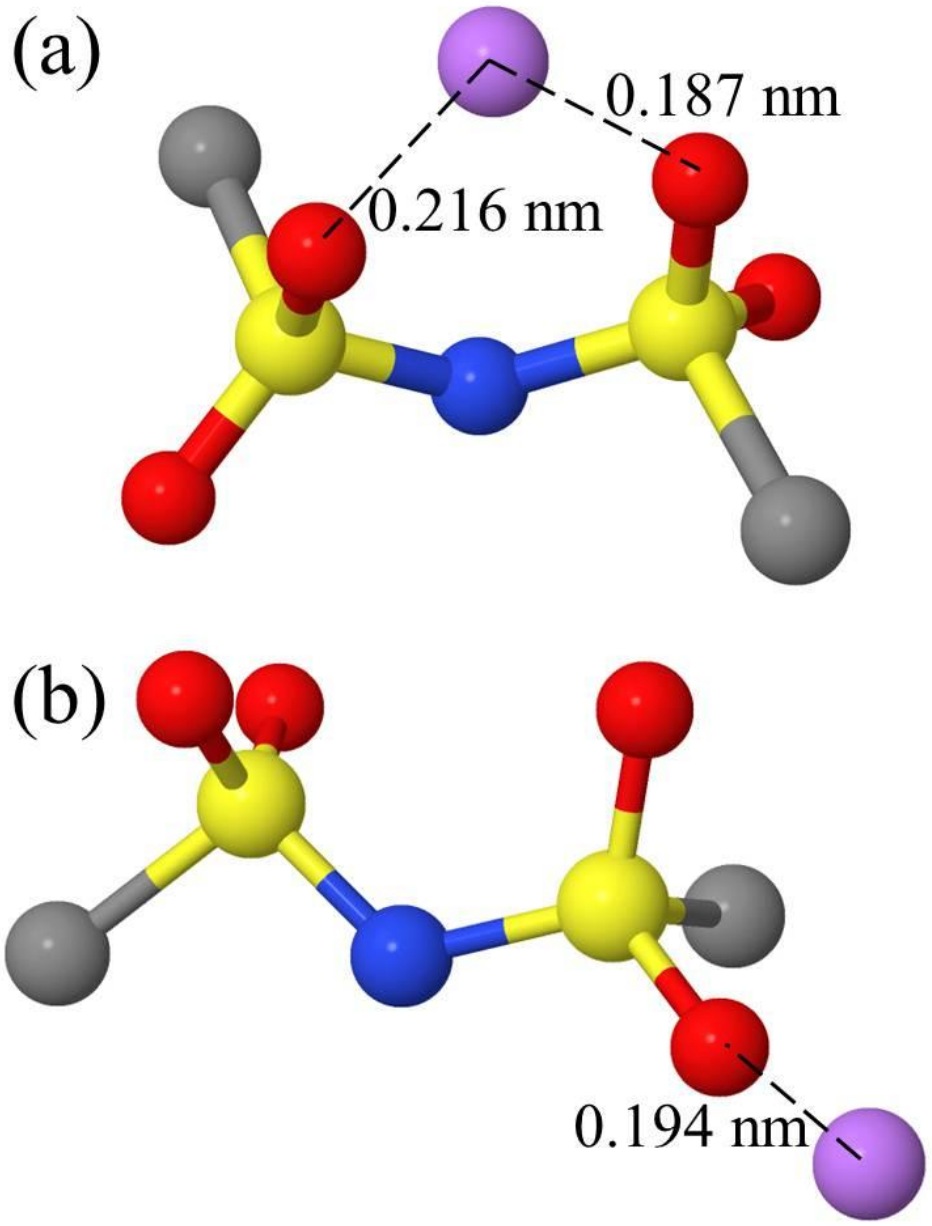

Figure 4-2. Bidentate (a) and monodentate (b) configurations of Ntf_2 anions coordinating to a Li^+.

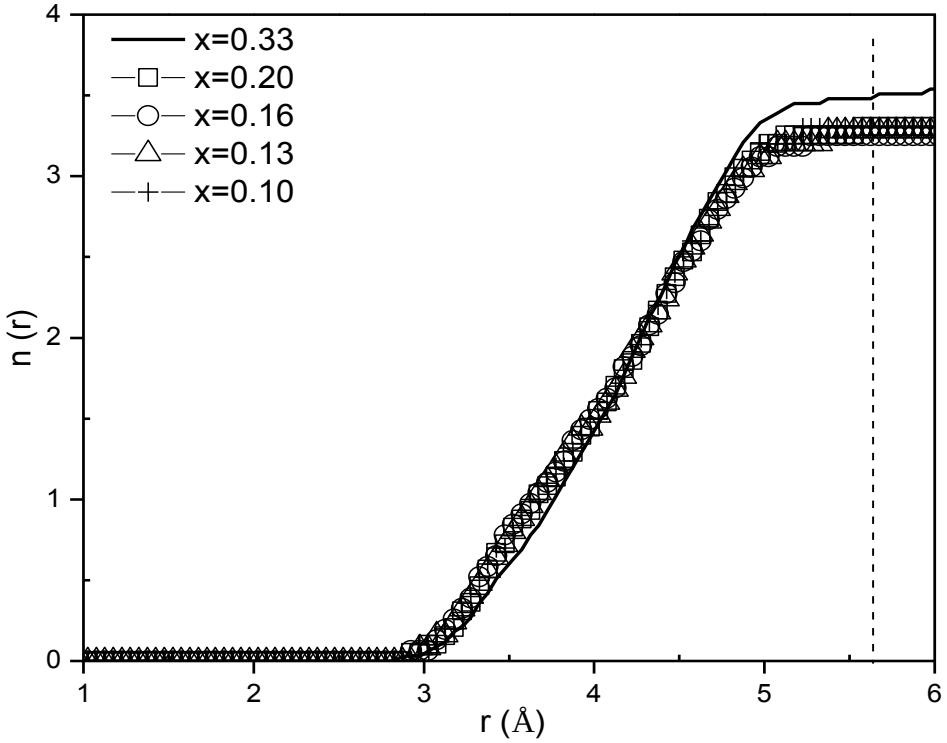

Figure 4-3. Number of Ntf_2 anions coordinating with a Li^+ cation within distance r.

around 3.5, despite the decrease in the ratio of Ntf_2 to Li^+.

In order to better understand how Li^+ is coordinated in the ILE, we also calculated the $Li^+ – O^{Ntf2}$ and $Li^+ – N^{Ntf2}$ RDFs as shown in Figure 4-4. For all the simulated electrolyte compositions, the Li^+ cation is most closely approached by the O^{Ntf2} atoms with the position of the $Li^+ – O^{Ntf2}$ first peak at 1.97 Å. The magnitude of $Li^+ – O^{Ntf2}$ RDFs first peak slightly decreases with increasing lithium salt concentration. Defining the $Li^+ – O^{Ntf2}$ first coordination shell by an $r(Li^+ – O^{Ntf2}) < 2.8$ Å, we find that, for all the electrolytes, the Li^+ cation was on average coordinated by 4.1 O^{Ntf2} atoms as shown in Figure 4-5. Similar behavior is seen at 363 K which is in agreement with experimental observation that temperature dependence of ionic pair population is negligible.[9] The $Li^+ – N^{Ntf2}$ RDF shows a first peak with two maxima analogous to the behavior observed for the Li^+-Ntf_2 RDF (Figure 4-1d), again supporting the simultaneous existence of monodentate and bidentate coordination of Li^+ by the anions. This behavior, along with an increase in the number of anions coordinating each Li^+, was observed in experimental and MD simulations[9,10] of $[Li][Ntf_2]$/$[bmim][Ntf_2]$ discussed above. The investigators concluded that at least two kinds of coordination of Li^+ by Ntf_2 are existing simultaneously, i.e., closer approaching bidentate and further separated monodentate anions. The interesting thing here is that the first maximum in the first Li^+-Ntf_2 coordination peak is much higher than the second one in their systems, indicating a greater preference for bidentate anions within the Li^+ first coordination shell than observed in our simulations. This difference suggests that the Li^+ cations in our ILEs are coordinated by less bidentate and more monodentate Ntf_2 anions.

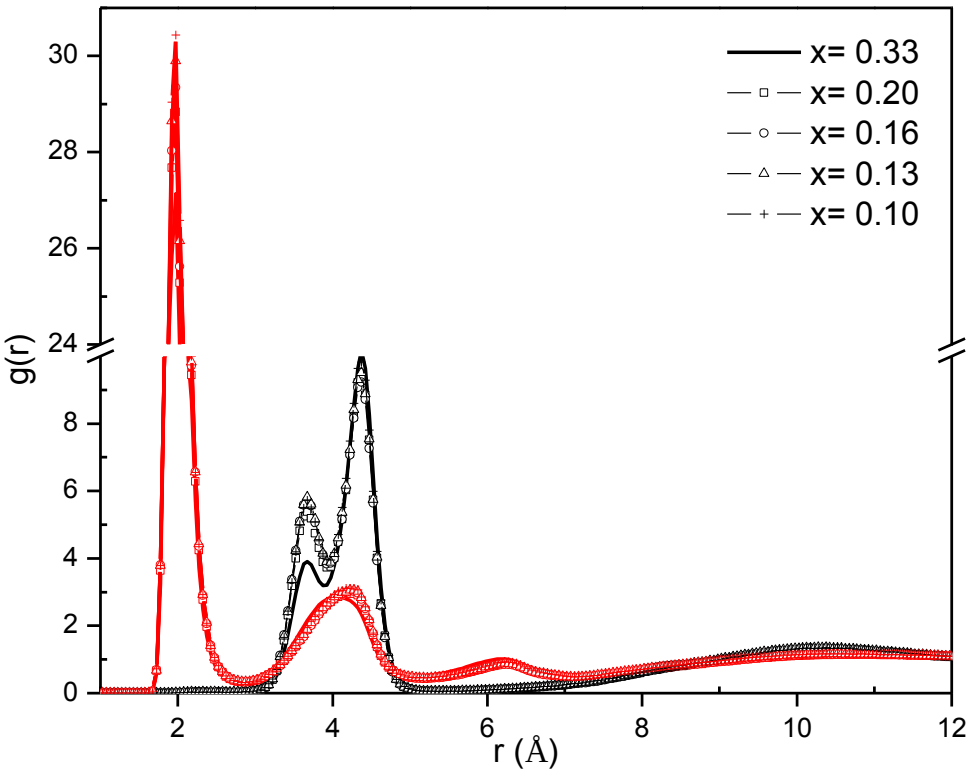

Figure 4-4. $Li^+ – O^{Ntf2}$ (red), $Li^+ – N^{Ntf2}$ (black) radial distribution functions at 423K.

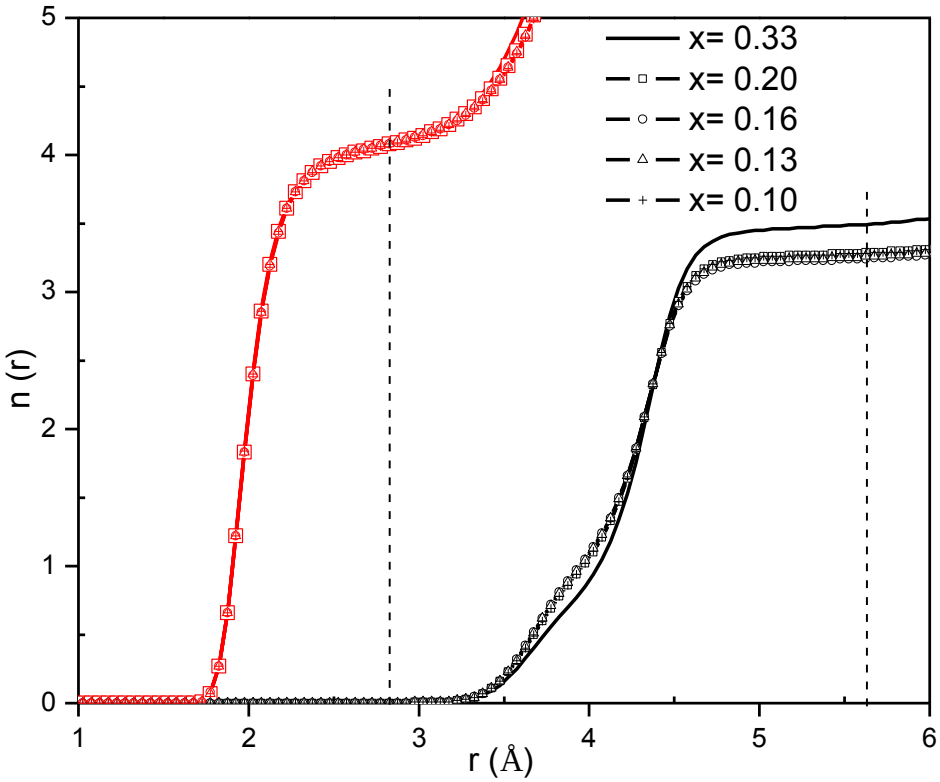

Figure 4-5. Number of O^{Ntf2} (red) and N^{Ntf2} (black) coordinating to a Li^+ cation within distance r.

Examination of the running $Li^+ - N^{Ntf2}$ coordination numbers, shown in Figure 4-5, shows 1.1 anions within 4 Å (primarily bidendate)[17] of each Li^+ and 2.2 anions between 4 Å and 5.6 Å (monodentate) for x $[Li][Ntf_2]$ – (1-x) $[pyr_{13}][Ntf_2]$ systems ($x \leq 0.20$), respectively. This structural pattern captured from a snapshot of the systems is illustrated in Figure 4-6a. It is interesting that the first maxima in the first peak of the $Li^+ - N^{Ntf2}$ RDFs drops while the maxima increases when more lithium salt in the electrolyte (x = 0.33), analogous to the behavior observed in the $Li^+ - Ntf_2$ RDFs. An examination of number of the N^{Ntf2} around the Li^+ cations in 0.33 $[Li][Ntf_2]$ – 0.67 $[pyr_{13}][Ntf_2]$ electrolyte, shown in Figure 4-5, indicates that the Li^+ in average is surrounded by 0.9 N^{Ntf2} within 4 Å and 2.6 N^{Ntf2} between 4 Å and 5.6 Å for a total of 3.5. This behavior indicates that at the highest Li^+ concentration, a large fraction of the bidentate anions transformed to monodentate while the a fourth monodentate anion penetrated the coordination shell , keeping the Li^+-O^{Ntf2} coordination number constant at around 4.1 (see Figure 4-5). A typical coordination of Li^+ for the x = 0.33 electrolyte is shown in Figure 4-6b.

The above findings confirm that at all lithium salt concentrations some Li^+ cations are coordinated by three anions with two in monodentate structure and one in bidentate structure, and other Li^+ cations are coordinated by four monodentate anions, with the fraction of bidentate coordination decreasing at the highest salt concentration investigated. This finding is in agreement with the experimental investigation.[12] The investigators found that when Li^+ cations are coordinated by 4 monodentate Ntf_2 anions each of them provides only one oxygen atom. However, different from our observation, they claimed that when a Li^+ cation is coordinated by 3 anions, there are two in bidentate

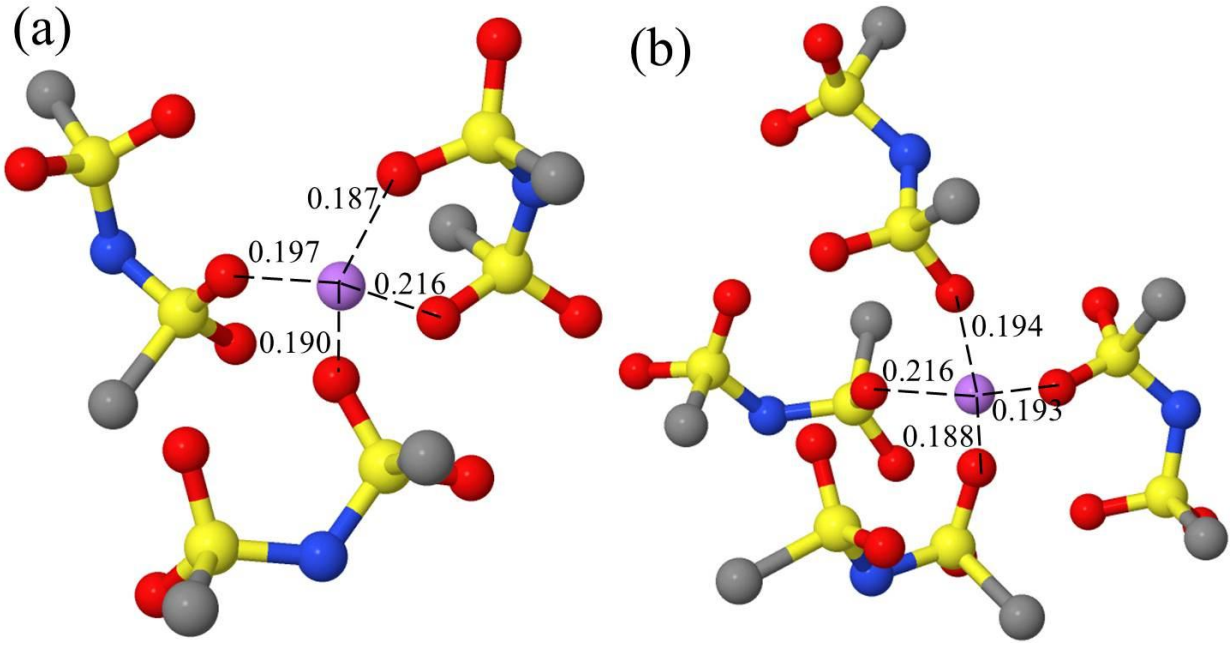

Figure 4-6. Two Li^+ cation solvation structures (distance is in nm). Fluorine atoms of the Ntf_2 anions are not shown for clarity.

structure and one in monodentate structure, resulting in a five-coordinate Li^+ cation.

4.3.2. Transport Properties of [Li][Ntf_2] doped Ionic Liquid Electrolytes

The self-diffusion coefficients from the MD simulation are plotted versus temperature in Figure 4-7 and are compared with experimental diffusion coefficients from pfg-NMR measurements.[5,18] Uncertainty of the reported self-diffusion coefficients is less than 10%. As can be seen from Figure 8a, the calculated self-diffusion coefficients of ions in the neat ionic liquid are in good agreement with the experimental data. The ion self-diffusion coefficients in the mixtures are also compared with the available experimental data in Figure 4-8b-e. At temperature below 333 K, the ion self- diffusion coefficients obtained from NMR experiments follow the order: pyr_{13} > Ntf_2 > Li^+. At higher temperature, however, the NMR measurements exhibit an unexpected increase of self-diffusion

Figure 4-7. Ion self-diffusion coefficients of ILEs obtained from MD simulations and pfg-NMR measurements (solid line: ref. 5, dot line: ref.21) at different lithium salt doping level: a) x=0; b)

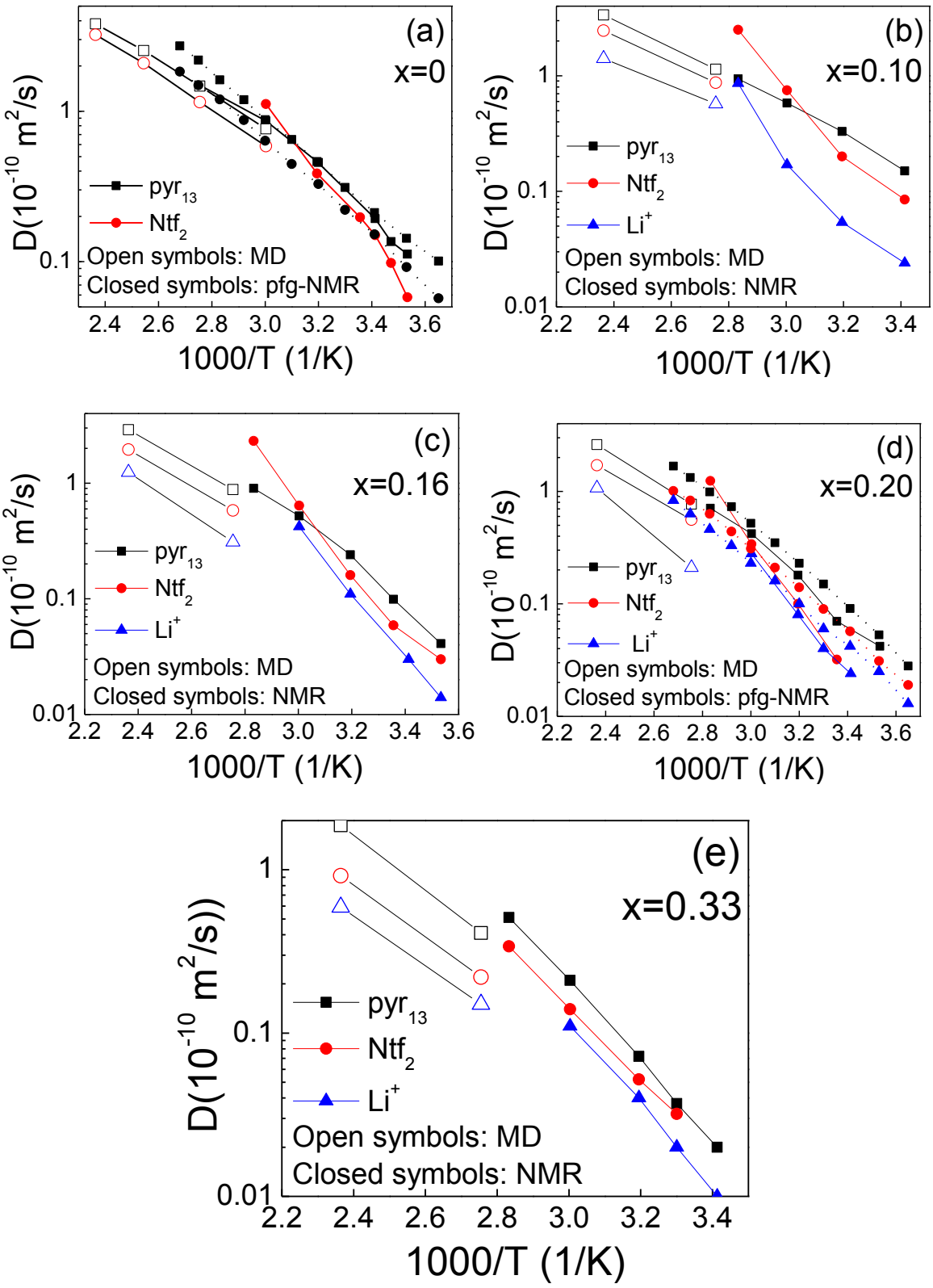
(a)
x=0
pyr13
Ntf2
Open symbols: MD
Closed symbols: pfg-NMR
D(10-10 m2/s)
1000/T (1/K)
(b)
x=0.10
pyr13
Ntf2
Li+
Open symbols: MD
Closed symbols: NMR
D(10-10 m2/s)
1000/T (1/K)
(c)
x=0.16
pyr13
Ntf2
Li+
Open symbols: MD
Closed symbols: NMR
D(10-10 m2/s)
1000/T (1/K)
(d)
x=0.20
pyr13
Ntf2
Li+
Open symbols: MD
Closed symbols: pfg-NMR
D(10-10 m2/s)
1000/T (1/K)
(e)
x=0.33
pyr13
Ntf2
Li+
Open symbols: MD
Closed symbols: NMR
D(10-10 m2/s))
1000/T (1/K)

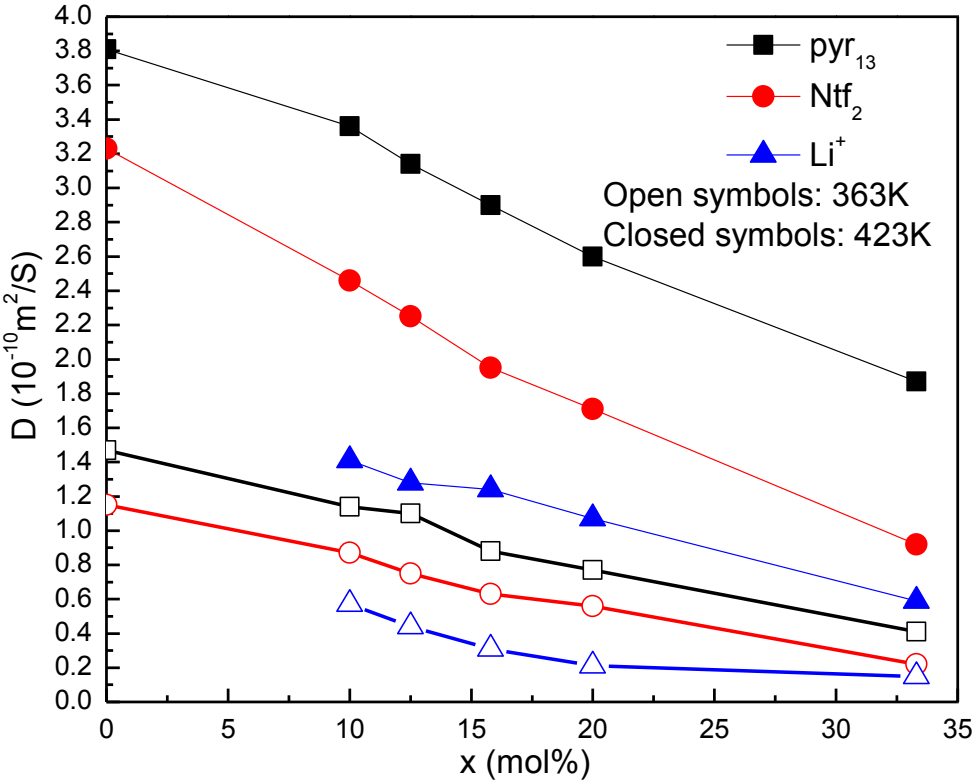

Figure 4-8. Ion self-diffusion coefficients as a function of [Li][Ntf_2] doping content at 423 K and 363 K.

coefficients for the Ntf_2 anion and Li^+ cation. Such an increase observed in the NMR experiment is very suspicious because it was not observed in other measurements of $[pyr_{13}][Ntf_2]$ and its mixtures with $[Li][Ntf_2]$,[14] and a very similar $[pyr_{14}][Ntf_2]$,[19] either in our previous MD simulation of pure[20] and lithium salt doped[7] $[pyr_{13}][Ntf_2]$ RTIL. Furthermore, the experimentally measured diffusion coefficients for Li^+ and the anion exhibit anomalous temperature dependence corresponding to a decreasing apparent activation energy with decreasing temperature. The MD derived self-diffusion coefficient for pyr_{13} cation is in reasonable agreement with experiment for all concentrations.

In Figure 4-8 we examine the concentration dependence of ion self-diffusion coefficients. As expected, the pyr_{13} cations diffuse the fastest followed by the Ntf_2 anions with the Li^+ cations having the lowest self-diffusion coefficient. Upon adding lithium salt into the RTIL, remarkable slowing down of the ionic mobility is noticed. The addition of $[Li][Ntf_2]$ to the $[pyr_{13}][Ntf_2]$ RTIL retarded the Ntf_2 anions diffusivity more significantly than pyr_{13} cations, which is consistent with the fact that Ntf_2 is coordinated with the slow-moving Li^+ (see discussion below). We believe the slowing down of pyr_{13} cations with increasing salt concentration is mainly due to increasing viscosity in the mixtures.

The degree of uncorrelated motion from MD simulations at 423 K are shown in Figure 4-9. The average values from 0.2 to 0.6 ns for $\alpha(t)$ from Figure 4-9 are taken as α with estimated uncertainties of ± 0.1. MD simulations predict α lies in the narrow range of 0.63 - 0.69 at 423 K. A slightly higher α (by about 0.05) was obtained for the ILEs at 363 K. α predicted from MD simulation is higher than those available experimental results.[5] Experiment measurements of α by Nicotera for x $[Li][Ntf_2]$/(1-x) $[pyr_{13}][Ntf_2]$ electrolyte

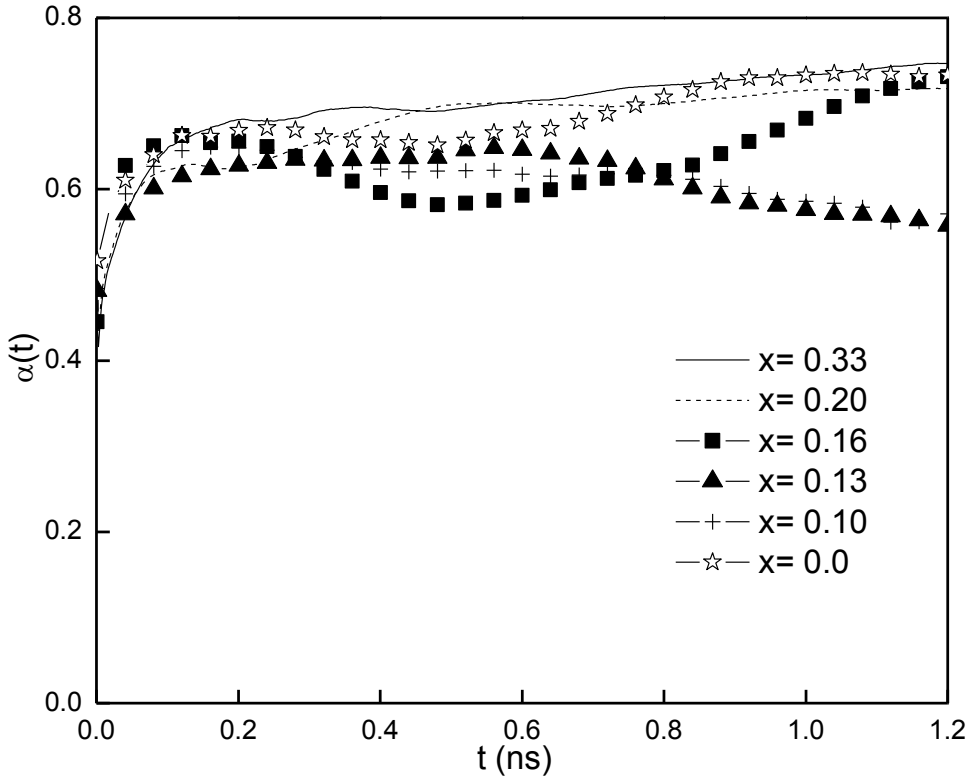

Figure 4-9. Degree of ion uncorrelated notion α for simulated electrolytes at 423K.

(Figure 4-10) shows strong temperature and concentration dependence. The results are, however, suspicious due to the poor results of ion diffusion coefficients from the experiment. Another systematic investigations of α for pure [pyr13][Ntf2] RTIL and 0.65 M [Li][Ntf2] /[pyr13][Ntf2] between 270 and 380 K range from 0.45 to 0.61 with the maximum at 303K.21. However, the huge size of error bars in the experiments makes any comparison of α from experiment with MD simulation results impossible. Nevertheless, we notice that difference between α for the pure RTIL and lithium salt doped RTIL becomes negligible at high temperature range. This finding agrees well with our prediction from MD simulations at 363 and 423 K, that is, α for the pure RTIL is close to that for lithium salt doped RTIL. As the temperature increases, we might expect α to increase due to the relative weaker ion electrostatic interactions (compared to thermal energy). This expectation, however, is not well supported by the available experiments or our by our MD simulations. Finally, our simulations show that the degree of ion uncorrelated motion increase slightly as the concentration of lithium salt increases, but the effect is weak.

Ionic conductivities of simulated ILEs are shown in Figure 4-11 as a function of concentration and are compared with experiments as well.[5,21] Conductivity extracted from simulation for pure [pyr_{13}][Ntf_2] is in excellent agreement with available experimental values. We were unable to extract an accurate estimate of conductivity at temperature below 333 K for the 16% ILE but extrapolation from the 333 K indicates very good agreement with experiment.[14] The conductivity for the 20 mol % salt ILE (0.70 M [Li][Ntf_2]) at 423 K from simulation is 26 mS/cm, which is also in good agreement with an experimental estimate of 26.2 mS/cm (0.65 M [Li][Ntf_2] at 423 K calculated from

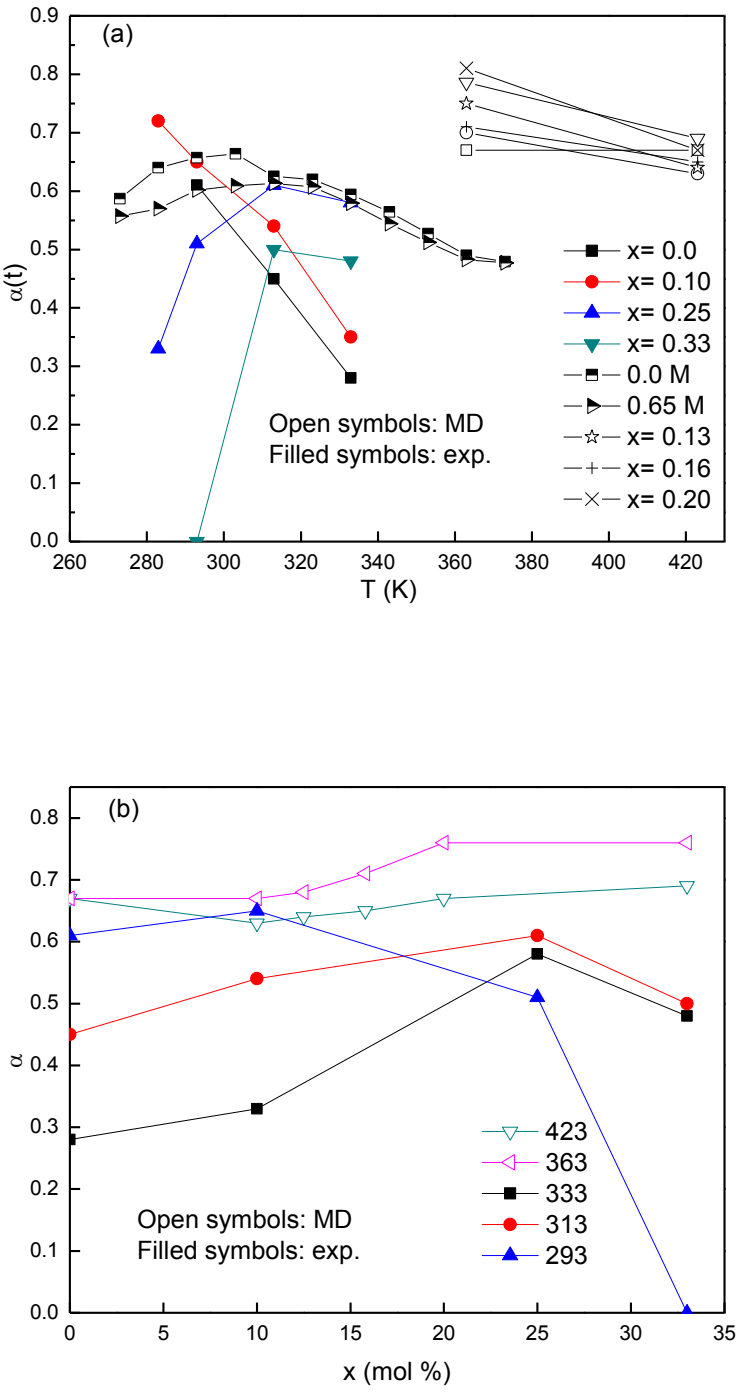

Figure 4-10. Degree of ion uncorrelated motion from MD simulation and available experiments as a function of temperature (a) and [Li][Ntf_2] doping content (b) for the pure RTIL and [Li][Ntf_2] doped IL.

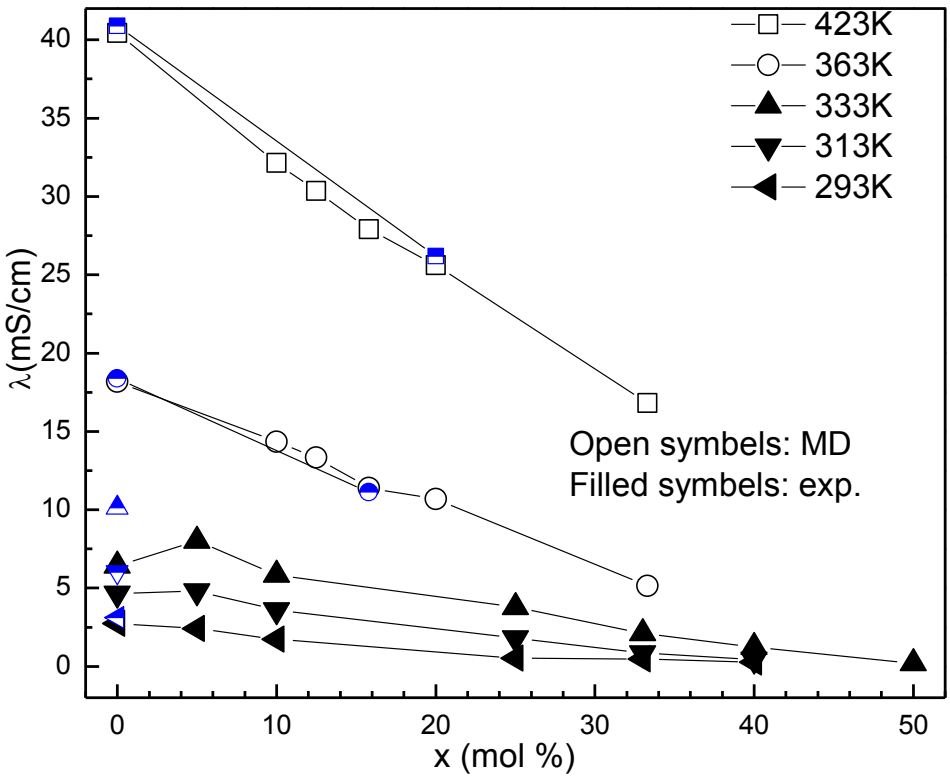

Figure 4-11. Ionic conductivity obtained from MD simulations as a function of [Li][Ntf_2] doping content at 423 K and 363 K with available experimental data at 333 K, 313 K, and 293 K(Filled: ref.5, Half-filled: ref.21). Uncertainty of the reported ionic conductivity is less than 11%.

the fitted VTF equation in the experimental paper).[21] MD simulation predicted that the conductivity of 16 mol % salt ILE (0.58 M [Li][Ntf_2]) at 363 K is 11 mS/cm, compared to 11.1 mS/cm from experiment at 363 K (0.65 M [Li][Ntf_2]).[21] As expected, the ionic conductivity of the RTIL was dramatically lowered by the addition of [Li][Ntf_2] and continued decreasing with increasing concentration of [Li][Ntf_2]. More interesting is the higher the temperature the more conductivity drops when lithium salt is added, that is, the influence of lithium salt on the ionic conductivity is also temperature dependent. This behavior was also observed in an experimental investigation of [pyr_{13}][FSI]/[Li^+][FSI] and [1,2-Dimethyl-3-propylimidazolim(DMPIm)]/[Ntf_2][Li^+][Ntf_2].[22,23] This is because of the observed stronger concentration dependence of ion self-diffusion coefficient, particularly pyr_{13} cations and Ntf_2 anions, at higher temperature (Figure 4-8).

Figure 4-12 shows the temperature dependence of the conductivity from MD simulations and available experiments. The ionic conductivity of a solution is directly related to the number, charge and mobility of the carrier ions as well as the degree of correlation in ionic motion. A decrease in temperature and an increase in litium salt concentration both result in decreased ionic conductivity due to increased viscosity of the solution resulting in reduced ion mobility. The temperature dependence of the ionic conductivity corresponds to an expected increase in apparent activation energy with decreasing temperature observed in the conductivity of many neat ionic liquids that corresponds to an underlying glass transition at lower temperatures.

Due to the importance of Li^+ transport on the efficacy of ILEs in lithium battery applications, we examined the influence of lithium salt concentration on the Li^+ cation transport mechanism. It is generally recognized that Li^+ cation transportation has

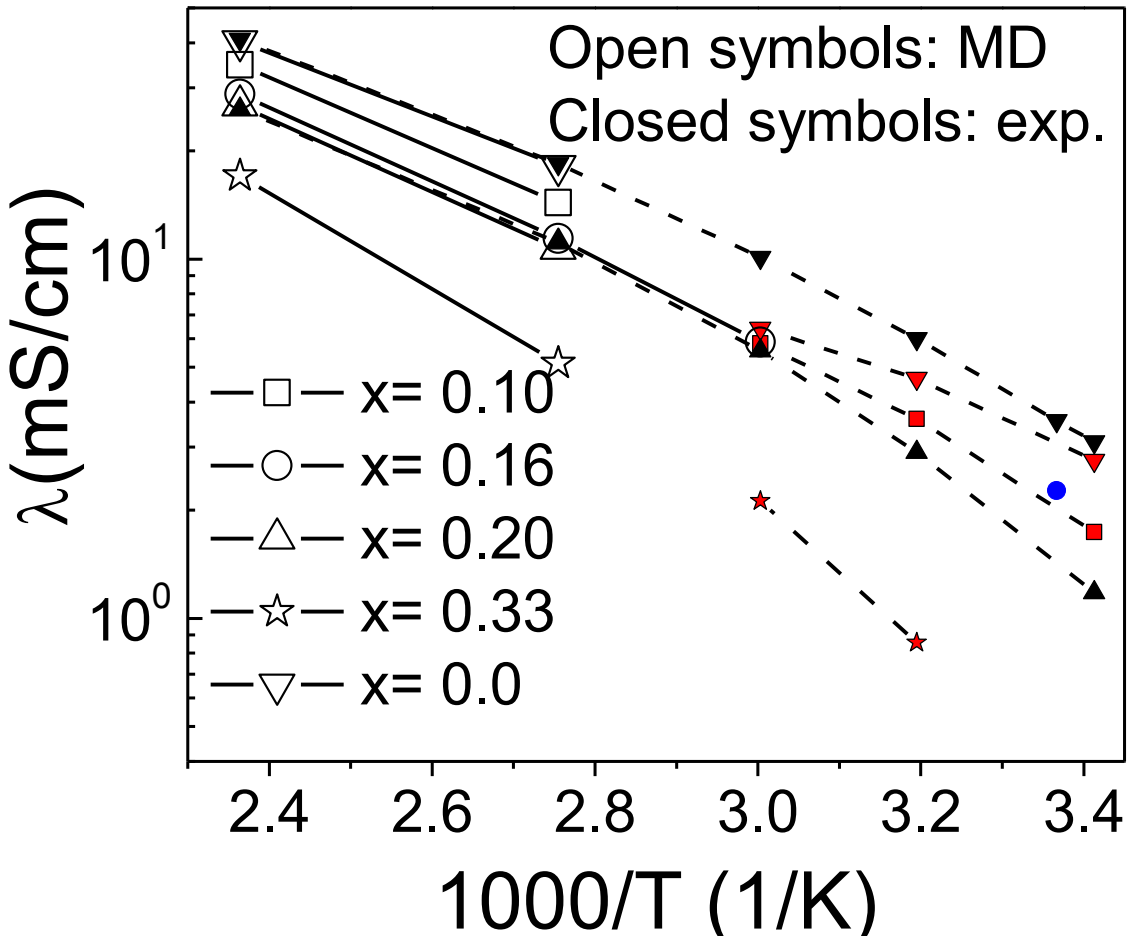

Figure 4-12. Ionic conductivity obtained from MD simulations for different ILEs as a function of temperature with available experimental data (red: ref.5, black: ref., blue: ref.14).

contributions from motion with their coordination shell (of solvating anions) (vehicular mechanism) and contributions from exchanging Ntf_2 anions in the first coordination shell (structure diffusion mechanism) of the Li^+ cation. In order to better understand the relative importance of these mechanisms and the dependence of Li^+ transport on salt concentration we monitored Li^+-N^{Ntf2} residence times as a function of Li salt concentration. The residence time ACF was calculated using

$$p_{Li^+-N^{Ntf_2}} = \frac{<H_{ij}(t)H_{ij}(0)>}{<H_{ij}(0)H_{ij}(0)>} \qquad (4\text{-}5)$$

where $H_{ij}(t)$ = 1 when $r_{Li^+-N^{Ntf_2}}$ < 5.3 Å, respectively, and zero otherwise. The ensemble average denoted by < > is taken over all Li^+ cations in the system at multiple time origins. This autocorrelation function decays from unity to zero when all Li^+ cations have completely exchanged their solvation shell of Ntf_2 anions. It was found that the ACF could be reasonable well fit with a function of the form

$$p_{Li^+-N^{Ntf_2}} = Aexp\left[-(t/\tau_{KWW})^{\beta}\right] \qquad (4\text{-}6)$$

as shown in Figure 4-13. Figure 4-13 shows relatively rapid decay of the ACF. The decay of the ACF to zero occurs on a very short time may indicate Li^+-Ntf_2 correlations are very rarely long-lived. This is in contrast to the report that long-lived negative $Li^+(NTF2)_3^{2-}$ complexes move as an entity in ILE, and hence, it retards the diffusion of Li^+ to the anode at low potential gradient.[6] Given the result that β obtained from the fits is around 0.9, we believe the Li-Ntf_2 ACFs decay with almost single relaxation time behavior. We estimated the lifetime (τ) of the solvation shell, i.e., the time needed for a Li^+ to completely exchange solvating anions, as

$$\tau = \int_0^{\infty} exp\left[-(t/\tau_{KWW})^{\beta}\right] dt \qquad (4\text{-}7)$$

In Table 4-2 we give τ and the corresponding Li^+ MSD at τ for each temperature and salt

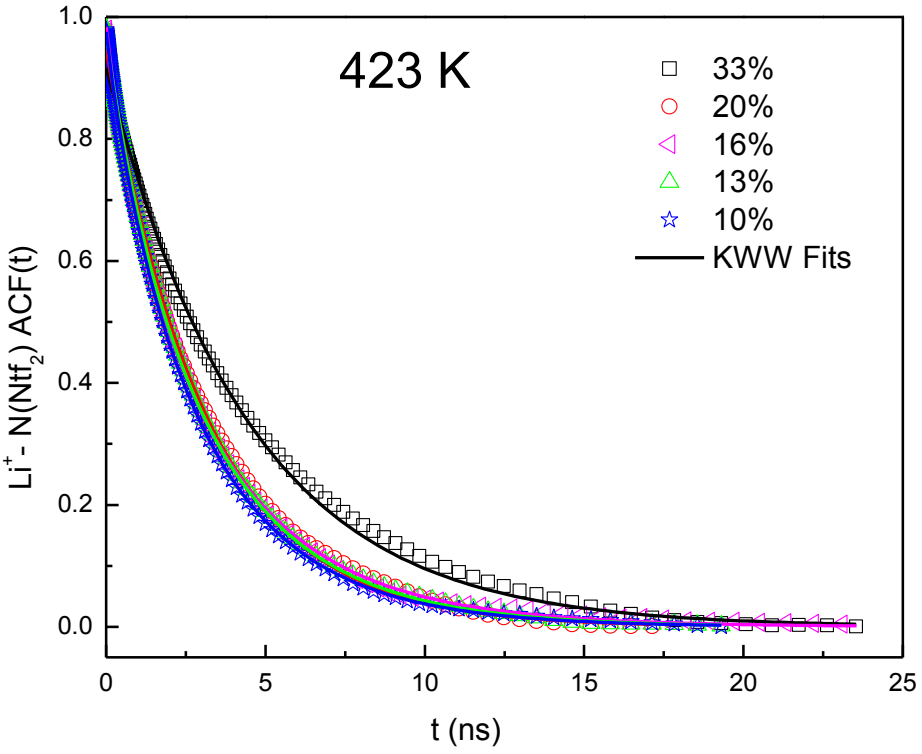

Figure 4-13. Li^{+}- N ^{Ntf2} Auto Correlation Functions (ACFs) and fits at 423 K.

Table 4-2. $Li^+ - N^{NTf2}$ residence time (τ) and Mean-square Displacement (MSD) of Li^+ at τ

	10%		13%		16%		20%		33%	
T (K)	**423**	**363**	**423**	**363**	**423**	**363**	**423**	**363**	**423**	**363**
τ (ns)	2.80	8.73	2.96	10.47	3.14	16.69	2.97	17.25	4.07	20.50
Li^+ MSD (τ) ($Å^2$)	244.4	209.4	229.5	266.3	237.0	321.9	208.7	283.3	160.2	182.8

concentration investigated. As expected, when the amount of lithium salt increases, τ also increases, implying a reduced exchange rate of anions in first coordination shell of Li^+ and hence reduced structure diffusion. The coordination shell lifetime τ also increases with decreasing temperature. However, an increase in the coordination shell lifetime cannot necessarily indicate an increase in the importance of the vehicular diffusion mechanism to Li^+ transport. Examination of the Li^+ MSD at τ, which indicates how far on average Li^+ diffuses before completely exchanging its coordination shell, shows very little concentration dependence for $x \leq 0.2$. For both temperatures, MSD at τ is around 250 $Å^2$, yielding a mean Li^+ displacement of around 16 Å before the coordination shell (of between three and four Ntf_2 anions) is renewed. Hence, Li^+ exchanges coordinating anions on a scale comparable to the size of the anions, indicating that vehicular motion plays some role in Li^+ cation diffusion. It is clear therefore both structural diffusion and vehicular diffusion contribute to Li^+ motion and that vehicular motion (i.e., motion of long-lived $Li^+(Ntf_2)_n^{-(n-1)}$ with n = 3 or 4) does not dominate Li^+ motion. Although we see increasing importance of vehicular motion with decreasing Li^+ concentration and temperature, it is still not dominant, and we see little sign of large-scale motion of Li with

the same coordinating Ntf_2 anion. At the highest salt concentration, Li^+ MSD at τ actually decreases to around 180 $Å^2$, or a length scale of around 13 Å, indicating a decrease in importance of the vehicular mechanism. We note that in a previous MD simulation study of this system (with X = 0.25) it was reported that vehicular mechanism contributes only 30 % of the total diffusion of the Li^+ cations.[7]

High ionic conductivity of ILEs does not necessarily reflect their ability to conduct Li^+. The conductivity due to Li^+ cation transport, denoted as λ^{Li+}, can be approximated using

$$\lambda^{Li^+} = \frac{n_{Li^+} D_{Li^+}}{n_{Li^+} D_{Li^+} + n_{pyr_{13}} D_{pyr_{13}} + n_{Ntf_2} D_{Ntf_2}} \lambda \qquad (4\text{-}8)$$

where n_i is the number of atoms of type i. This equation is valid where no ion correlations are present, but it is justifiable to use it here to obtain a rough estimate of λ^{Li+} for ILEs because the degree of ion uncorrelated motion is rather high (> 0.60) for ILEs in this study.

Shown in Figure 4-14 is the concentration dependence of conductivity due to Li^+ cation transport from simulations at 423 K and 363 K. As the concentration of [Li][Ntf_2] increasing, λ^{Li+} is expected to increase proportionally since the number of Li^+ increases in the ILE. A saturation of the conductivity due to Li^+ transport, however, is observed within the investigated concentration range at both simulation temperatures. This saturation can be attributed to the increased viscosity of the solutions. We estimated λ^{Li+} of all systems at 298 K based on the data at 423 K and 363 K. This was done by first extrapolating the ion self-diffusion coefficients at 298 K assuming Arrhenius temperature dependence and then calculating the overall ionic conductivity. α used in the extrapolation is the same as the corresponding one (for each composition) at 363 K.

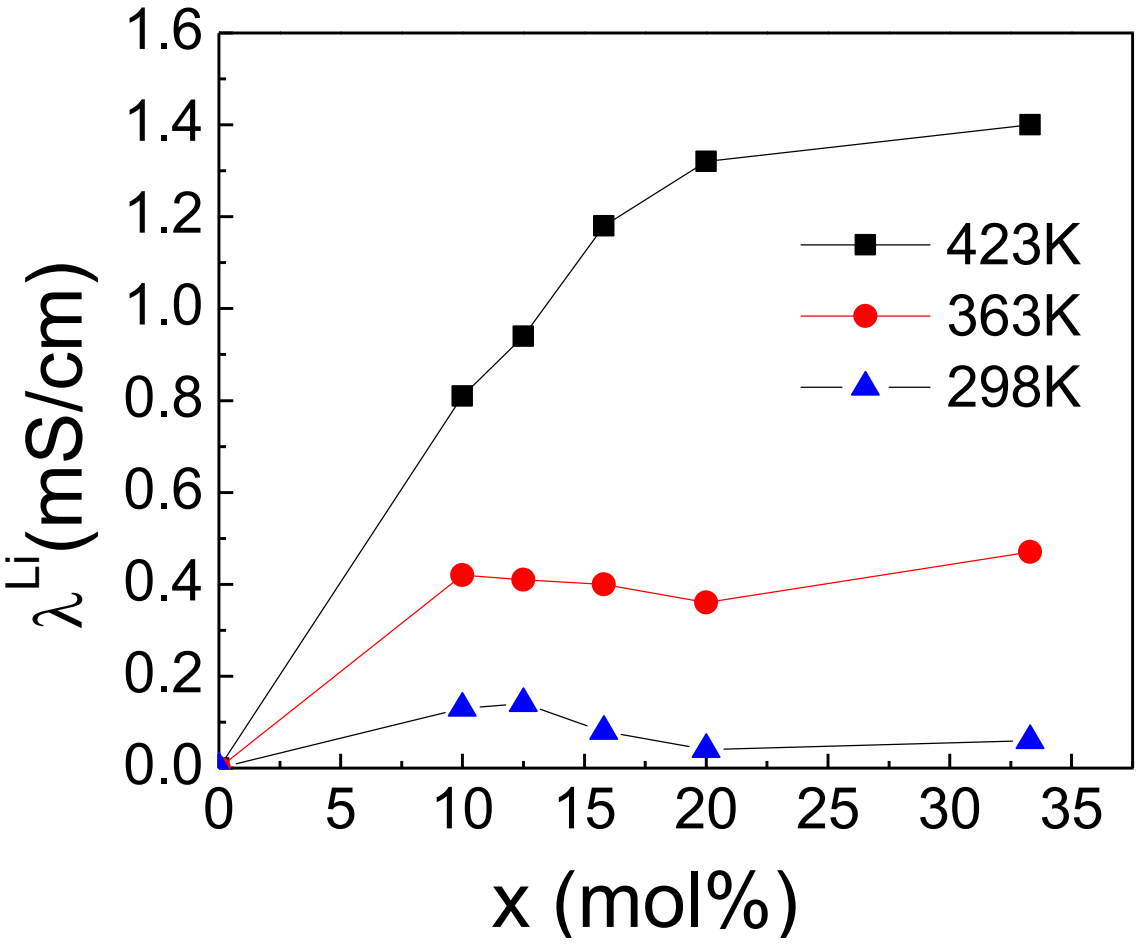

Figure 4-14. Li^+ contribution to the ionic conductivity of ILEs as a function of [Li][Ntf_2] doping content.

Interestingly, the estimated Li^+ conductivity at 298 K exhibits a maximum at the doping level ~ 13 mol%. Based upon our results at 423 K and 363 K, when same amount of lithium salt is added into the ionic liquid, the increase of viscosity is greater at the lower temperature, resulting in the observed maximum in Li^+ conductivity at even lower temperature (298 K).

4.4. Conclusions

MD simulations were performed on five ILEs consisting of $[pyr_{13}][Ntf_2]$ RTIL and $[Li][Ntf_2]$ salt at various concentrations. Structure of the $(Li^+(Ntf_2)_n)^{(n-1)-}$ cluster was identified by analyzing center of mass and atom-atom RDFs. The Li^+ cations are on average coordinated by 4.1 oxygen atoms at all lithium salt doping level. The closed two peaks of the Li^+–N^{Ntf2} RDF indicates that at least two kinds of solvated Ntf_2 exist in the simulated systems. Number of anions within the first coordination shell of Li^+ cations is found to be either 3 or 4. The fraction of the later solvation structure, however, increases when lithium salt concentration goes up. When coordinated by three anions, there are two in monodentate structure and the other in bidentate structure. However, all anions are in monodentate structure when a Li^+ cation is surrounded by four anions. Density, ionic conductivity, and self-diffusion coefficients derived from MD simulations with the many-body polarizable force field are in good agreement with the available experimental data and reveal that the $[Li][Ntf_2]$ doped ionic liquid electrolytes have unusual dynamics that depends on the $[Li][Ntf_2]$ doping level. A significant but unfortunate decrease in transport properties of all the ions in the systems are noticed upon the addition of lithium salt to the ionic liquid electrolytes. This is directly correlated to the increased viscosity and formation of $(Li^+(Ntf_2)_n)^{(n-1)-}$ clusters in the mixtures. $(Li^+(Ntf_2)_n)^{(n-1)-}$ can be long-lived

but the fraction of such long-lived complexes is very small and should not dominate the diffusion of Li^+ cations.

4.5. References

(1) Lewandowski, A.; Świderska-Mocek, A. *J. Power Sources* **2009**, 194, 601.

(2) Armand, M.; Endres, F.; MacFarlane, D. R.; Ohno, H.; Scrosati, B. *Nature Materials* **2009**, 8, 621.

(3) Howlett, P. C.; MacFarlane., D. R.; Hollenkamp, A. F. Electrochem. *Solid-State Lett.* **2004**, 7(5), A97.

(4) Henderson, W. A; Passerini, S. *Chem. Mater.* **2004**, 16,, 2881.

(5) Nicotera, I.; Oliviero, C.; Henderson, W. A.; Appetecchi, G. B.; Passerini, S. *J. Phys. Chem. B* **2005**, 109, 22814.

(6) Saito, Y.; Umecky, T.; Niwa, J.; Sakai, T.; Maeda, S. *J. Phys. Chem. B* **2007**, 111, 11794.

(7) Borodin, O.; Smith, G. D.' Henderson, W. *J. Phys. Chem. B* **2006,** *110,* 16879**.**

(8) Niu, S.; Cao, Z.; Li, S.; Yan, T. *J. Phys. Chem. B* **2010**, 114, 877.

(9) Monteiro, M. J.; Bazito, F. F. C.; Aiqueira, L. J. A.; Ribiro, M. C. C.; Torresi, R. M. *J. Phys, Chem. B* **2008**, 112, 2102.

(10) Umebayashi, Y.; Hamano, H.; Seki, S.; Minofar, B.; Fujii, K.; Hayamizu, K.; Tsuzuki, S.; Kameda, Y.; Kohara, S.; Watanabe, M. *J. Phys. Chem. B* **2011**, 115, 12179.

(11) Lassegues, J.; Grondin, J. Aupetit, C.; Johansson, P. *J. Phys. Chem. A* **2009**, 113, 305.

(12) Zhou, Q.; Boyle, P. D.; Malpezzi, L.; Mele, A. Shin, J.H.; Passerini, S.; Henderson, W. A. *Chem. Mater.* **2011**, 23, 4331.

(13) Rosol, Z. P.; German, N. J.; Gross, S. M. *Green Chem.* **2009**, 11, 1453.

(14) Bayley, P. M.; Lane, G. H.; Rocher, N. M.; Clare, B. R.; Best, A. S.; MacFarlane, D. R.; Forsyth, M. *Phys. Chem. Chem. Phys.* **2009**, 11, 7202.

(15) Martyba, G. J.; Tuchkerman, M.; Tobias, D. J.; Klein, M. *J. Mol. Phys.* **1996**, 87, 1117.

(16) Palmer, B. J. *J. Comput. Phys.* **1993**, 104, 470.

(17) A fraction of the Ntf2 anions approaching within 4 Å of a Li+ contribute two oxygen atoms to Li+ coordination.

(18) Bayley, P. M.; Best, A. S.; MacFarlane, D. R.; Forsyth, M. *Phys. Chem. Chem. Phys.* **2011**, 13, 4632.

(19) Tokuda, H.; Ishii, K.; Susan, M. A. B. H.; Tsuzuki, S.; Hayamizu, K.; Watanabe, M. *J. Phys. Chem. B* **2006**, 110, 2833.

(20) Borodin, O. J. Phys. Chem. B **2009**, 113, 11463.

(21) Bayley, P. M.; Lane, G. H.; Lyons, L. J.; MacFarlane, D. R.; Forsyth, M. *J. Phys. Chem. C* **2010**, 114, 20569.

(22) Bhatt, A. I.; Best, A. S.; Huang, J.; Holenkamp, A. F. J. Electrochem. Soc. **2010**, 157(1), A66.

(23) Seki, S.; Ohno, Y.; Kobayashi, Y.; Miyashiro, H.; Usami, A.; Mita, Y.; Tokuda, H.; Watanabe, M.; Hayamizu, K. Tsuzuki, S.; Hattori, M.; Terada, N. J. Electrochem. Soc. **2007**, 154(3), A173.

CHAPTER 5

EFFECT OF ORGANIC SOLVENTS ON LI^+ ION SOLVATION AND TRANSPORT IN $[PYR_{13}][NTF_2]$/[LI][NTF_2] ELECTROLYTES: A MOLECULAR DYNAMICS SIMULATION STUDY

Note that this chapter is under preparation for the Journal of Physical Chemistry B.

5.1. Introduction

Although progress has been made on performance of ILEs their principal drawbacks, namely high viscosity and hence low ion diffusivity/conductivity and, decomposition of ions on graphite anode, still hinder the commercial development of ILEs for lithium ion batteries. Currently, researchers are focusing on synthesizing low viscosity ILs and use of low viscosity additives.[1,2] However, it is reasonably difficult to design and synthesize new ILs with low viscosity that are suitable for lithium ion batteries.[3] Addition of molecular solvents as additives is, therefore, a more immediate solution. Organic solvents up to a concentration of 20 mol% have been shown to retain the non-flammability of ILEs.[4] What is more, it has been reported that the additives could effectively prevent the decomposition of ionic liquids on the negative electrode and improve reversible lithium deposition/dissolution.[5] Organic carbonates, ethers and nitriles were examined as

additives to ensure formation of stable SEI which can prevent the reduction of organic cations in ILEs.[6,7]

Organic solvents in ILEs have also been proved to have the potential to improve transport properties of ILEs not only due to the reduced viscosity but also possible changes of Li^+ solvation structure.[8,9] Investigators have examined the transport properties of $[pyr_{13}][Ntf_2]/[Li][Ntf_2]$ electrolytes mixed with the organic solvents vinylene carbonate (VC), ethylene carbonate (EC), tetrahydrofuran (THF), and toluene for lithium batteries. Enhanced ion mobility was achieved in the mixtures, indicating that ILEs diluted with organic solvent are promising materials. Importantly, the investigators pointed out that viscosity effect is not the only factor contributing to the enhanced Li^+ cations mobility and changes in Li^+- Ntf_2 association in the mixtures played a role as well. For instance, when 20 mol% EC were added into the $[pyr_{13}][Ntf_2]/[Li][Ntf_2]$ electrolyte the viscosity of the electrolyte was almost halved in the diluted electrolyte. If a pure viscosity effect occurred, the self-diffusion coefficient of all ions should be improved by a factor of two. However, even for the most improved Li^+ cations, self-diffusion coefficients were improved only by a factor of 1.6, indicating changes of ion association in the diluted systems. Addition of 20 mol % tetraglyme in to $[pyr_{13}][Ntf_2]/[Li][Ntf_2]$ electrolytes was able to reinstate viscosity, conductivity, and the ion diffusion coefficients to the value observed in the pure IL.[10] However, the diffusion of Li^+ in the diluted system is a factor of 4 faster than in undiluted one, indicating that again viscosity is not the only factor in determining Li^+ diffusion. Indeed, organic solvents are found to be able to break the anionic clusters $(Li(Ntf_2)_2)^-$ in ILEs.

Raman spectroscopy provided additional insight into composition of the Li^+ cation solvation shell in [1-methyl-3- ethylimidazolium (emim)][Ntf_2] doped with $LiNtf_2$ salt when further diluted with EC, VC[11] or oligoethers.[12] Raman measurements focused on the Ntf_2 $_sCF_3$ mode located at 742 cm^{-1} for "free" Ntf_2 and around 748 cm^{-1} for Ntf_2 directly interacting with Li^+. Lassègues et al.[12] interpreted changes of IL Raman spectrum as a function of $LiNtf_2$ concentration as formation of [$Li^+(Ntf_2)_2$] clusters. When oligoethers were added to [emim][Ntf_2]/[Li][Ntf_2] intensity of the "free" Ntf_2 band increased indicating that oligoethers dissolved $Li^+(Ntf_2)_2$ complexes and formed Li^+(oligoether) solvates.[12] Similarly, Hardwick et al.[11] found that addition of 2M EC and VC to [emim][Ntf_2]/0.5 M [Li][Ntf_2] also increased the magnitude of the "free" 742 cm^{-1} Ntf_2 peak and essentially illuminated 748 cm^{-1} band that was attributed to formation of $Li^+(Ntf_2)_2$ complexes. The conclusion was consistent with appearance of blue shifted band for EC ring breathing mode that occurs during EC direct complexation with Li^+. Recent DFT study[13] of acetonitrile (ACN) complexes with $LiNtf_2$ showed that 742 cm^{-1} band exhibits a blue shift by 5-8 cm^{-1} upon Li+ complexation in $Li^+(Ntf_2)_2$, $(ACN)_2$-$LiNtf_2$, $(ACN)_2$-[$Li^+(Ntf_2)_2$]$^-$ and $(ACN)_3$-$LiNtf_2$ complexes with bidentate binding of Li^+ to Ntf_2^- oxygen atoms. DFT studies of $(ACN)_3$-$LiNtf_2$ complexes with monodentate Li^+ - oxygen binding scenario were found more stable than the bidentate analogs in gas phase. Interestingly, Raman $_sCF_3$ band in $(ACN)_3$-$LiNtf_2$ complexes with monodentate binding of Li^+/Ntf_2^- exhibit very minor blue shift (0-3 cm^{-1}) compared to the one observed complexes with the bidentate Li^+/Ntf_2^- binding. This observation suggested a possibility that the Li^+/Ntf_2^- complexes with monodentate binding could have been

counted as "free" Ntf_2^- anions during interpretation of Raman spectrum and will challenge the conclusion of $[Li^+(Ntf_2)_2]^-$ as the dominant complex forming in these ILs.

Although these studies provides insight into the lithium solvation structure and diffusion in organic diluted ILEs for Lithium batteries the liquid structure of and Li^+ solvation in such electrolytes has been less known, and hence the role that organic solvents play in such mixtures is still not fully understood. It has been reported that Li^+ cations in ILEs can move with their coordination shell (vehicular mechanism) or by exchanging coordinated molecules in the shell (structure diffusion mechanism) and the later can contributes about 70% to the total lithium diffusion. [14] Therefore, involving of organic solvents can possibly affect both of the mechanisms and hence the diffusion of lithium ions.

Raman spectroscopy is so far a valuable experimental tool in determining coordination environment of ions in ILEs.[8,11,12,15,16] However, further study of the influence of organic diluents on ILEs by raman spectra is prevented due to, as discussed above, the inability of Raman spectroscopy to differ monodentate Ntf_2 anions from "free" anions and the fact that there is overlap of modes for organic ions and diluents, for example, the 'breathing' mode of EC has the position same as that of pyrrolidinium cation.[8] Molecular dynamics (MD) simulations are promising research method for studying ionic liquids and their mixtures with lithium salt and/or organic solvents.[14,17,18] Particularly, MD simulations are well suited for exploring structure and transport in ILEs since ions move sufficiently far on the time scales accessible to MD simulations to permit the determination of transport properties and equilibrium structure. Our previous work validated the many-body polarizable APPLE&P® force fields for N-alkyl-N-methylpyrrolidinium[pyr_{1R}] cations,

bis(tribluoromethanesulfonyl)imide [Ntf_2] anions including interactions of [Ntf_2] with [Li^+], and various organic solvents.[19-20] [pyr_{1R}][Ntf_2] ILs doped with 25mol% [Li][Ntf_2] were first successfully studied by MD simulations using the developed force field.[14] Li^+ cations were found to be, on average, coordinated by four Ntf_2 anions, forming the stable $(Li(Ntf_2)_4)^{3-}$ clusters. Importantly, through the investigation of the Li^+ cations transport mechanism, the investigators claimed that Li^+ cations move primarily by exchanging Ntf_2 anions in their first coordination shell via a structure-diffusion mechanism. Only about 30% of the total diffusion is due to vehicular mechanism (Li^+ cations move with their coordination shells as clusters). In Chapter 3, simulation studies of the influence of lithium salt concentration on the structural and transport properties of x[pyr_{13}][Ntf_2]/(1-x)[L][$LiNtf_2$] electrolytes again shows accurate prediction of ion self-diffusion coefficients and ionic conductivity. Investigation of Li^+ salvation structure indicates that Li^+ cations could be coordinated by either 3 or 4 Ntf_2 anions in the electrolytes. Very few fraction of $(Li(Ntf_2)_4)^{3-}$ structure was observed when $x \leq 0.20$ but at $x = 0.33$ the ratio of the two solvation structures could be close to 1.

In this work, we extend our study to examine 0.16 [Li][Ntf_2]-0.84[pyr_{13}][Ntf_2] electrolytes with added organic solvents, focusing on the influence of organic solvents on the Li^+ solvation and ion transport properties. As to the organic solvents, we selected ethylene carbonate (EC) and acetonitrile (ACN). EC is often used as a constituent of organic electrolytes for LIBs and known to play an important role in formation of the SEI film which prevents further electrolyte decomposition and provides good reversibility for lithium intercalation/deintercalation. Therefore, EC is expected to play the same role in ionic liquid based electrolytes. What is more, EC has high dielectric constant (≈90) which

promotes ion dissociation and acceptable viscosity (1.9cP at 40 ℃) that fosters ion diffusion. As a low-viscous aprotic liquid, ACN is expected to considerably enhance ionic mobility in ILEs. ACN is also well known for its good conductivity and strong permittivity.[22] Solvation interaction between ACN and ion is relatively straightforward due to the single electron lone-pair in ACN molecule which makes the diluents either coordinate or uncoordinated to a single Li^+ cation.

To the best of our knowledge, this is the first MD simulation study performed on ionic liquid/lithium salt mixtures with added organic solvents. In this contribution, we first examine the thermodynamic and structure properties of the electrolytes followed by analysis of the Li^+ solvation in the ILEs with added organic solvents. For comparison purpose, the pure IL and IL/Lithium salt systems were also examined here. The liquid transport properties were also calculated and Li^+ transport mechanisms in such mixtures were examined.

5.2. Molecular Dynamics Simulation Methodology

Aversion of the molecular dynamics simulation package *Lucretius* that includes man-body polarization was used for all MD simulations. A three-dimensional, periodic cubic simulation cell consisted of 25 [Li][Ntf_2] and 133 [pyr_{13}][Ntf_2] molecules are simulated as the neat electrolytes. The organic diluted electrolyte systems contained 32 EC or ACN, 125 [pyr_{13}][Ntf_2], and 25 [Li][Ntf_2]. All the systems were simulated at 423 K, 393 K, 363 K (systems at 333 K and 298 K were also conducted but production run is only long enough for accurate extraction of density). The starting configurations of the electrolytes at low temperature were taken from the configuration of the corresponding electrolytes at the closest higher temperature. Since we used a parallelized *Lucretius* to run the systems

at 423K, the number of ions was changed to 24 [Li][Ntf_2] and 132 [pyr_{13}][Ntf_2] for neat electrolytes and 32 EC or ACN, 124 [pyr_{13}][Ntf_2], and 24 [Li][Ntf_2] for the diluted systems. All systems were first running in NPT ensembles for at least 20ns. The equilibrium cell sizes obtained from NPT runs were then used in the subsequent runs in NVT ensembles. The production runs used in calculation of all the properties are more than 40 ns for all systems.

A Nosé-Hoover thermostat and a barostat[23] were used to control the temperature and pressure with the associated frequencies of 10^{-2} and 0.5×10^{-3}fs. Bond lengths were constrained using the Shake algorithm to utilize a larger time step. The long-range electrostatic forces, including forces between partial charges with partial charges and partial charges with induced dipoles, were treated by Ewald summation method. The induced dipole-induced dipole interactions was drove to zero at cutoff distance of 11.0 Å by a tapering function, with scaling starting at 8.5, 9.5, and 10.2 Å for EC diluted, neat, and ACN diluted electrolytes, respectively. We also employed a multiple time step reversible reference system propagator algorithm. Time step of 0.5fs, 1.5fs, and 3.0fs for bonding, bending, and torsional motions, for nonbonded interactions within a 6.5 (EC diluted system) or 7.0Å sphere, and for nonbonded interactions between 6.5 or 7.0 and 11.0 Å and reciprocal space part of the Ewald summation were adopted in all the simulations, respectively.

5.3. Results and Discussion

5.3.1. Thermodynamic and Structure Properties

The densities of 0.16 [Li][Ntf_2]-0.84[pyr_{13}][Ntf_2] electrolytes with/without added organic solvents at each temperature are listed in Table 5-1. As can be seen from the table,

Table 5-1. Density (ρ, kg/m^3) of investigated systems at 423 K, 393 K and 363 K (Uncertainty for reported density is less than 1.5 kg/ m^3)

T (K)	Neat	20 mol%		40 mol%	
		EC	ACN	EC	ACN
423	1377	1383	1366	1257	1297
393	1402	1395	1377	1282	1324
363	1428	1421	1404	1307	1350
293(exp.[8])	1470	1470	N/A	N/A	N/A

MD simulations yield densities of electrolytes within about 1% of available experiment data. Similar quality of density predictions for the ionic liquids and their mixtures were previously reported as well, indicating that the force field developed in our group consistently predicts a density in excellent agreement with experiment.

The structure of the ILs can be well exposed by ion center of mass radial distribution fuctions (RDFs). The small peak of the center of mass RDFs (Figure 5-1) for EC–EC and ACN–ACN indicates that the organic solvents are not completely randomly distributed in the systems and the solvent molecules very slightly aggregate in the electrolytes. This is in agreement with the optimized geometry of $(ACN)_2$ - Li - $(Ntf_2)_2$ complexes in which the second ACN molecule does not bound to the Li^+ cation but located in proximity.[13]

It has been reported that Li^+ can be strongly coordinated by oxygen atoms from Ntf_2 anions[14], carbonyl oxygen atoms (O_c) from EC[24] and nitrogen atoms from ACN[13]. In

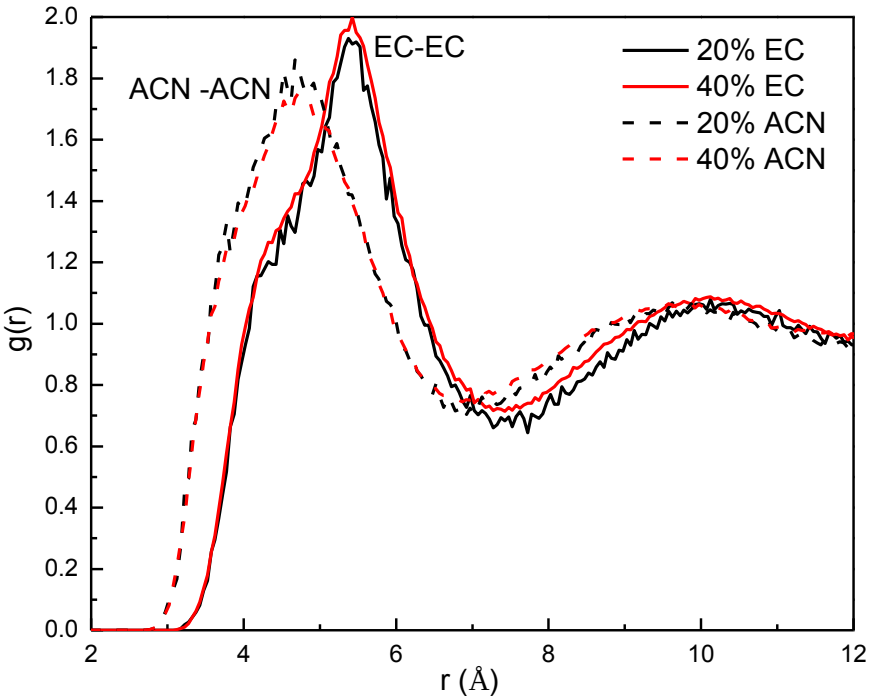

Figure 5-1. Molecular center-of-mass EC-EC and ACN-ACN radial distribution functions (g(r)) obtained from simulations at 423K.

Figure 5-2, we show the Li^+-O^{Ntf2}, Li^+-O_c^{EC}, and Li^+-N^{ACN} RDFs for all the electrolytes at 423 K. The strong peaks at small distance in the above RDFs indicate that Li^+ cations are closed approached by EC, CAN, and Ntf_2. The density weighted integral of the Radial distribution functions in Figure 5-2 yields the accumulated coordination number of oxygen and nitrogen atoms around the Li^+cation and the results are shown in Figure 5-3. From the RDFs, we determine the Li^+-O^{NTF2}, Li^+-O_c^{EC}, and Li^+-N^{ACN} first coordination shell by an r < 2.8 Å criteria which is the end of the first peak. Similarly, we define the Li^+- N^{NTF2} separation r < 5.3 Å. Temperature dependence of RDFs and coordination number are negligible for the simulated systems and thus results for other temperatures are not shown here.

As can been seen in Figure 5-3, the Li^+ cations are, on average, coordinated by 4.1 O^{NTF2} in the neat electrolyte. As expected, upon addition of the organic solvents in to the neat electrolyte, the Li^+ coordination number in both diluted electrolytes is reduced. More reduction of Li^+ coordination number is observed in ACN containing electrolytes, for example, reduction of 0.3 and 0.7 are obtained in 40 mol% EC and ACN electrolytesat 423 K, respectively. What's more, the reduction seems to be concentration dependence, that is, the higher the organic molecules concentration, the less of O^{NTF2} around a Li^+cation. Influence of ACN molecules also tends to be more concentration dependent. Interestingly, we notice that the first peaks of Li^+- Oc^{EC} and Li^+-N^{ACN} RDFs are almost at the same distance as that of Li^+-O^{NTF2} RDFs, indicating that organic molecules does coordinate to the Li^+ cations. A close comparison between Li^+- Oc^{EC} and Li^+- N^{ACN} RDFs suggests that the N^{ACN} atoms interacts strongly with the Li^+ cations, which is comparable to that of O^{NTF2}. EC molecules, however, show a relative weaker interaction to Li^+

Figure 5-2. Li^+- O^{Ntf2}(a) ,(b), Li^+- N^{ACN} and Li^+- O_c^{EC} (c) radial distribution functions (g(r)) at 423K.

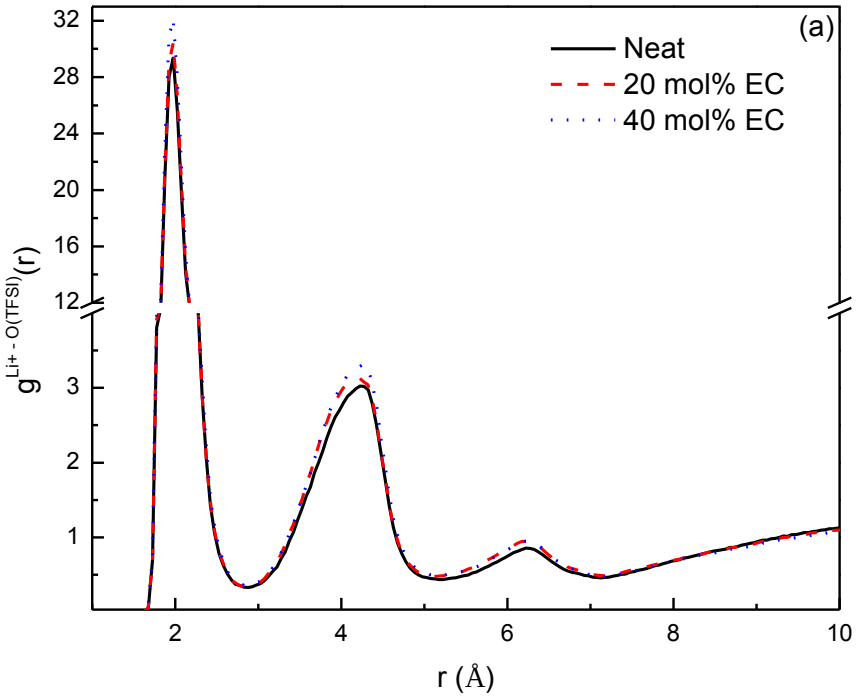
(a)
Neat
20 mol% EC
40 mol% EC
$g^{Li+ - O(TFSI)}(r)$
r (Å)

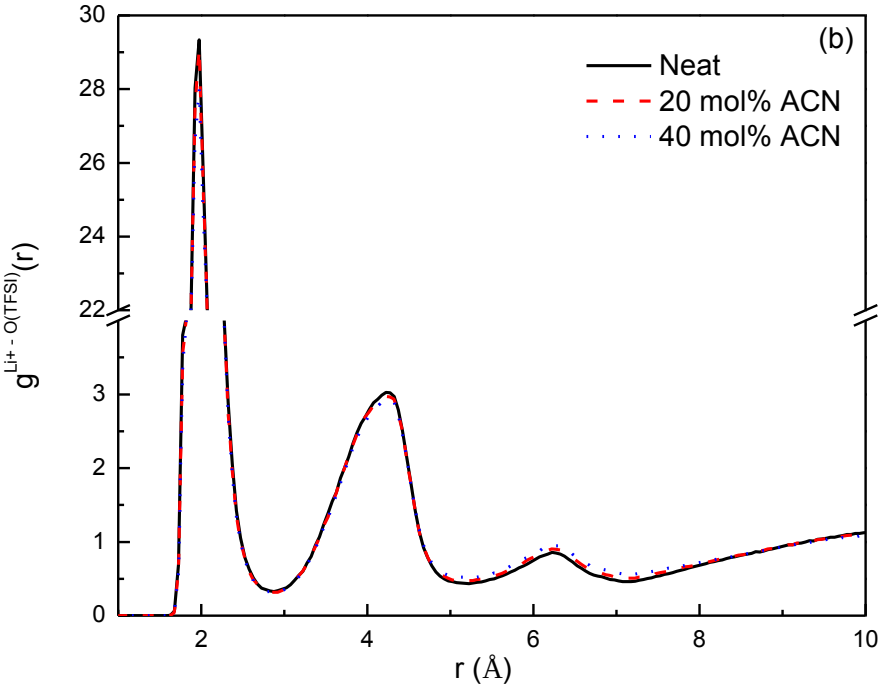
(b)
Neat
20 mol% ACN
40 mol% ACN
$g^{Li+ - O(TFSI)}(r)$
r (Å)

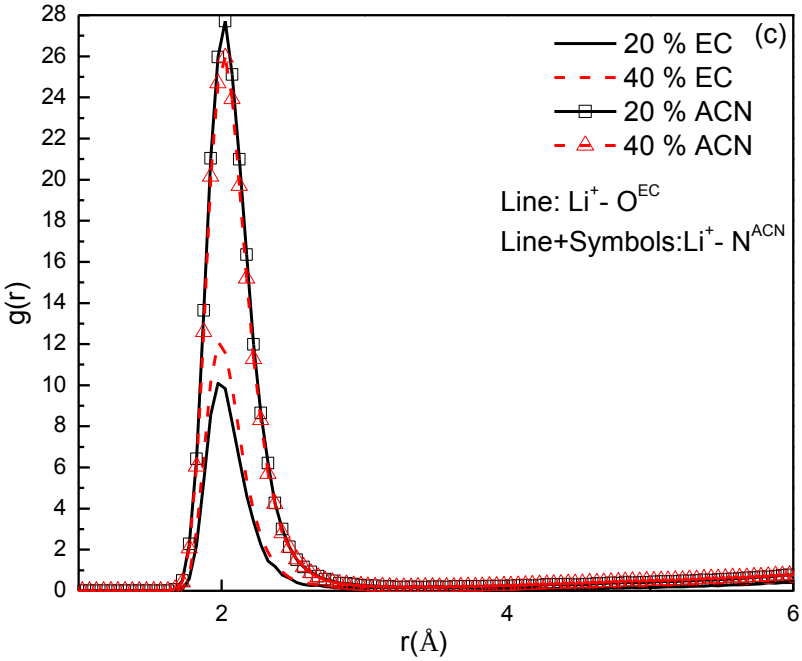
(c)
20 % EC
40 % EC
20 % ACN
40 % ACN
Line: Li+- OEC
Line+Symbols:Li+- NACN
g(r)
r(Å)
0
2
4
6
8
10
12
14
16
18
20
22
24
26
28

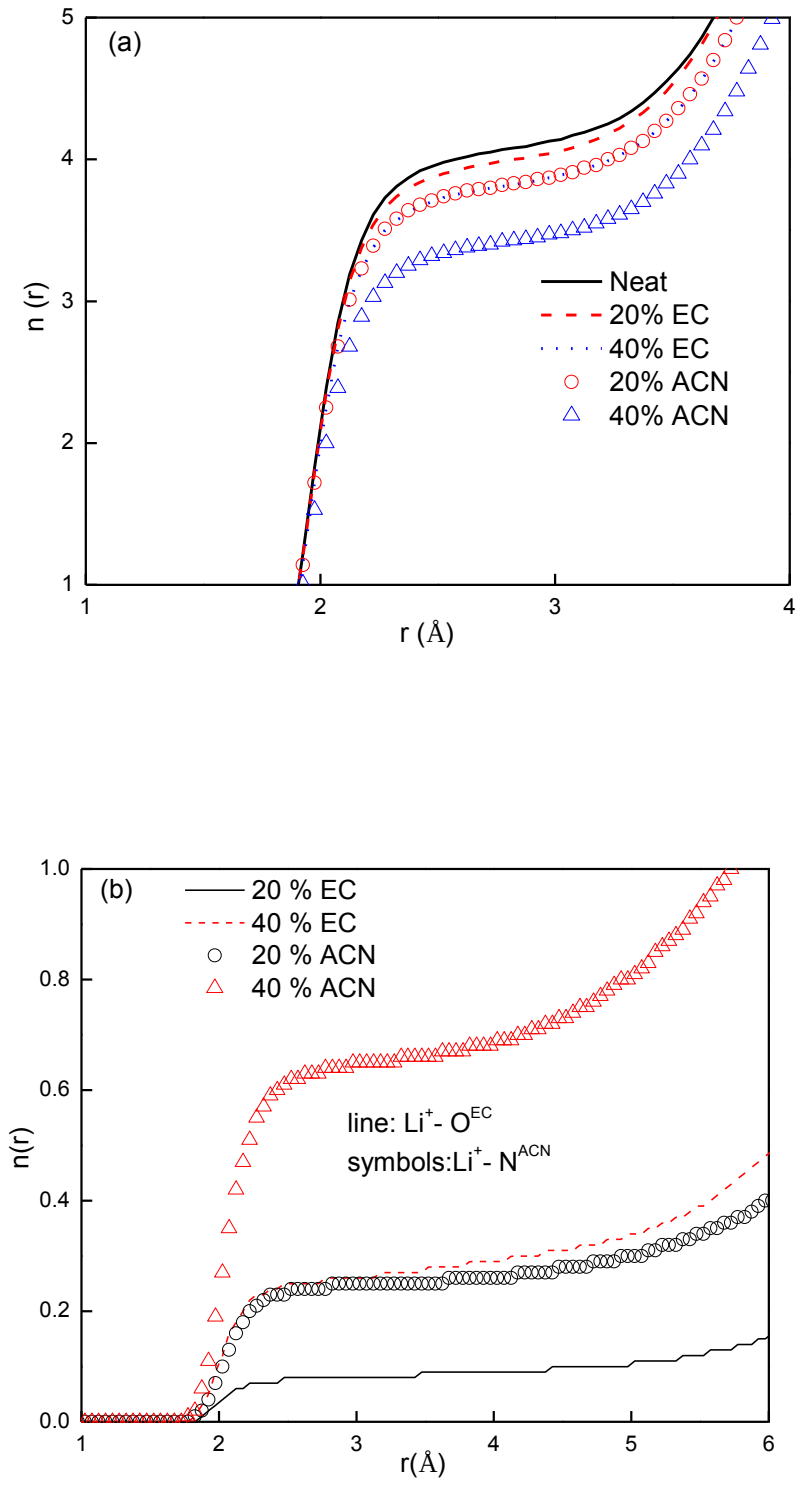

Figure 5-3. Coordination number of oxygen from Ntf_2 (a) and EC (b) and nitrogen atoms from ACN (b) around the Li^+ cation.

cations. This may well explain what we observed above that ACN solvent tend to have more influence on the $(Li^+(NTF2)_n)^{(n-1)-}$ clusters. Since those organic solvent molecules are small, we believe the number of O_c^{EC} and N^{ACN} coordinating a Li^+ cation can well represent the number of molecules around a Li^+ cation. As shown in Figure 5-3 b, within 2.8 Å, there are on average 0.08 and 0.26 Oc^{EC} atoms around a Li^+ cation in 20 and 40 mol% EC electrolytes, respectively. The number of N^{ACN} atoms within the Li^+ first coordination shell in 20 and 40 mol% ACN electrolytes, however, is almost 3 times of the number of O_c^{EC} in corresponding EC containing electrolytes. This indicates that, at the same diluting level, ACN molecules have more ability to scavenge the Li^+ away from Ntf_2 anions. In other words, at relatively lower ACN concentration the molecules might be able to completely remove Ntf_2 anions around Li^+ cations.

We previously show that Li+ cations can be coordinated by bidentate or monodentate Ntf2 anions. Thus, it would be interesting to see if the organic molecules have effect on how the anions coordinate to a Li+ cation and how those organic solvent changed the anions around a Li+ cation. Li+- N^{ntf2} RDFs for neat and diluted electrolytes are shown in Figure 5-4. As expected, EC and ACN molecules affect anions around Li+ cations differently. At low concentration, the first maximum of the first peak of Li+- N^{ntf2} RDFs for diluted electrolytes are identical and slightly lower than that for neat electrolyte, indicating that the number of anions in bidentate structure is reduced in diluted electrolytes. Changes for the second peaks also imply that EC might not affect the anions in monodentate structure but ACN does. At high concentration, however, the completely contrary influence of EC and ACN on the first maximum of the first peak is noticed for electrolyte containing organic solvents. Change for the second peaks is similar to that at

Figure 5-4. Li^{+}- N^{Ntf2} radial distribution functions (g(r)) and the coordination number in neat and diluted electrolytes.

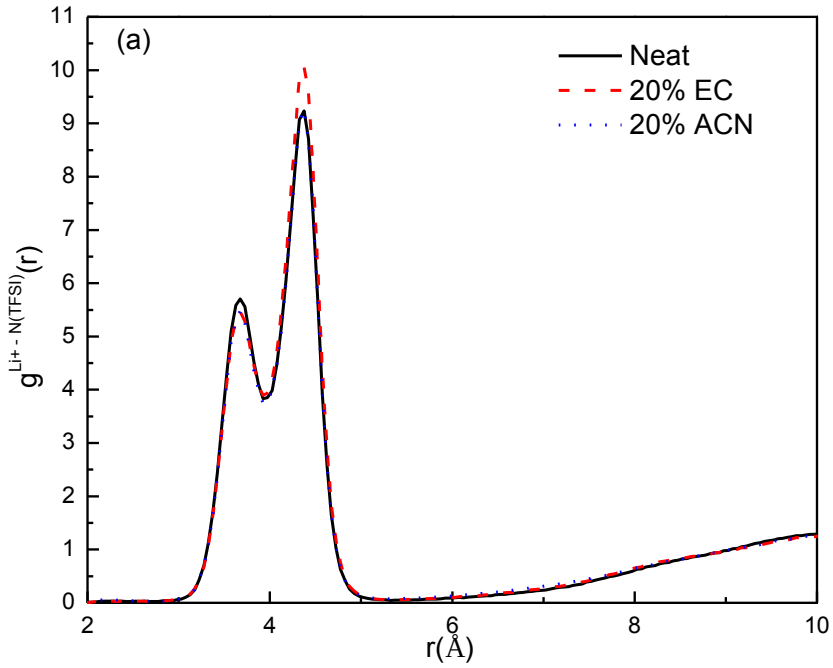
(a)
Neat
20% EC
20% ACN
$g^{Li+ - N(TFSI)}(r)$
r(Å)
0
1
2
3
4
5
6
7
8
9
10
11
2
4
6
8
10

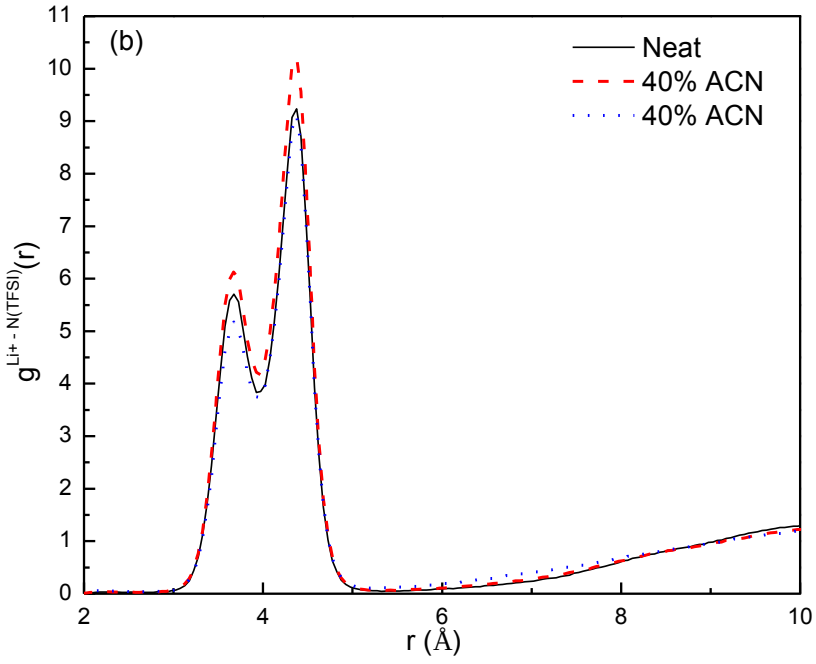
(b)
Neat
40% ACN
40% ACN
$g^{Li+ - N(TFSI)}(r)$
r (Å)
0
1
2
3
4
5
6
7
8
9
10
11
2
4
6
8
10

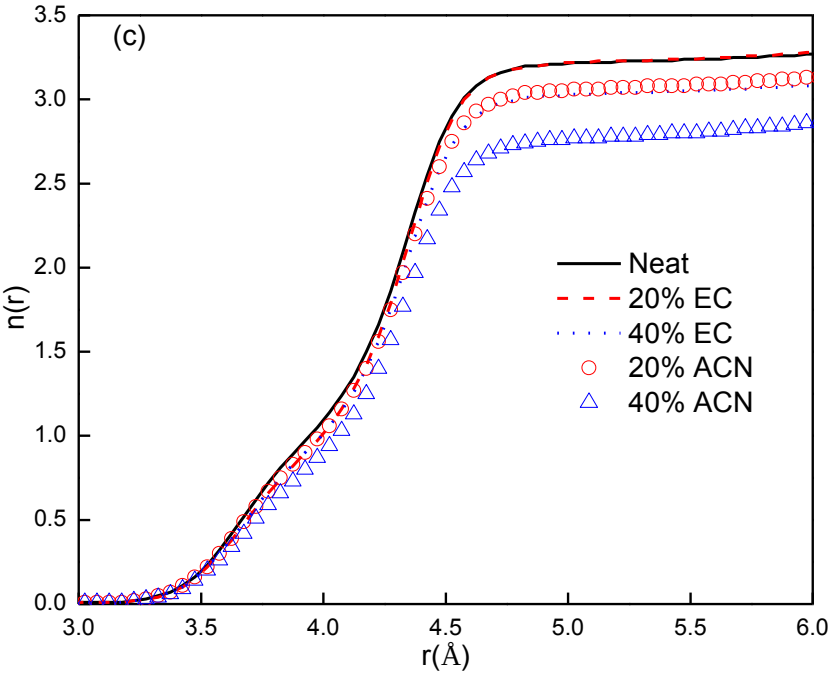
(c)
n(r)
r(Å)
Neat
20% EC
40% EC
20% ACN
40% ACN
3.5
3.0
2.5
2.0
1.5
1.0
0.5
0.0
3.0
3.5
4.0
4.5
5.0
5.5
6.0

low concentration. A further look at the Li^+- N^{NTF2} coordination number confirms what we just observed. As shown in Figure 5-4c, when 20 mol% organic solvents were added, within about 4 Å the number of anions which are bidentate decreased identically in the two diluted systems, implying that anions in the bidentate structure transformed to monodentate structure which allows the EC/ACN molecule penetrated into the $(Li^+(NTF2)_n)^{(n-1)-}$ clusters. The structures of this complex captured from a snapshot of the simulation are shown in Figure 5-5 a, b. Between 4Å and 5.3 Å, however, the number of anions around a Li^+ cation, on average, kept unchanged when EC was added. This means that at this low concentration, EC were not able to affect those anions in monodentate structure, as shown in Figure 5-5 c where the EC molecule approached a Li^+ through the space between two monodentate anions. But Figure 5-5d shows that, even at low concentration, ACN molecules were able to replace anion in monodentate structure. The above observed changes in Li solvation structure are believed to result in the slightly reduced average number of O^{Ntf2} atoms around a Li^+ cation. When it comes to the high concentration, numbers of anions within 4 Å and 5.3 Å both dropped due to the reasonthat the EC and ACN were both able to change or replace anions in monodentate and bidentate structures around Li^+ cations. A replacement of anions by molecular solvents means there are more "free" Ntf_2 anions in the electrolytes, leading to an overall improved dynamics of the anions.

5.3.2. Transport Properties of Organic Diluted Electrolytes

The self-diffusion coefficients obtained from the MD simulations for each species in the electrolytes are plotted versus temperature in Figure 5-6. Given the fact that our systems have a slightly lower (about 0.60 M at 293K) lithium salt concentration than the

Figure 5-5. Li-Ntf_2-organic solvents complex captured from a snapshot of the diluted electrolytes.

(a)

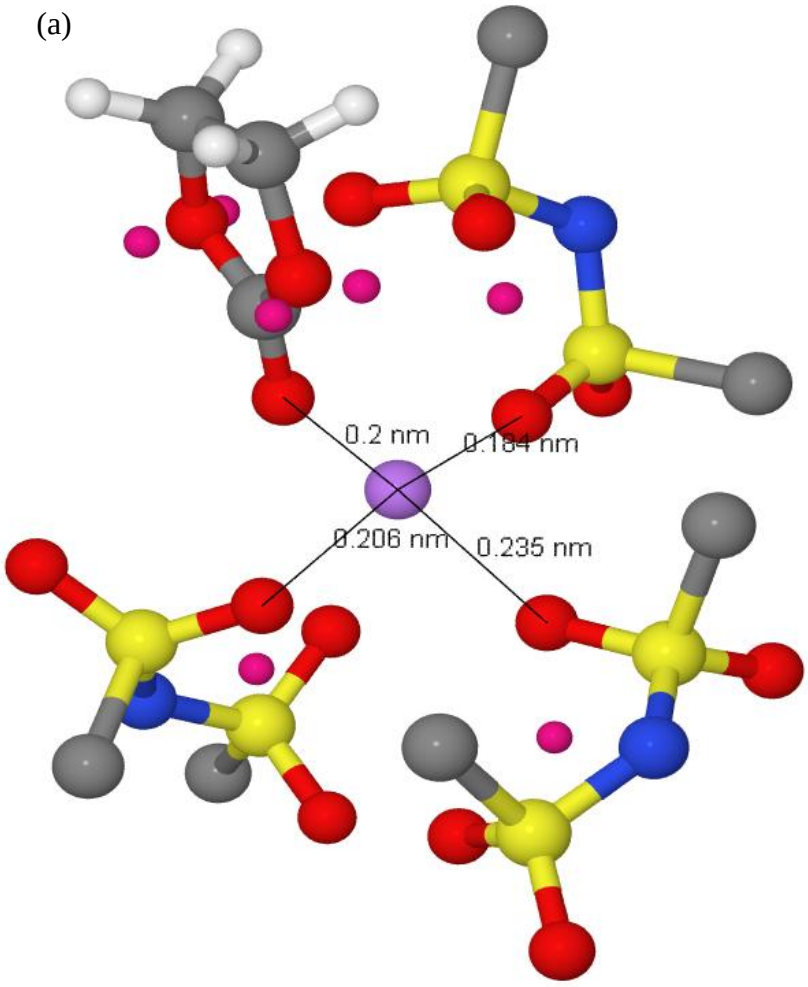

(b)

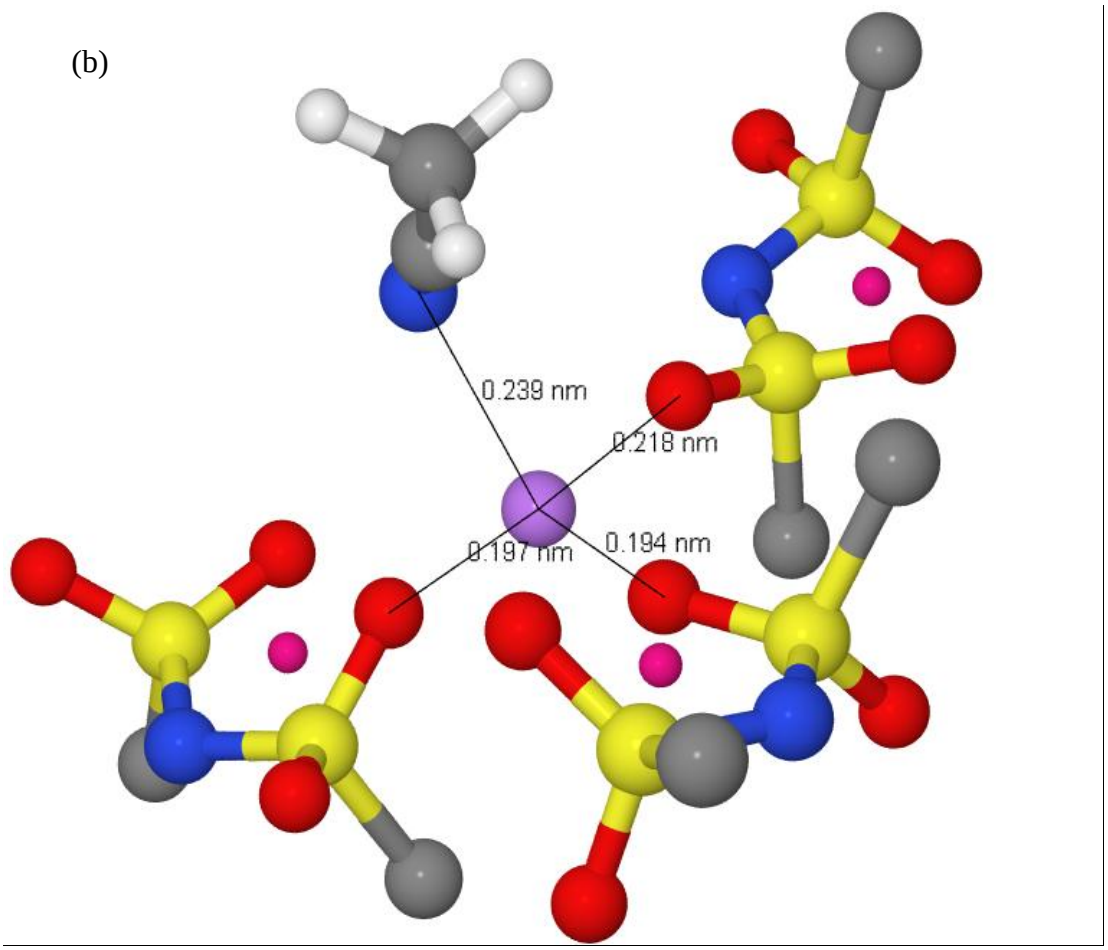

(c)

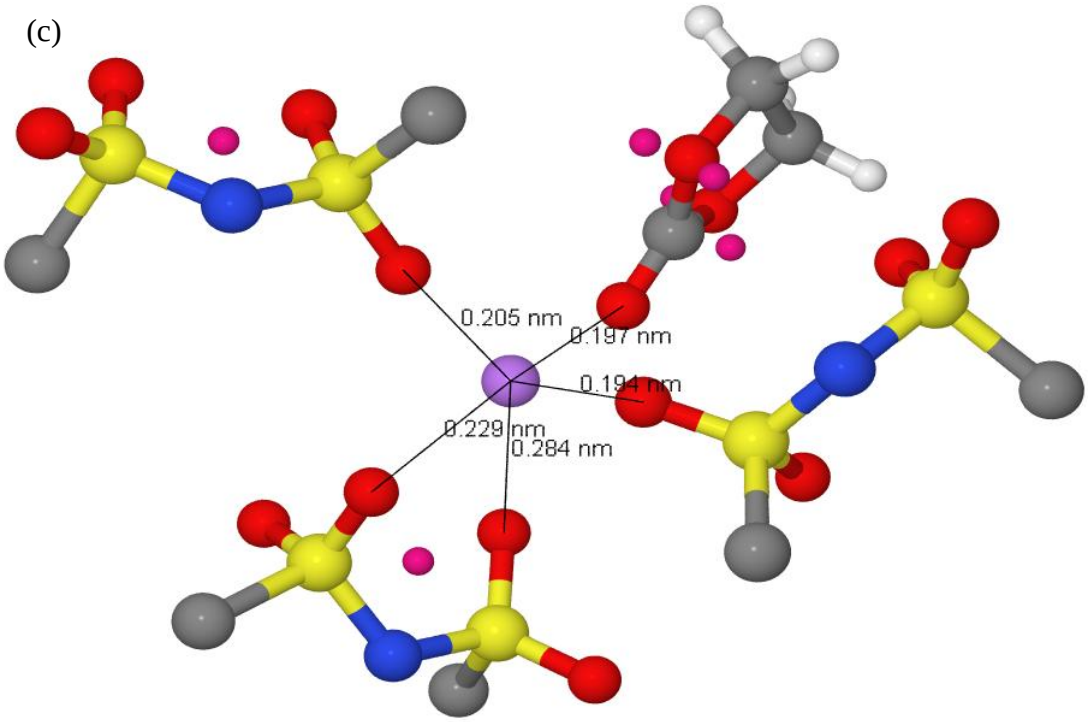
0.205 nm
0.197 nm
0.194 nm
0.229 nm
0.284 nm

(d)

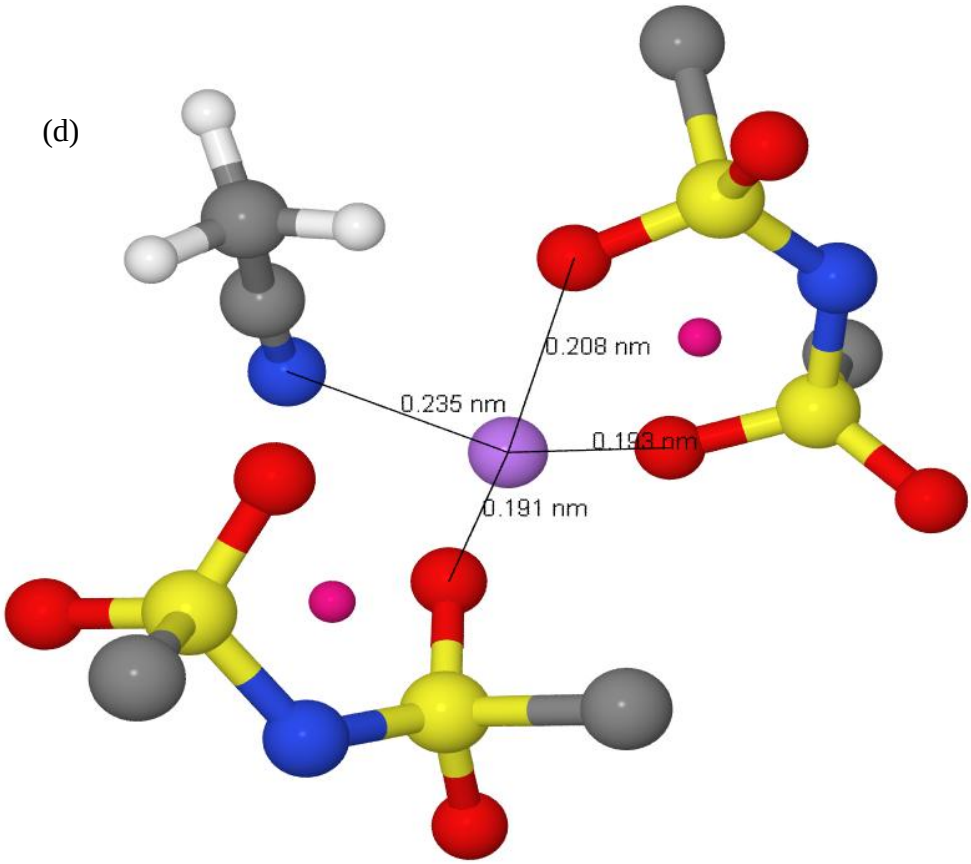
0.208 nm
0.235 nm
0.193 nm
0.191 nm

Figure 5-6. Temperature dependence of Self-Diffusion coefficients for components in Neat and diluted electrolytes. Self-diffusion coefficient in pure organic solvents is also shown. Uncertainty for reported ion self-diffusion coefficients is less than 10%.

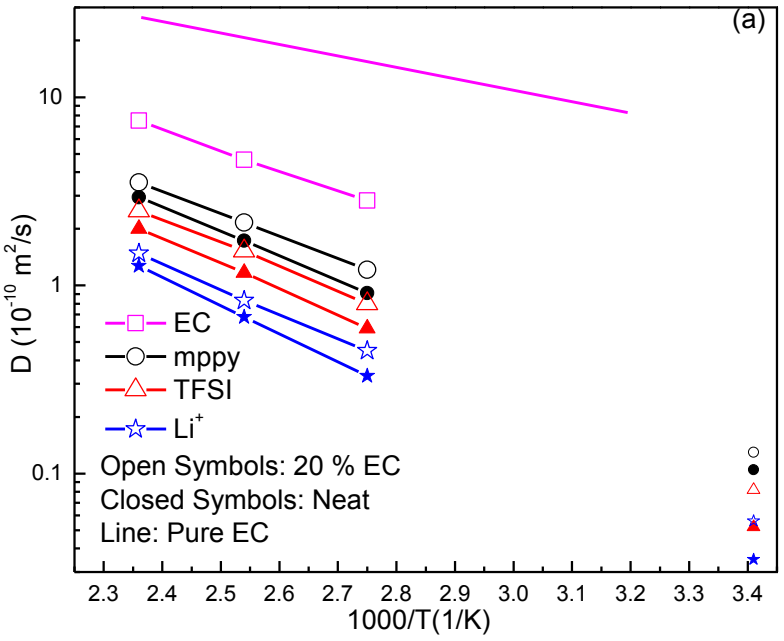
(a)
D (10^-10 m^2/s)
10
1
0.1
EC
mppy
TFSI
Li+
Open Symbols: 20 % EC
Closed Symbols: Neat
Line: Pure EC
2.3 2.4 2.5 2.6 2.7 2.8 2.9 3.0 3.1 3.2 3.3 3.4
1000/T(1/K)

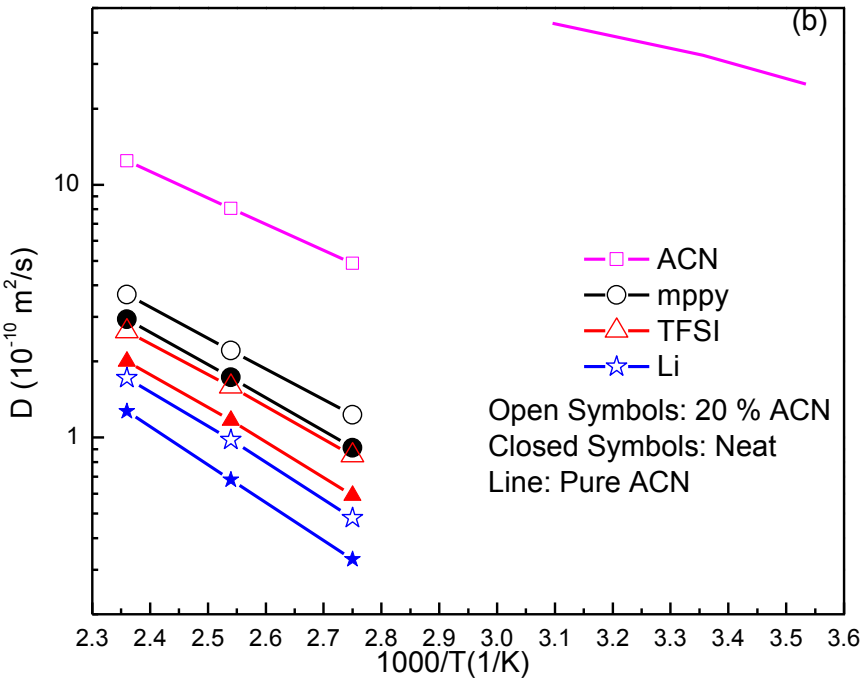
(b)
D (10^-10 m^2/s)
10
1
ACN
mppy
TFSI
Li
Open Symbols: 20 % ACN
Closed Symbols: Neat
Line: Pure ACN
2.3 2.4 2.5 2.6 2.7 2.8 2.9 3.0 3.1 3.2 3.3 3.4 3.5 3.6
1000/T(1/K)

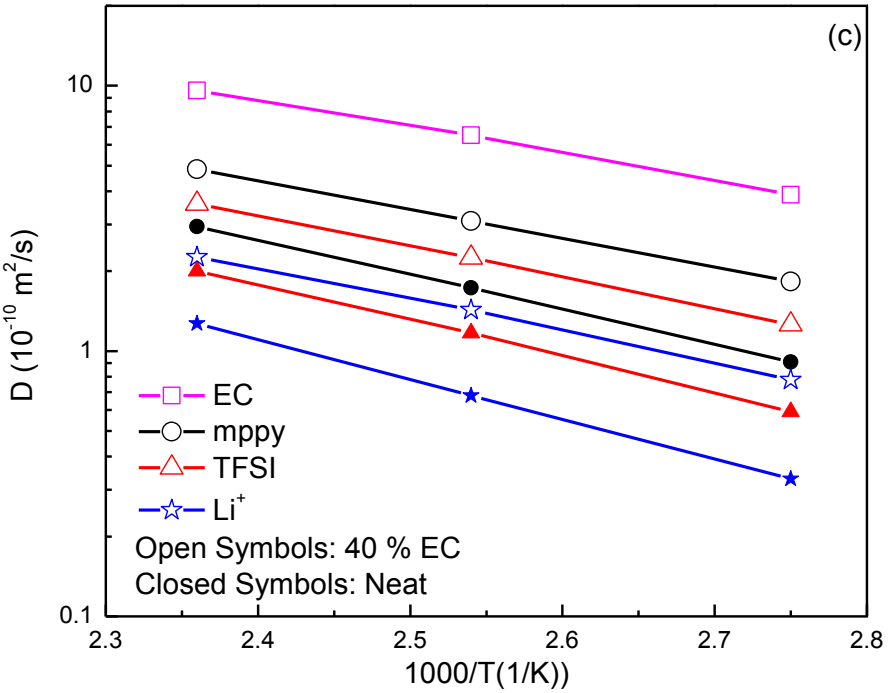
(c)
10
1
0.1
D (10^-10 m^2/s)
2.3
2.4
2.5
2.6
2.7
2.8
1000/T(1/K))
EC
mppy
TFSI
Li+
Open Symbols: 40 % EC
Closed Symbols: Neat

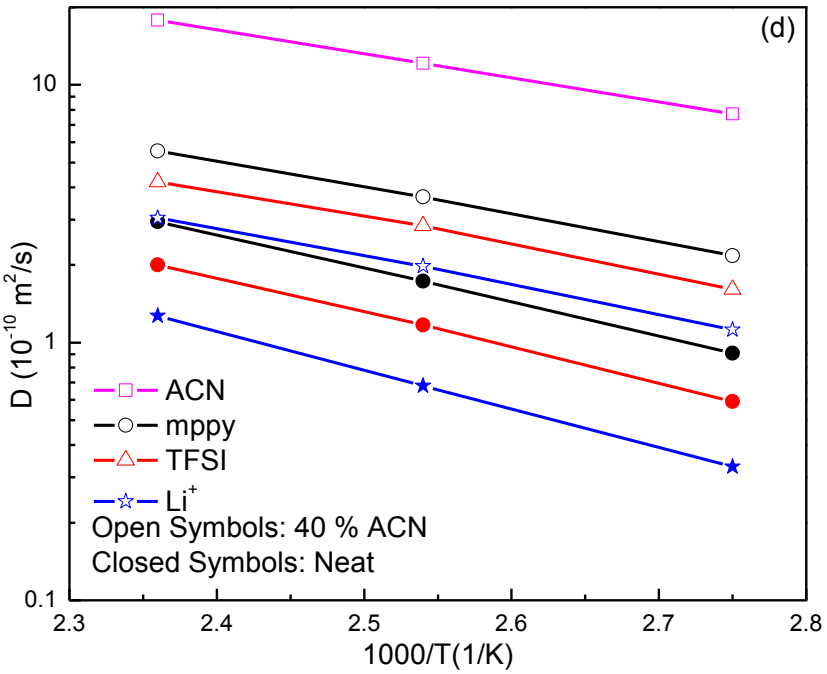
(d)
10
1
0.1
D (10^-10 m^2/s)
2.3
2.4
2.5
2.6
2.7
2.8
1000/T(1/K)
ACN
mppy
TFSI
Li+
Open Symbols: 40 % ACN
Closed Symbols: Neat

available experiments (0.65 M at 293K), an extrapolation of self-diffusion coefficients at 293K from the plot indicates that our predictionsare in very good agreement with the available experiments. As can be seen from the figures, the mobility of the components in the electrolytes follows the order ACN >EC >mppy> Ntf_2 > Li^+, which is in agreement with the experiments.[8-10] As expected, the presence of organic diluents in ionic liquid electrolyte encouragingly improves the diffusion of ions in the electrolytes. The improvement can be better understood by providing the ratio of the ion diffusion coefficient in the diluted systems to the neat one, as shown in Figure 5-7. At low organic solvent concentration (20 mol%), ACN strongly influenced Li^+ cations mobility, however, EC had influence the Ntf_2 anions the most within the simulated temperature. Addition of ACN solvent improved the diffusion of Li^+ cations by a factor up to 1.6 at low organic concentration. In agreement with experiments,[10] the influence of organic solvent on ions' mobility is temperature dependence, that is, the lower the temperature the higher the improvement of ion mobility upon adding the solvents. This is mainly due to plasticizing effect: inclusion of organic solvent which has a different Arrhenius behavior (smaller slope)[20,25] from neat ILE (as shown in Figure 5-6) results in temperature dependence of the self-diffusion coefficient of ions in between the organic solvent and neat ILE. Therefore, when temperature goes down the speed up of ions mobility is increasing. It is also obvious that the influence of organic solvents on Li^+ cations shows the strongest temperature dependence in the diluted electrolytes, thus at low concentration we actually can expect that Li^+ mobility will be mostly improved when the temperature is below 363 K. This was also observed in experiment.[8,10] At high solvent concentration, however, in both diluted electrolytes, Li^+ cation diffusion is increased the most, especially at lower

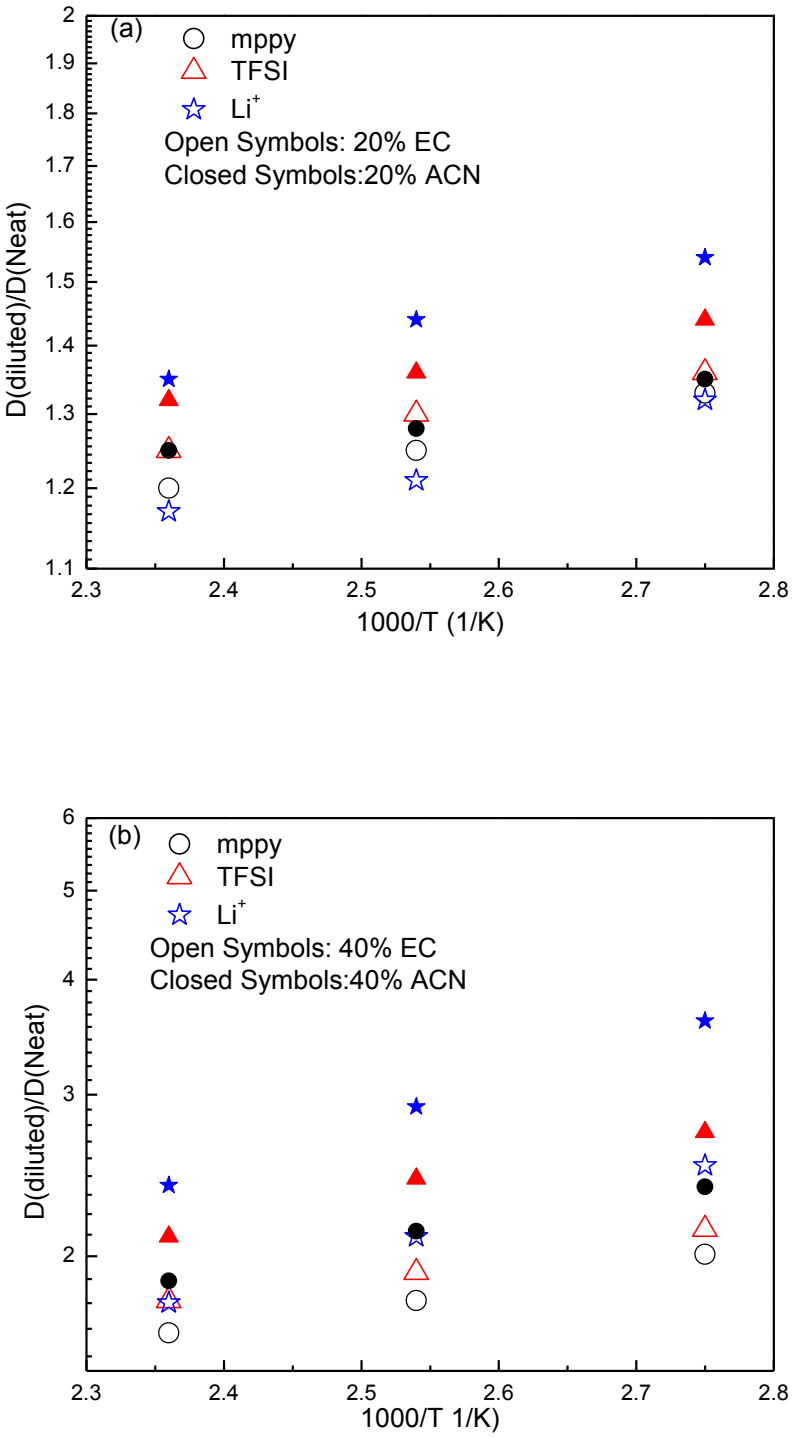

Figure 5-7. Ratio of diffusivity relative to electrolyte without organic solvents at simulated temperatures.

temperature. The enhancement of ion diffusion follows exactly the order of Li^+> Ntf_2 >mppy in both electrolytes. As can be seen from Figure 5-6, ion self-diffusion coefficients in ACN containing electrolytes are higher than those in EC containing electrolytes. Given the fact that the viscosity of the diluted electrolytes are comparable (see Figure 5-9), this can be probably attributed to that the Li^+ cation is better solvated by ACN molecules than EC in ILEs, indicating that reduced viscosity is not the only factor that results in the improvement of ion mobility.

For all the electrolytes α calculated from MD simulation lies in the narrow range of 0.62-0.86 at low concentration and shows slightly temperature and concentration dependence. The predictions of α from MD simulation are slightly larger than available experimental value which is close to 0.5 at room temperature. However, the slight temperature difference (~ 4℃) in the measured values of ionic conductivity and diffusion coefficient skewed the experimental calculations. In agreement with experiments,[10,26,27] α extracted from MD simulations of diluted systems is slightly lower than that in neat electrolyte, particularly at lower temperature, indicating that the organic molecular dilutes indeed increased the association of the ions.

Temperature dependence of ionic conductivities is shown in Figure 5-8. In agreement with available experiments, addition of 20 mol% neutral organic solvents into the ILEs results in an improvement of the ionic conductivity for the electrolytes. Despite the reduction in the number of ions per volume within the diluted ILEs, the lower viscosity of the electrolytes, and hence the higher ion diffusion of ions, can contribute to the improved conductivity. Due to more improvement of ion mobility in the electrolyte uponadding ACN than EC we observe slightly higher conductivity in former. More

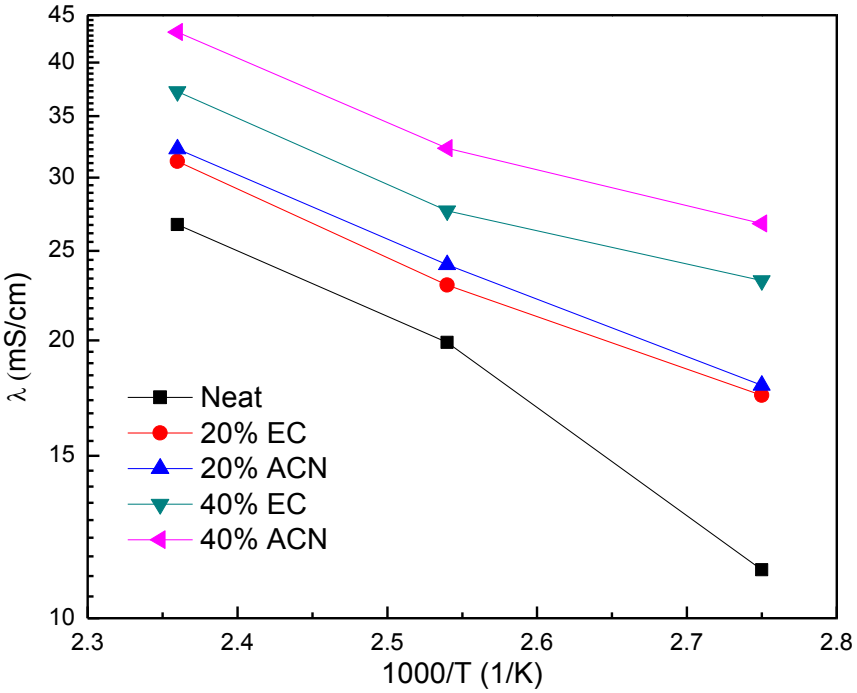

Figure 5-8. Ionic conductivity obtained from MD simulations for different systems as a function of temperature.

enhancement of ionic conductivity is realized by further addition of the solvents. Interestingly, the difference of conductivity between two diluted electrolytes increases at higher diluting level, indicating that ACN molecules have more ability to improve the ionic conductivity of ILEs than EC.

Due to the importance of Li^+ transport on the efficacy of ILEs in lithium battery applications, we examined the influence of organic solvent on the Li^+ cation transport mechanism. It is generally recognized that Li^+ cation transportation has about 30% contributions from motion with their coordination shell (of solvating anions) (vehicular mechanism) and about 70% contributions from exchanging Ntf_2 anions in the first coordination shell (structure diffusion mechanism) of the Li^+ cation.[14] In order to understand the influence of organic solvent molecules on these mechanisms we monitored Li^+-N^{Ntf2} residence times as a function of temperature and solvent concentration. The residence time ACF was calculated using

$$p_{Li^+-N^{TFSI}} = \frac{<H_{ij}(t)H_{ij}(0)>}{<H_{ij}(0)H_{ij}(0)>} \qquad (5\text{-}5)$$

where $H_{ij}(t)$ = 1 when $r_{Li^+-N^{TFSI}}$ < 5.3 Å, respectively, and zero otherwise. The ensemble average denoted by < > is taken over all Li^+ cations in the system at multiple time origins. This autocorrelation function decays from unity to zero when all Li^+ cations have completely exchanged their solvation shell of Ntf_2 anions. It was found that the ACF could be reasonable well fit with a function of the form

$$p_{Li^+-N^{TFSI}} = Aexp\left[-(t/\tau_{KWW})^{\beta}\right] \quad (5\text{-}6)$$

as shown in Figure 5-9. Figure 5-9 shows relatively rapid decay of the ACFs to zero at 423 K, indicating that there is significant rare long-lived Li^+-Ntf_2 correlations.

Given the result that β obtained from the fits is around 0.9, we believe the Li-Ntf_2 ACFs decay with almost single relaxation time behavior. Faster decay of ACF(t) are noticed when organic solvents are added into the electrolytes, indicating reduced Li^+-Ntf_2 correlations (relative fast Ntf_2 exchange). ACN again shows more influence on Li^+-N^{Ntf2} ACF. Similar behaviors are also observed for electrolytes at lower temperatures. We estimated the lifetime (τ) of the solvation shell, i.e., the time needed for a Li^+ to completely exchange solvating anions, as

$$\tau = \int_0^\infty exp\left[-(t/\tau_{KWW})^\beta\right] dt \quad (5\text{-}7)$$

Shown in Figure 5-10 is the temperature dependence of τ for all electrolytes. As expected, involving of organic solvents in the ILEs encouragingly reduces the lifetime (τ) of Li^+ solvation shell, resulting in improved structure diffusion and hence better Li^+ mobility/diffusion. The more reduction of Li^+ - Ntf_2 correlations in ACN diluted systems well explains why more improvement of Li^+ diffusion is observed in ACN containing electrolytes. It is interest to see that this improvement is temperature dependence, that is, the lower the temperature the more improvement upon addition of the solvents. In other words, at lower temperature addition of organic solvents improves more in the structure diffusion of Li^+ cations. This trend is in consistent with the observed temperature dependence of ion self-diffusion coefficient speed up factor, as shown in Figure 5-7 where ion mobility are more improved at lower temperature by organic solvents. As we discussed above, instead of completely replacing the anions around a Li^+ cation the EC or ACN molecule approaches a Li^+ cation by either replacing a monodentate Ntf_2 anion or changing the bidentate Ntf_2 anion to monodentate structure. In the latter case, this actually leads to (S $Li(Ntf_2)_3)^{-2}$ (S is the molecular solvents) clusters with larger size,

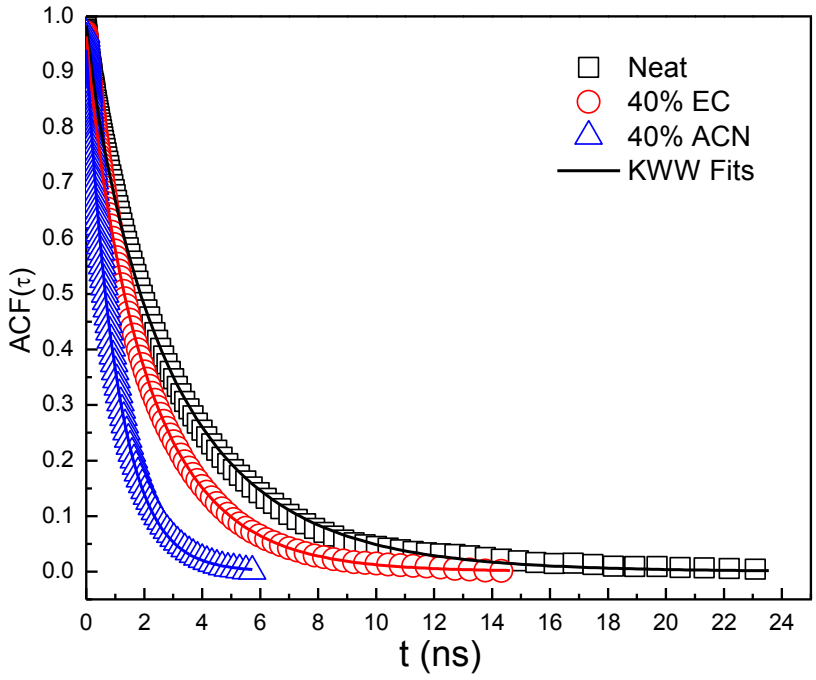

Figure 5-9. Li^{+}-N^{Ntf2} Auto Correlation Functions (ACFs) and fits at 423K.

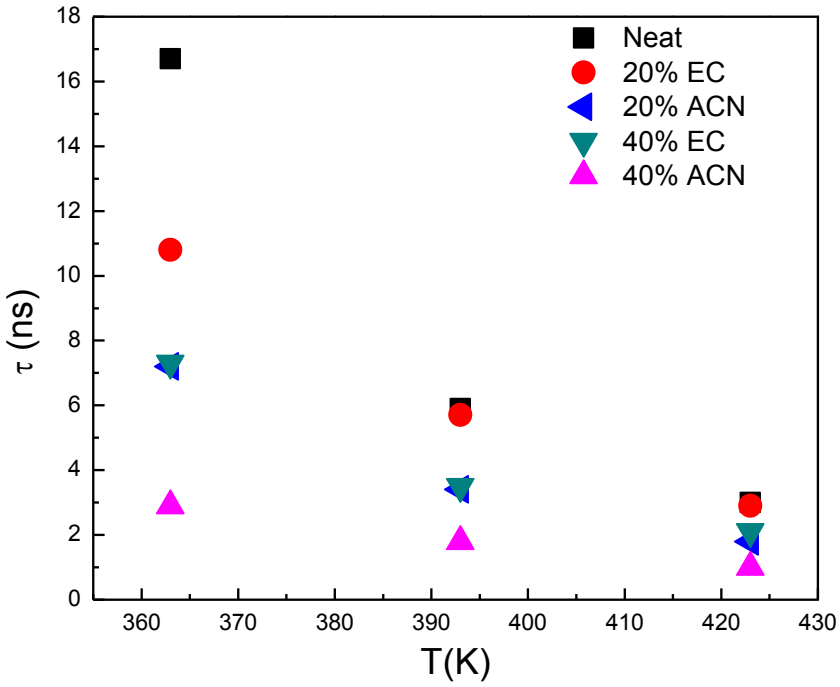

Figure 5-10. Temperature dependence of Li^{+}-N^{Ntf2} residence time (τ) obtained from MD simulations for the electrolytes.

resulting in slower vehicular diffusion of Li^+ cations. The reduced viscosities in the mixtures, however, compensate this un-favorite increase of cluster size. The increased dynamic of Li^+ cations, as well as anions, is then mainly contributed by the improved structure diffusion.

5.4. Conclusion

Addition of organic solvents is able to improve the ion transport properties in the ILEs. Incorporation of ACN in the electrolyte leads to a slightly greater enhancement of the transport properties compared to EC. The organic solvents affects the Li^+ coordination by either changing the bidentate anions to monodentate ones or by simply replacing the monodentate anions in the first coordination shell. Surprisingly, at the same diluting level, ACN molecules show more influence on the first coordination shell of Li^+ cations, i. e. more Li^+ cations in the ACN diluted electrolytes have organic solvent molecules involved in their first coordination shells. Incorporation of organic solvent in the electrolyte also reduce in the Li^+ - N^{Ntf2} correlations resulting in improved structure diffusion of Li^+ which is responsible for the improved the Li^+ ion diffusion coefficient. In one word, the addition of proper amount of organic solvent is shown to be a potential way to modify the transport properties of ions in ILEs.

5.5. References

(1) Ohno, H. H. Bull. Chem. Soc. Jpn. **2006**, 79, 1665.

(2) Bayley, P. M.; Lane, G. H.; Rocher, N. M.; Clare, B. R.; Best, A. S.; MacFarlane, D. R.; Forsyth, M. *Phys. Chem. Commun.* **2009**, 6297.

(3) Seki, S.; Kobayashi, Y.; Miyashiro, H.; Ohno, Y.; Usami, A.; Mita, Y.; Kihira, N.; Watanabe, M.; Terada, N.; *J. Phys. Chem. Phys.* **2009**, 110, 10228.

(4) Choi, J. A.; Eo, S. M.; MacFarlane, D. R.; Forsyth, M.; Cha, E.; Kim, D. W. *J. Power Sources* **2008**, 178, 932.

(5) Sato, T.; Maruo, T.; Marukane, S.; Takagi, K. *J. Power Sources* **2004**, 138, 253-261.

(6) Holzapfel M.; Jost, C.; Novak, P.; *Chem. Commun.* **2004**, 2098-2099.

(7) Katayama, Y.; Yukumoto, M.; Miura, T. *Electrochim. Solid-state Lett.* **2003**, 6(5), A96.

(8) Bayley, P. M.; Lane, G. H.; Rocher, N. M.; Clare, B. R.; Best, A. S.; MacFarlane, D. R.; Forsyth, M. *Phys. Chem. Chem. Phys.* **2009**, 11, 7202.

(9) Bayley, P. M.; Best, A. S.; MacFarlane, D. R.; Forsyth, M. *Phys. Chem. Chem. Phys.* **2011**, 13, 4632.

(10) Bayley, P. M.; Lane, G. H.; Lyons, L. J.; MacFarlane, D. R.; Forsyth, M. *J. Phys. Chem. C* **2010**, 114, 20569.

(11) Hardwick, L. J.; Holzapfel, M.; Wokaun, A.; Novak, P. *J. Raman Spectro.* **2007**, 38, 110.

(12) Lassegues, J.; Grondin, J.; talaga, D. *Phys. Chem. Chem. Phys.* **2006**, 8, 5629.

(13) Seo, D. M.; Borodin, O.; Han, S.-D.; Boyle, P. D.; Henderson, W. A. *J. Electrochem. Soc*. **2012**, 159, A1489-A1500.

(14) Borodin, O.; Smith, G. D.; Henderson, W. *J. Phys. Chem. B* **2006**, 110, 16879.

(15) Umebayashi, Y.; Yamaguchi, T.; Fukuda, S.; Mitsugi, T.; Takeuchi, M.; Fujii, K.; Ishiguro, S. *Analy. Sci. Jpn.* **2008**, 24, 1297.

(16) Shirai, A.; Fujii, K.; Seki, S.; Umebayashi, Y.; Ishiguro, S.; Ikeda, Y. *Anyly. Sci. Jpn.* **2008**, 24, 1291.

(17) Umebayashi, Y.; Hamano, H.; Seki, S.; Minofar, B.; Fujii, K.; Hayamizu, K.; Tsuzuki, S.; Kameda, Y.; Kohara, S.; Watanabe, M. *J. Phys. Chem. B* **2011**, 115, 12179.

(18) Monteiro, M. J.; Bazito, F. F. C.; Aiqueira, L. J. A.; Ribiro, M. C. C.; Torresi, R. M. *J. Phys, Chem. B* **2008**, 112, 2102.

(19) Borodin, O.; Smith, G. D.; *J. Phys. Chem. B* **2006**, 110 (23), 11481.

(20) Borodin, O.; Smith, G. D.; *J. Phys. Chem. B* **2006**, 110 (23), 6279.

(21) Borodin, O. *J. Phys. Chem. B* **2009**, 113, 11463.

(22) Arulepp. M.; Permann, L.; Leis, J.; Perkson, A.; Rumma, K.; Janes, A.; Lust, E. *J. Power Sources* **2004**, 133, 320.

(23) Martyba, G. J.; Tuchkerman, M.; Tobias, D. J.; Klein, M. *J. Mol. Phys.* **1996**, 87, 1117.

(24) Borodin, O.; Smith G. D. *J. Phys. Chem.* **2006**, 110(10), 4971.

(25) arXiv:1202.1006v1

(26) Li, W.; Zhang. Z.; Han, B.; Hu, S.; Xie, Y.; Yang, G. *J. Phys. Chem. B* **2007**, 111, 6452.

(27) Tokuda, H. *Electrochemistry* **2005**, 73, 620.

CHAPTER 6

BEHAVIOR OF ROOM TEMPERATURE IONIC LIQUIDS (RTILS) MIXED WITH LITHIUM SALT AND ORGANIC SOLVENTS NEAR CHARGED SURFACE: A MOLECULAR DYNAMICS SIMULATION STUDY

6.1. Introduction

The RTILs electrolytes have some drawbacks such as comparatively low ion diffusivity, and hence ionic conductivity, that hinders their application in LIBs. In addition, compared to conventional organic solvents the ionic liquids have poor stability on a carbon anode, restricting their commercial development. Encouragingly, addition of traditional organic solvents diluents into the ionic liquids/Lithium salt mixture enhances the ion mobility, and hence, ionic conductivity.[1,2] Incorporation of organic solvents enable the formation of a stable SEI layer on the electrode surface as well.[3-5] The SEI layer can passivate the electrodes and ultimately prevent further decomposition of the electrolytes. It is believed that the SEI layers closely relate to the local environment (i.e., coordination shell of the lithium) of electrolyte near the electrode surface,[6-8] making

insight into the structure and composition of electrolyte near electrode surface interesting. In addition, the operation of Li-ion batteries largely depends on the transport of Li^+ cations back and forth between the electrodes, as well as through the electrolyte/electrode interface. Therefore, it is of great importance to characterize the structure and properties of the RTIL-based electrolyte/electrode interface to promote the implementation of such electrolyte in LIBs.

As discussed in Chapter 4 and 5, molecular dynamics simulation studies of ionic liquid doped with lithium salt and with organic solvents have led to an improved understanding of the structure in the bulk electrolytes, in particular, the Li^+ solvation structure. In contrast, simulations of the ILEs at electrode surface are very limited.[9] Recently, multi-layers structure of the ionic liquid/electrode interface has been extensively investigated by MD simulations using the "electroactive interface" methodology.[10] Utilizing a polarizable force field, MD simulations of carbonates doped with lithium salt at the graphite surfaces with different potentials have been carried out as well.[11] These investigations improve the understanding of electrolyte structures near a surface and reveal that the composition of the electrolyte at the charged surface and the manner in which Li^+ is solvated near the surface are significantly different from the bulk. In this chapter, we continue our investigation of ILEs to study their structure near the surface of charged and uncharged graphite electrode. The simulated systems consist of $[pyr_{13}][Ntf_2]$, [Li][Ntf_2] and organic solvent EC or acetonitrile (ACN) which are confined between two basal graphite electrodes.

6.2. Simulation Methodology

Molecular dynamics (MD) simulations were performed on graphite electrodes confined electrolytes $[pyr_{13}][Ntf_2]$/[[Li][Ntf_2], $[pyr_{13}][Ntf_2]$/[[Li][Ntf_2]/EC, and $[pyr_{13}][Ntf_2]$ /[[Li][Ntf_2]/ACN. Figure 6-1 shows the chemical structure of all components in the electrolytes. The neat electrolyte contained 25 [Li][Ntf_2] and 133 $[pyr_{13}][Ntf_2]$ ion pairs, yielding a lithium salt mole fraction close to 16 %. The organic solvent diluted electrolytes consisted of 32 EC or ACN, 25 [Li][Ntf_2], and 125 $[pyr_{13}][Ntf_2]$ ion pairs, leading to 1.3 diluents per lithium cation.

The atomically flat electrode was represented by two close-packed atomic layers of graphite having 240 carbon atoms and was oriented such that the [111] crystallographic face is exposed toward the electrolyte, as illustrated in Figure 6-2. The distance between two closest neighbor electrode atoms is 2.58 Å. The asymmetry direction, defined as the axis perpendicular to electrodes surface, will be referred as z-axis. In order to simplify our analysis, positions of graphite atoms were restrained/frozen during simulations. The cross-sectional area of the system was 25.614 x 24.647 $Å^2$, and the distance between electrodes varied between 125.6 to 140.0 Å, depending on the system composition. This separation between electrodes was proved to sufficient to generate about 30-35 Å wide layer of bulk-like electrolyte in the middle of the simulation cell. Potential differences between electrodes (ΔV) are 0 V and 6.0 V.

The electrolytes were modeled with the polarizable APPLE&P force field which was shown to be able to accurately predict thermodynamics, structural, and transport properties of the bulk systems. The electrode-electrolyte repulsion-dispersion cross-terms were calculated using APPLE&P standard combining rules as mentioned in Chapter 2.

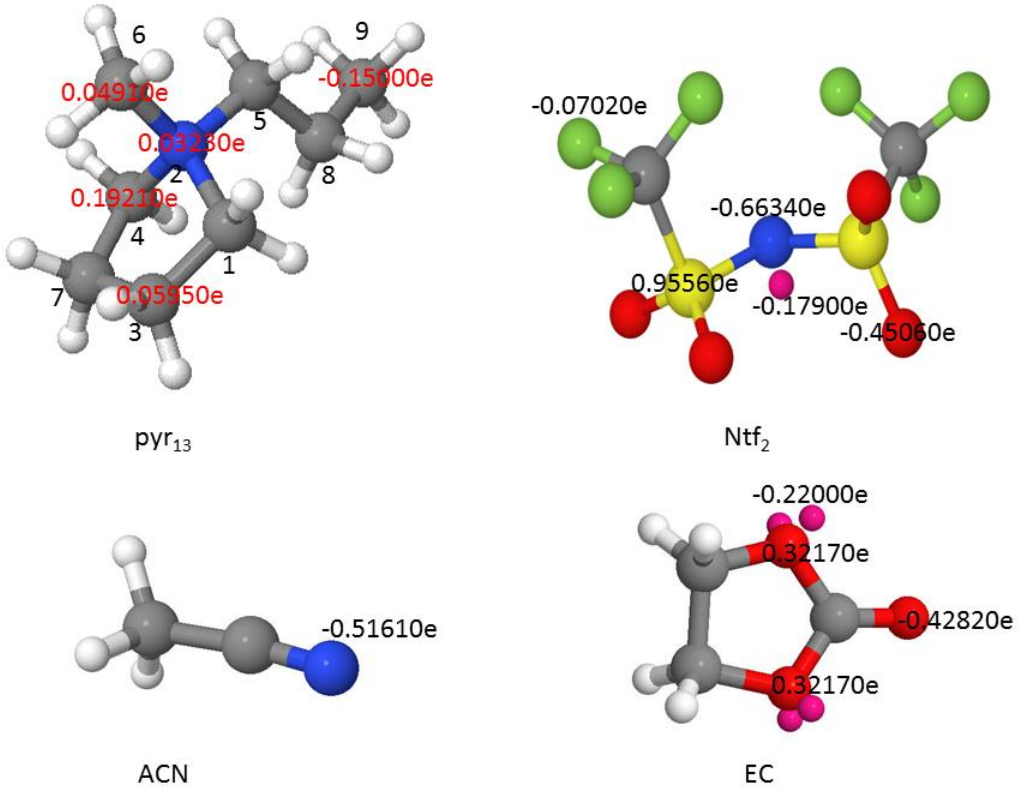

Figure 6-1. Chemical Structure of components in the simulations. Partial charges of some atoms are also shown.

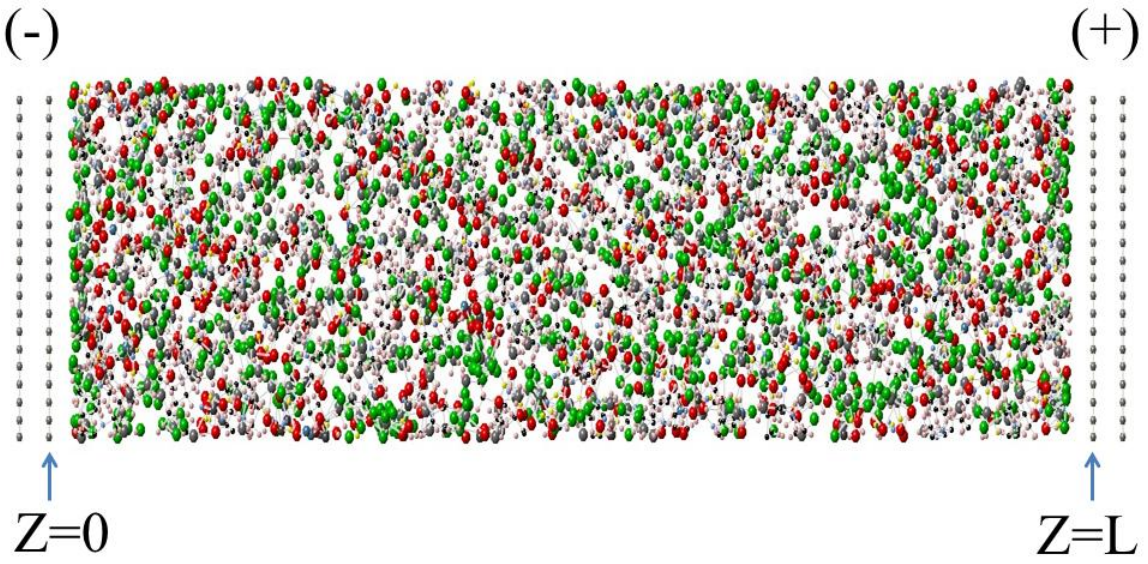

Figure 6-2. A representative configuration of the system comprising atomically flat conductive electrodes and neat electrolyte at 423 K and ΔV=0 V.

Electrodes were treated as electronic conductors with the potential difference between two electrodes constrained to a set value utilizing methodology described in Chapter 2. The electrode polarization was evaluated by minimizing the total electrostatic energy with respect to the electrode charges.

The temperatures of the systems were maintained at 423 K using a Nose-Hoover thermostat[12] with a coupling time of 0.1 ps. Covalent bond lengths were constrained using the Shake algorithm to utilize a larger time step. The long-range electrostatic forces, including forces between partial charges with partial charges and partial charges with induced dipoles, were treated by Ewald summation method. The induced dipole-induced dipole interactions was drove to zero at cutoff distance of 11.0 Å by a tapering function, with scaling starting at 8.5, 9.5, and 10.2 Å for EC diluted, neat, and ACN diluted electrolytes, respectively. We also employed a multiple time step reversible reference

system propagator algorithm. Time step of 0.5fs, 1.5fs, and 3.0fs for bonding, bending, and torsional motions, for nonbonded interactions within a 6.5 (EC diluted system) or 7.0 Å sphere, and for nonbonded interactions between 6.5 or 7.0 and 11.0 Å and reciprocal space part of the Ewald summation were adopted in all the simulations, respectively. The electrode charges were updated every 0.3 ps.

6.3. Results and Discussions

As illustrated in the MD simulations of bulk systems, the dynamics of ions significantly dropped in ionic liquids when lithium salt is added due to the formation of Li - Ntf_2 complexes. Thus, much longer trajectories than previous simulated systems[10,11] are required for MD simulations of graphite confined ILEs to ensure sufficient sampling of the phase space, making the computations expensive. Furthermore, we use the polarizable APPLE&P force field in the simulations which introduces extra interactions between and with induced dipoles to electrostatic interactions, making the calculations more expensive. The results reported here are extracted from production runs about 35 ns.

6.3.1 Role of Induced Dipoles on EDL Potential

We define the electrode potential as the Poisson potential drop across the EDL relative to the potential of zero charge (RPZC)

$$U_{RPZC} = U_{EDL} - PZC = \varphi_{electrode} - \varphi_{bulk} - PZC \qquad (6\text{-}1)$$

wheere, U_{EDL} indicates the potential drop across the electrode/electrolyte interface and PZC is the potential of zero charge. $\varphi_{electrode}$ and φ_{bulk} are the Poison potential of electrode and bulk electrolyte, respectively. The Poisson potential φ(z) along the z-direction is determined by numerically integrating the 1 D Poisson equation,

$$\frac{\partial^2 \varphi(z)}{\partial z^2} - \frac{\partial \mu(z)}{\partial z} * \frac{1}{\epsilon_0} = -\frac{q(z)}{\varepsilon_0} \quad (6\text{-}2)$$

where $\epsilon_0$is the vacuum permittivity, $\varphi(z)$ is the Poision potential, $\mu(z)$ is the density of the z-component of the induced dipoles, $q(z)$ is the charge density, and z is the distance from the electrode surface. PZC was approximated from the Poisson potential drop across the EDL at an imposed potential difference between electrodes of ∇V = 0 V. This approximation is reasonable because the total charge on the electrode at ∇V = 0 V is negligibly small. PZC for the neat, EC diluted, and ACN diluted electrolytes are -0.50 V, -0.49 V, -0.46 V. The negative PZCs are due to larger affinity of the uncharged surface for the negative O and F atoms of Ntf_2 anions (see discussion below), and may indicate a relatively low densities of Li^+ cations near the uncharged surface.

Figure 6-3 shows the Poisson potential due to fixed partial atomic charges and induced dipoles as a function of position relative to the electrode surface for neat systems at ∇V = 6 V. In agreement with what we observed in simulations of carbonate/Li salt mixtures, the large impact of inclusion polarization on the Poisson potential is noticed in the simulations of ILEs. Therefore, the relationship between electrode charge and the electrode potential predicted from a nonpolarizable model for ILEs can be in significant difference from polarizable model, particularly, at higher voltage. Similar results are observed in the diluted systems.

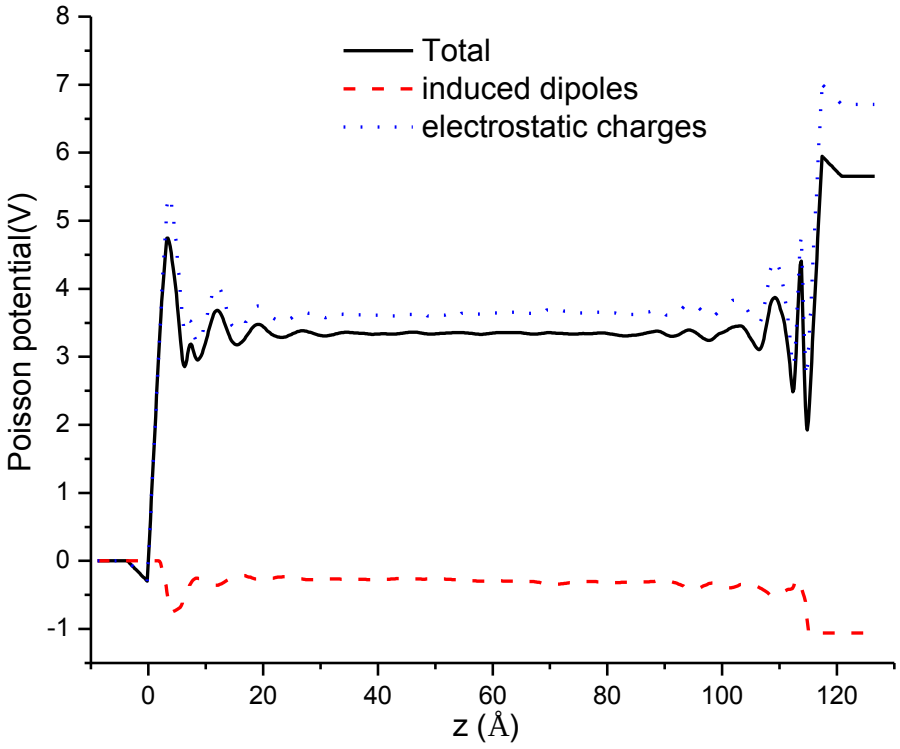

Figure 6-3. Poisson potential due to fixed charges, induced dipoles as a function of the position relative to the electrode surface for neat electrolyte at $\nabla V = 6$ V.

6.3.2. Electrode/Electrolyte Interface Structure

When an external electric field (charged electrodes) is applied to the bulk ILE which mainly consists of ions, the structure of the electrolyte near the electrode/electrolyte interface becomes ordered to "screen out" the bulk electrolyte fluid effectively from the influence of the added field.[13] Therefore, the charge density q(z), given by the difference between atom number density (plane-average) ρ_+ and ρ_-, in the bulk fluid far from the electrode/electrolyte interface is expected to be constant and zero, as shown in Figure 6-4. The constant Poisson potential in the bulk electrolyte, as shown in Figure 6-5, indicate that the applied electrostatic field $-\nabla\varphi$, vanishes away from the electrodes. In addition, we notice that the oscillation in the charge density is only within about 25 Å from the electrode, thus, structuring in the ILEs is only observed near the electrode and not in the bulk.

Ion center-of-mass density profile is a good way to look insight the interfacial structures of ILEs. Shown in Figure 6-6 are ion center-of-mass density profiles at two voltages, ΔV=0 V and ΔV=0 V 6 V. It can be clearly seen the multilayer structure of the fluid extending 20-30 Å from the electrode surface. Interestingly, even near the uncharged electrode there are multilayer structure formed near the surfaces. This was also observed in MD simulations of graphite confined [pyr_{13}][Ntf_2], [alkylimidazolium ($C_n$mim)][Ntf_2], and a simple melt salt LiCl. It was proved to result from the unequal van der Waals interactions of ions with the electrode and the size difference between ions.[10,14]

At 0 V potential difference both pyr_{13} and Ntf_2 ions populate the first layer (defined by the first peak in density profile and typically within about 6.0 Å near the surface), with a slightly larger affinity of the uncharged graphite surface for the anions. When organic

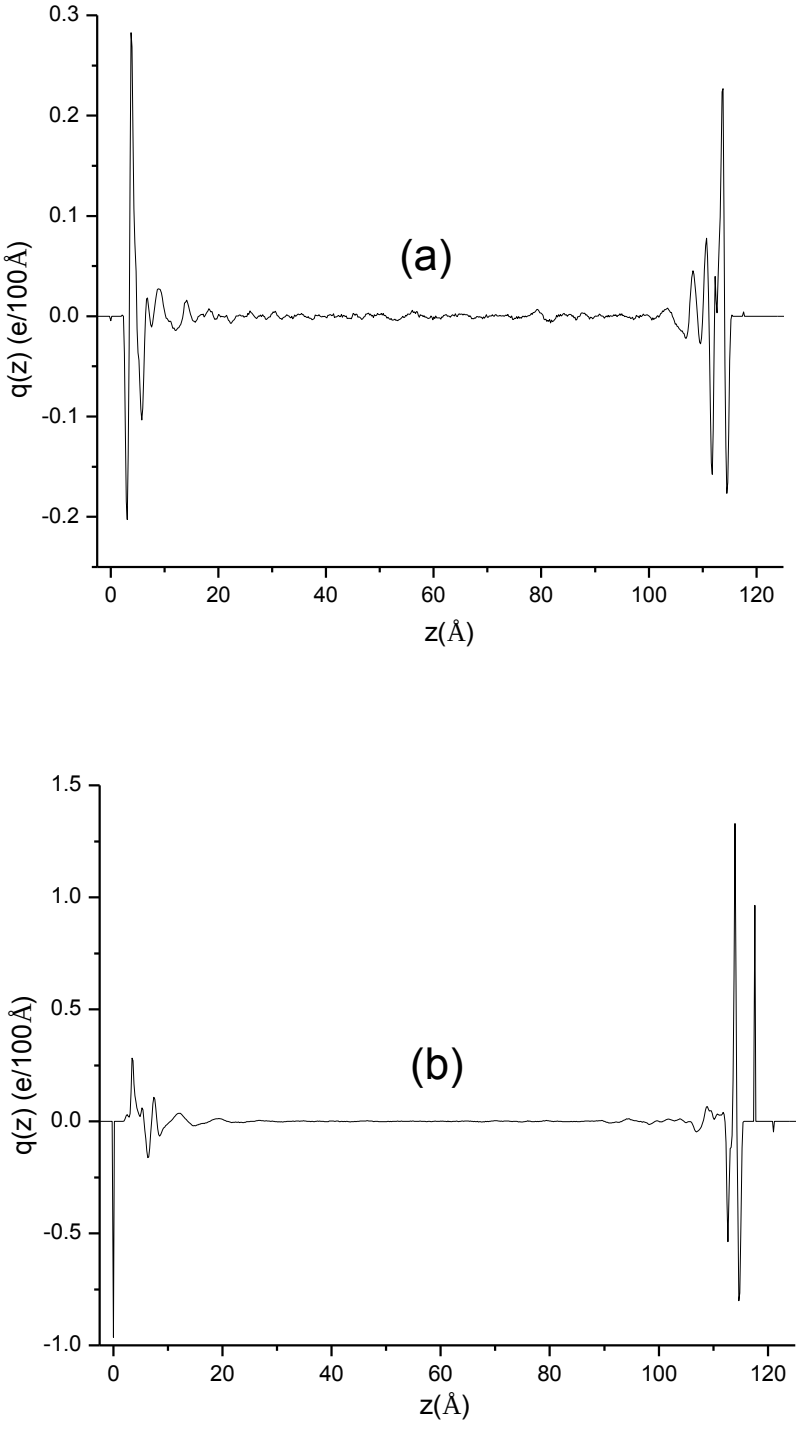

Figure 6-4. Charge density as a function of distance in Z-axis for the neat electrolyte at ΔV=0 V (a) and ΔV=6 V (b).

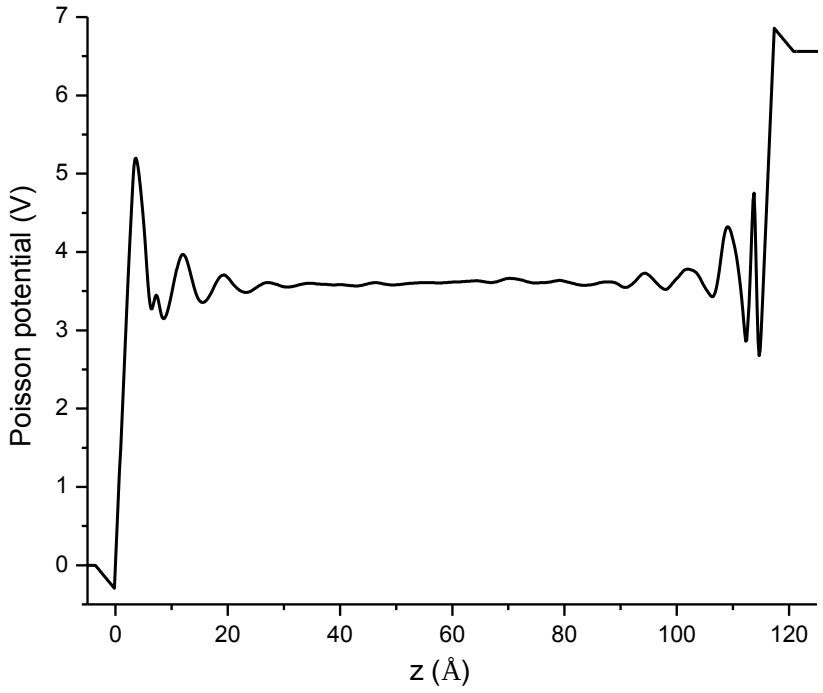

Figure 6-5. Poisson potential as a function of position relative to the electrode surface for the neat electrolyte at $\Delta V = 6$ V.

Figure 6-6. Ion center of mass density as a function of distance in Z-axis for neat electrolyte at ΔV=0 V (a) and ΔV=6 V (b), 20% EC at ΔV=0 V (c) and ΔV=6 V (d), and 20% ACN at ΔV=0 V (e) and ΔV=6 V (f).

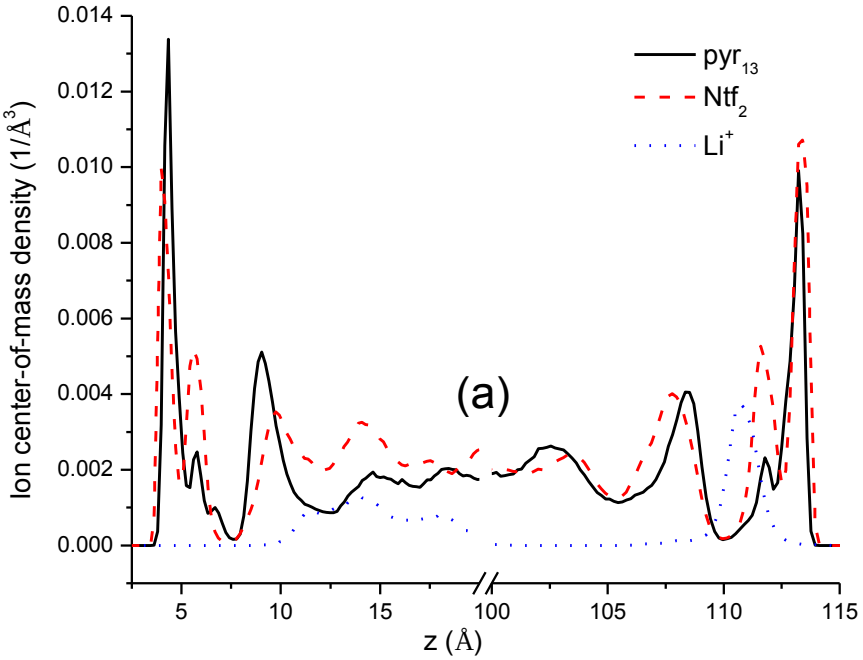
0.014
0.012
0.010
0.008
0.006
0.004
0.002
0.000
Ion center-of-mass density (1/Å^3)
pyr$_{13}$
Ntf$_2$
Li$^+$
(a)
5
10
15
100
105
110
115
z (Å)

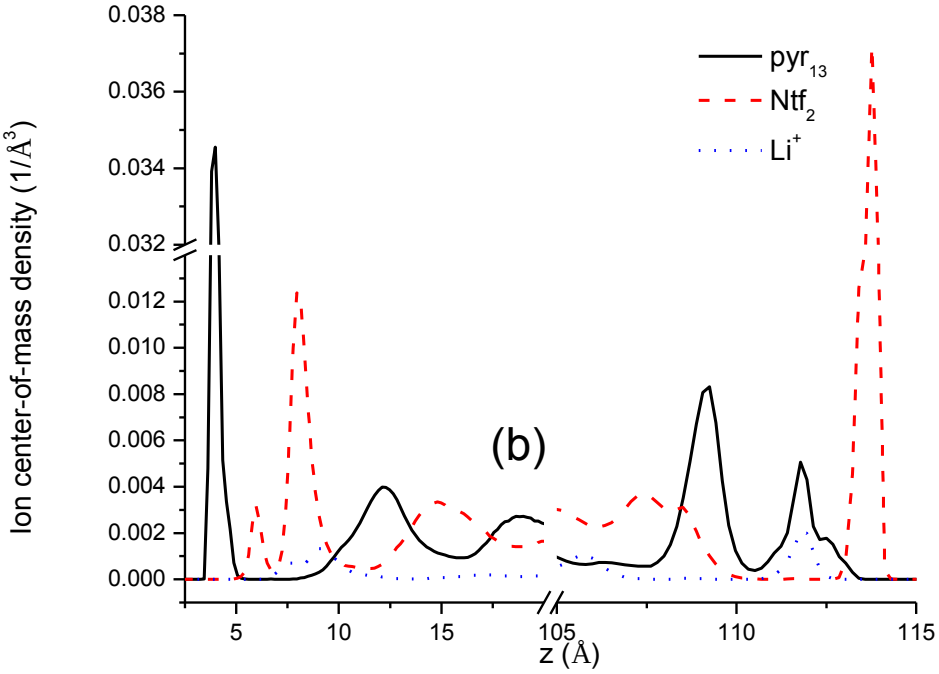
0.038
0.036
0.034
0.032
0.012
0.010
0.008
0.006
0.004
0.002
0.000
Ion center-of-mass density (1/Å^3)
pyr$_{13}$
Ntf$_2$
Li$^+$
(b)
5
10
15
105
110
115
z (Å)

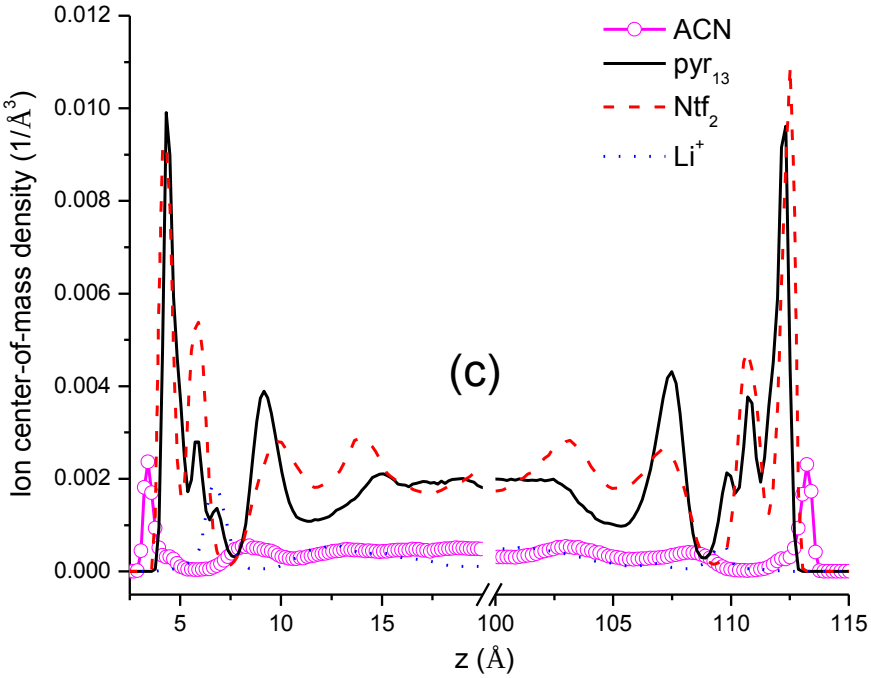
0.012
0.010
0.008
0.006
0.004
0.002
0.000
Ion center-of-mass density (1/Å^3)
ACN
pyr$_{13}$
Ntf$_2$
Li$^+$
(c)
5
10
15
100
105
110
115
z (Å)

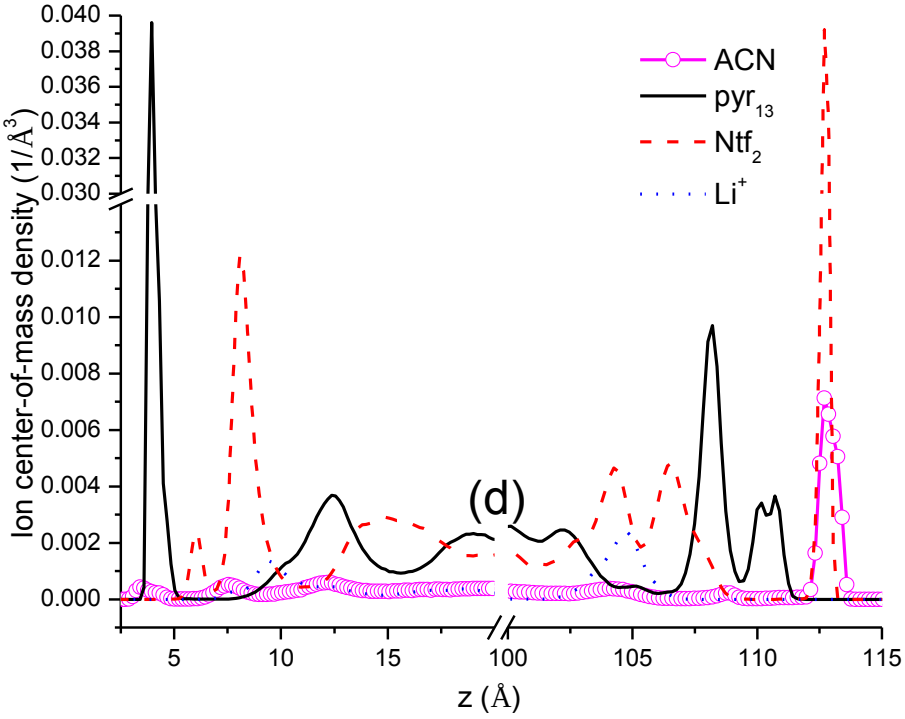
0.040
0.038
0.036
0.034
0.032
0.030
0.012
0.010
0.008
0.006
0.004
0.002
0.000
Ion center-of-mass density (1/Å^3)
ACN
pyr$_{13}$
Ntf$_2$
Li$^+$
(d)
5
10
15
100
105
110
115
z (Å)

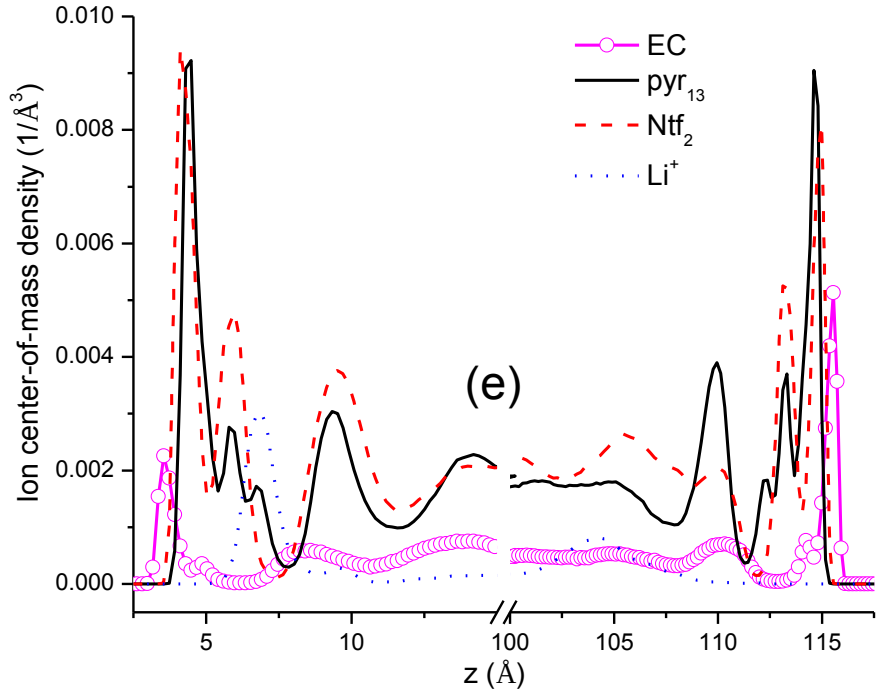
0.010
0.008
0.006
0.004
0.002
0.000
Ion center-of-mass density (1/Å^3)
EC
pyr$_{13}$
Ntf$_2$
Li$^+$
(e)
5
10
100
105
110
115
z (Å)

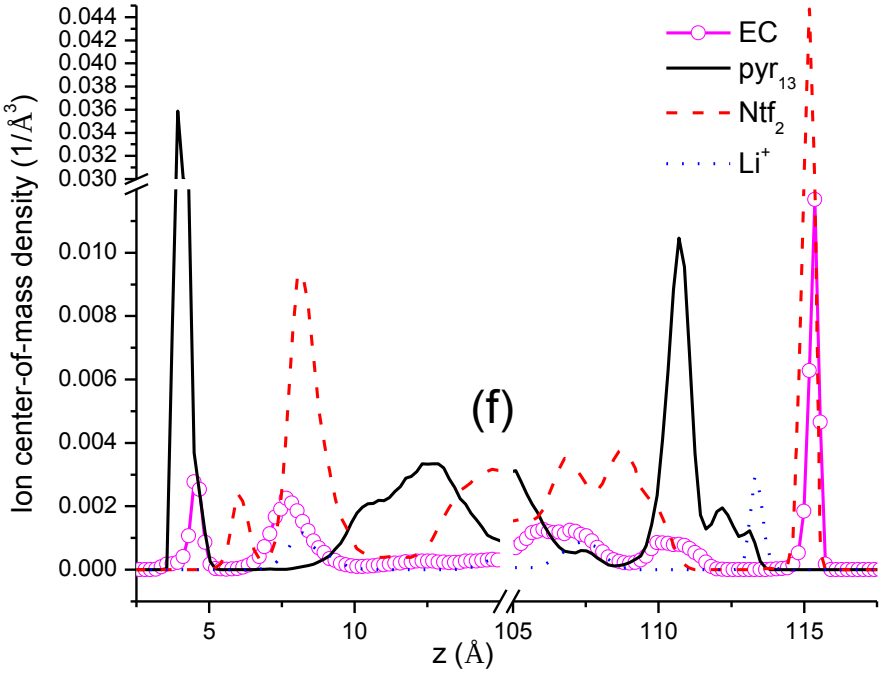
0.044
0.042
0.040
0.038
0.036
0.034
0.032
0.030
0.010
0.008
0.006
0.004
0.002
0.000
Ion center-of-mass density (1/Å^3)
EC
pyr$_{13}$
Ntf$_2$
Li$^+$
(f)
5
10
105
110
115
z (Å)

solvents, EC and ACN, are included in the electrolyte, it is interest to see the uncharged surfaces are more closely approached by those diluents. At sufficiently large potentials,when electrostatic interactions dominate, a layer of the negative ion (Ntf_2) and the positive ion (pyr_{13}) are found next to the positive and negative electrodes, respectively. The neutral diluents are, surprisingly, found to be rich in the first layers near positive electrode (anode) at the same distance as anions. The ability of organic solvents molecules to mostly closely accumulate near the anode well explains the formation of stable SEI layers in experiments when organic solvents were added into the ionic liquids electrolyte.[3,4,7] At 0 V potential, the density profiles of the components are expect to be symmetric at the two electrodes. Thus, the unsymmetrical density profile of Li^+ shown in Figure 6-6 indicates that the systems need to run much longer time. Considering the difference in self-diffusion coefficients and densities of ions, about 7 times longer production run than previous simulated systems[11] is expected in order to get a completely symmetric density profile for the Li^+. Therefore, at this moment we cannot comment the behavior of Li cations near the uncharged surface. In contrast to the observation that Li^+ cations in carbonates/ $LiPF_6$ mixtures are found most closely accumulated at the negative surface more negative than -2 V,[11] in ILEs Li^+ cations are not able to closely approach the negatively charged electrode surface, even at ΔV=6 V (electrode potential = $\pm$ 3 V). The density peaks for Li^+ is actually found in the layer rich of Ntf_2 anions because of the strong correlation between O(Ntf_2) atoms and Li^+ which restricts the Li^+ moving to the negative surface. In addition, as discussed in Chapter 4 the mobility of the ions in bulk electrolyte follow the order pyr_{13} > Ntf_2 > Li^+, therefore, a fast accumulation of pyr_{13} cations at the negative electrode will “screen out” the Li^+ from approaching the electrode.

At positive electrode, a relatively high concentration of Li^+ is also observed just next to the Ntf_2 layer closest to the surface. This behavior is consistent with what observed in carbonates/$LiPF_6$ mixtures near graphite electrode[11] and it is due to the structuring of the anions in the surface layers. The highly structured Ntf_2 anions with oxygen atoms oriented largely toward the surface[10(c)] has a reduced ability to coordinate Li^+ cations within the inner part of the surface layer (< 7.5 Å). Those oxygen atoms pointing away from the surface, in contrast, can rapidly coordinate Li^+ cations, leading to a Li^+ density peak next to the Ntf_2 layer. The pyr_{13} and Ntf_2 layer near the electrode means increased energy barrier for Li^+ intercalation/deintercalation. The inability of Li^+ cations to reach the electrode surface is fatal for the performance of lithium ion batteries in which Li^+ intercalation-deintercalation process is the key in the operation of the batteries. We believe the poor electrochemical performance and inability of graphite electrodes to reversibly cycle lithium observed in experimental studies of a similar ILEs $[pyr_{14}][Ntf_2]$/$[Li][Ntf_2]$[15,16] are due to the fact that Li^+ cations are not able to reach the graphite surface.

The electric double layer can be better understood by examination of the charge density near the electrode surface. Since the lithium salt concentration is very low, we expect that the Li^+ has very limited influence on the charge density profiles. Figure 6-7 shows charge density q(z) and cumulative charge near the electrode for the systems at ΔV= 0 V and ΔV= 6 V. As can be seen, inclusion of organic solvents does not change the charge densities profile obviously, indicating that the organic solvents have limited influence on the structure of multilayers. The oscillation in q(z) near the electrode should necessarily correspond to the oscillations in the atom densities shown in Figure 6-8. At

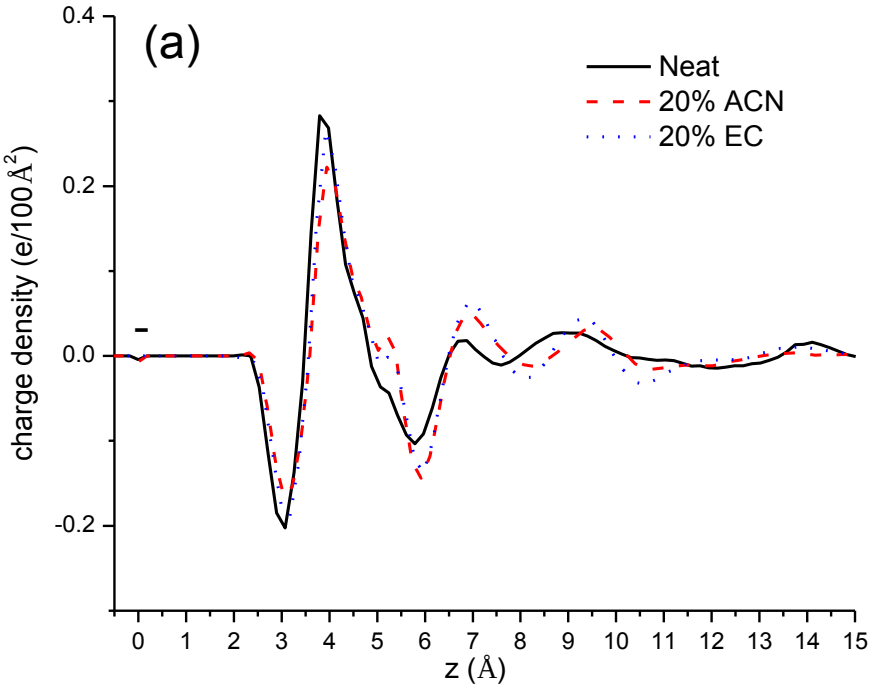

Figure 6-7. Charge density at ΔV = 0 V (a) and ΔV = 6 V (b), (c), and cumulative charge at ΔV = 0 V (d) and ΔV = 6 V (e) as a function of position relative to the electrode. The signs - and + indicted on the plot indicate the charge sign on the electrode.

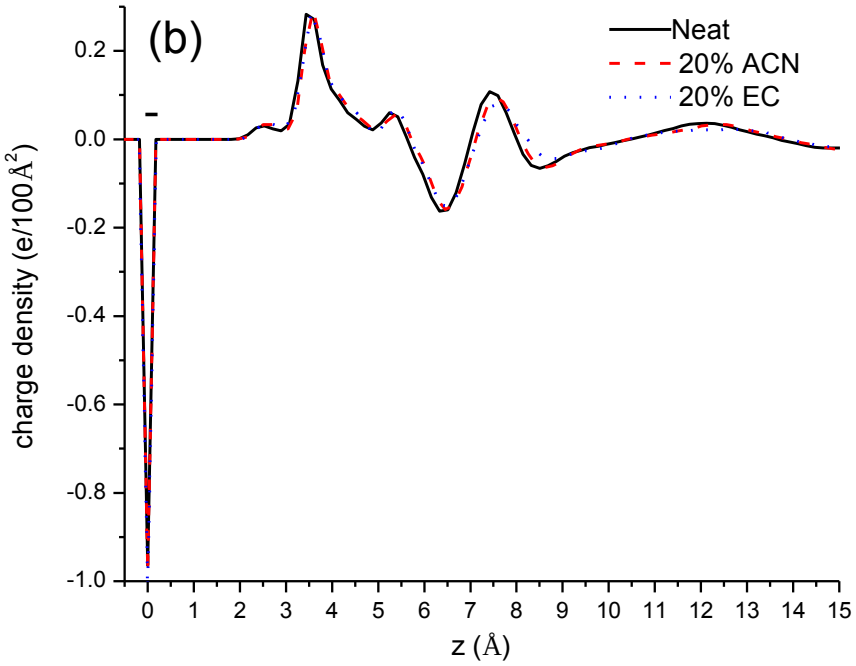

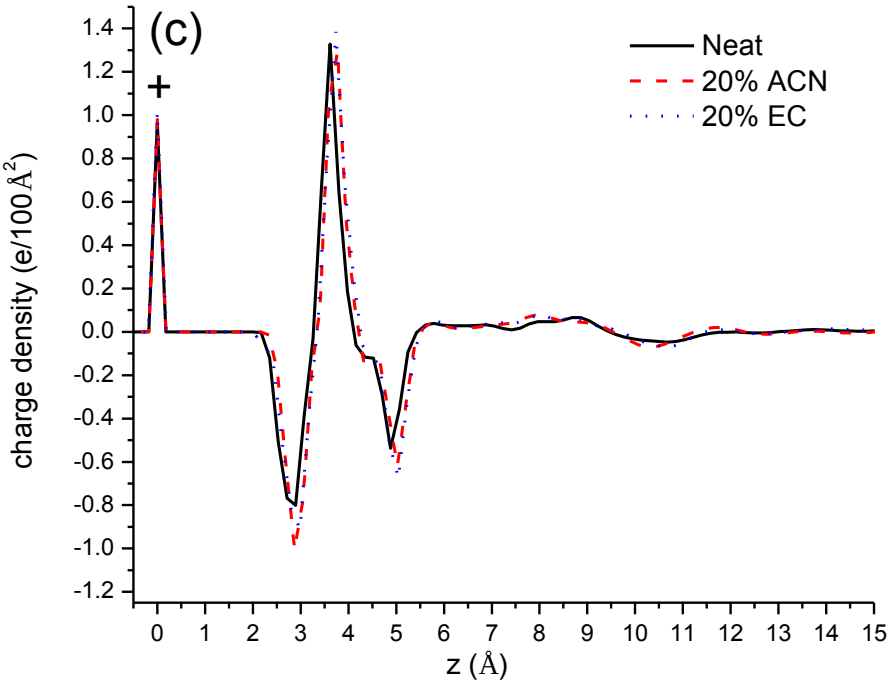

Figure 6-7. Continued

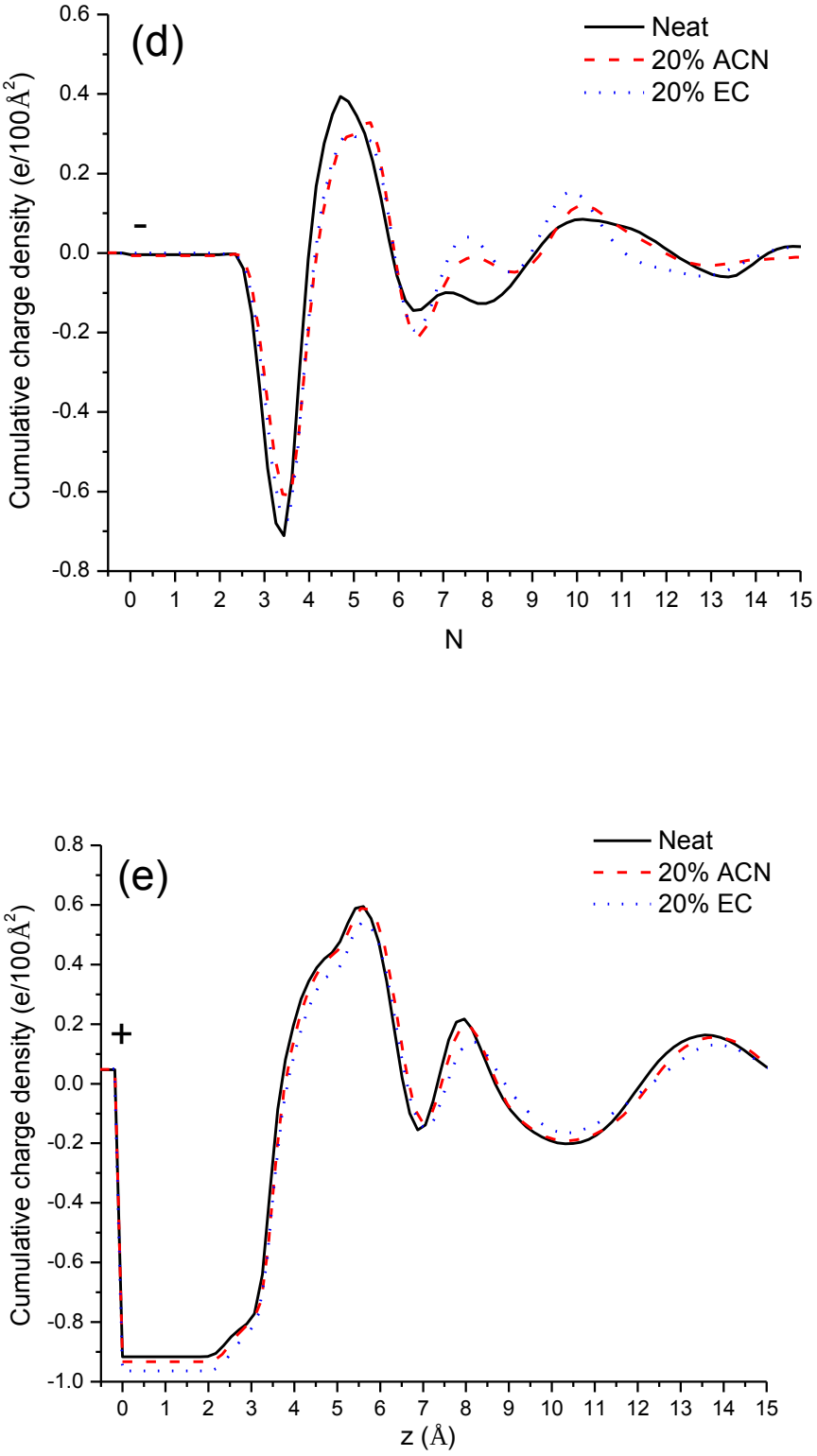

Figure 6-7. Continued

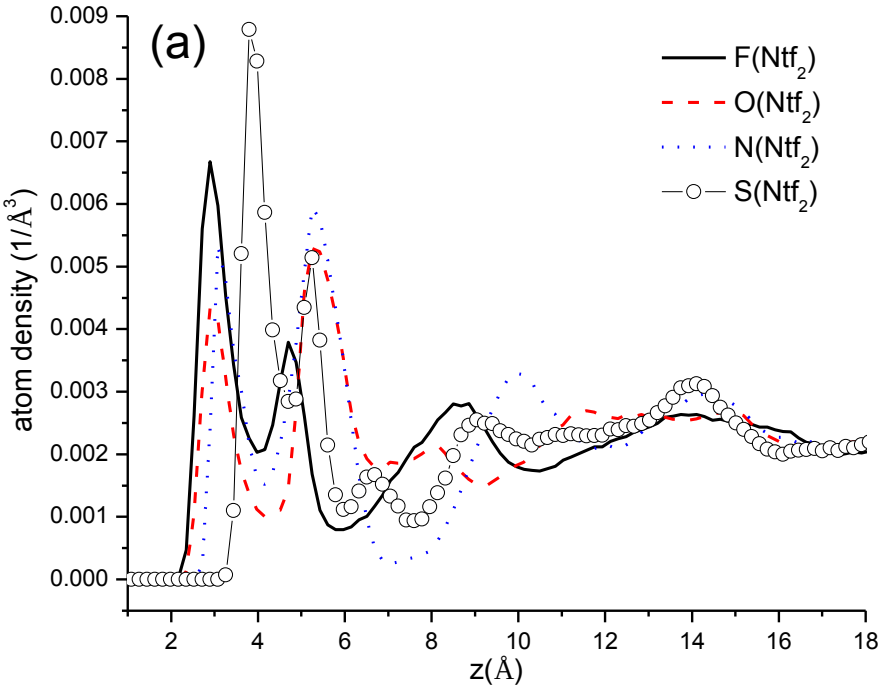

Figure 6-8. Atom densities as a function of distance from electrodes for Neat electrolyte at ΔV=0 V (a) (b), and at ΔV=6 V (c) (d). The signs - and + indicted on the plot indicate the charge sign on the electrode.

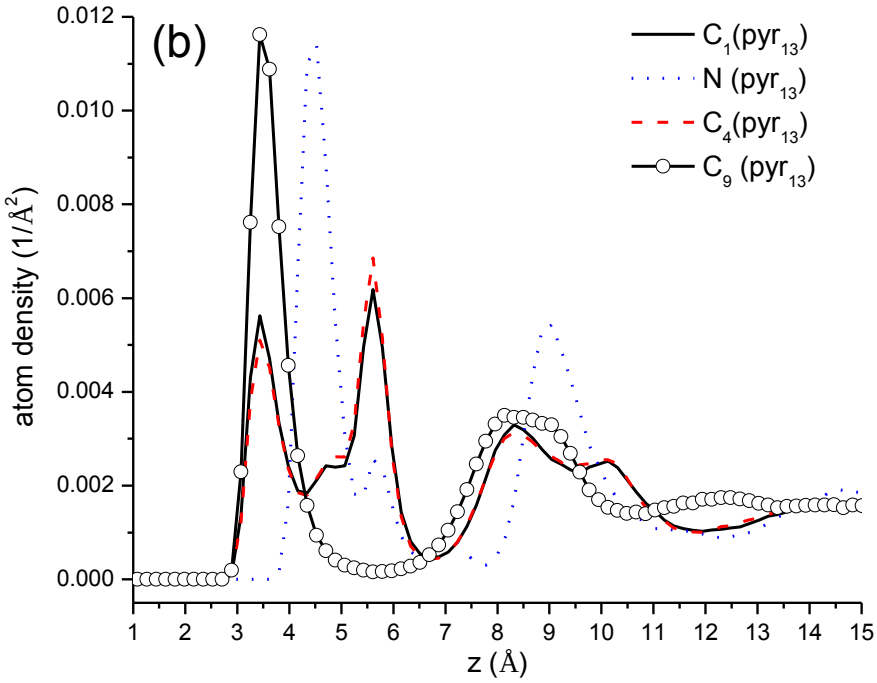

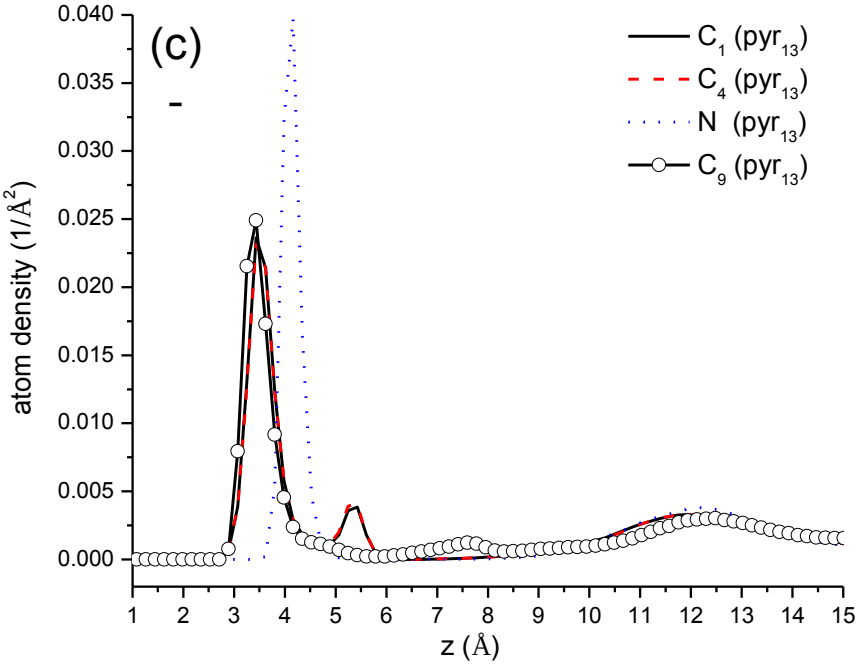

Figure 6-8. Continued

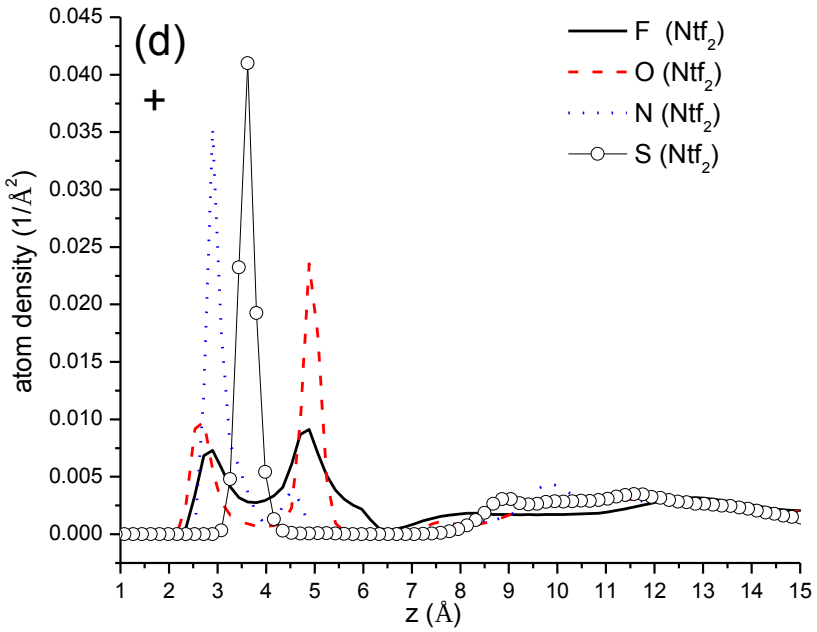

Figure 6-8. Continued

$\Delta V = 0$ V, the first negative peak near the electrode surface appears at about 3 Å, the same position where the negatively charged F and O atoms from Ntf_2 are found, as shown in Figure 6-8. The next positive peak has contribution mainly from S atoms in the Ntf_2 anions. The larger affinity of the uncharged graphite surface for the O and F of Ntf_2 was also observed in simulations of graphite confined $[C_nmim][Ntf_2]$[17] and $[pyr_{13}][Ntf_2]$.[10(c)] At $\Delta V = 6$ V, since pyr_{13} cations and Ntf_2 aions accumulate near the negative and positive electrode, respectively, a positive peak and a negative peak are observed near the two electrodes as shown in Figure 6-7b and 6-7c. The charge oscillations within the multilayer in ILEs can be qualitatively understood by "Overscreening" effect.[14] Figure 6-7e shows that the negative electrode has an accumulated charge around - 0.9 e/100 $Å^2$. Slightly increased values are observed for the organic containing systems. The cumulative charge reaches about + 0.6 e/100 $Å^2$ in the inner layer, indicating that there are more than 'needed' positive charges in the first layer to screen the effects of charges in electrode. This net positive charge is then responsible for the formation of a second layer with more than needed negative charges to screen the first layer. This successive "overscreening" mechanism continues with decreasing magnitude until finally there is no accumulative charge. The "overscreening" effect is also observed near uncharged surface as shown in Figure 6-7d.

It is interesting to look at the orientation of ions near the charged and uncharged surface. Here we define the direction of cations as the vector pointing from the center of the C-C bond to the N atom, and that of anions as the vector connecting the C atoms (Figure 6-9d). In previous MD simulations of graphite confined [pyr13][Ntf2],[10(c)] the anions adjacent to the surface were found to be mostly perpendicular to the uncharged

electrode surfaces and preferentially parallel to the highly charged negative surface. The pyr_{13} cations were found perpendicular to the uncharged electrode surface and changed their orientations while the electrode potentials increasingly negative. A scheme illustrating ion orientations is shown in Figure 6-9d. Using an all atom polarizable force field, however, we observed in the present work that perpendicular arrangement of Ntf_2 are no longer the preferred orientation near the uncharged surface, as evidenced by the two comparable maximums in the first peak of $N(Ntf_2)$ atom density shown in Figure 6-8a and snapshots in Figure 6-9. The first maximum of $N(Ntf_2)$ atom density has contribution mainly from Ntf_2 parallel to the surface and the second one are from those perpendicular to the surface. As to the pyr_{13} cations, we notice that the first maximum in $N(pyr_{13})$ atom density is significantly higher than the second one, indicating that the cations preferentially parallel to the uncharged surface. The positions of first peaks in densities profiles for C1, C4 and C9 atoms in pyr_{13} (Figure 6-1) appear at the same distance as the first maximum in $N(pyr_{13})$ atom density indicates that pyr_{13} ring tends to be parallel to the uncharged surface. An examination of the atom densities in $\Delta V = 6$ V systems (Figure 6-8c) shows that all pyr_{13} cations tend to be parallel to the highly negatively charged surface with only a small amount of rings perpendicular to the surface. Increase of first maximum and the decrease of second maximum in the $N(Ntf_2)$ atom density (Figure 6-8d) indicates that the Ntf_2 anions are preferentially parallel to the positively charged surface.

Figure 6-10 shows comparisons of the $N(Ntf_2)$ and $N(pyr_{13})$ in Neat, 20% ACN, and 20% EC at ΔV=0 V. Involving of EC does not influence the orientation of anions near the uncharged surface but ACN molecules slightly increase the number of anions

perpendicular to the uncharged surface and reduce the number of anions parallel to the uncharged surface. Near highly charged electrode surface, ACN molecules are found to accumulate near the positive electrode but EC are found near both electrodes as shown in the ion center-of-mass density profiles (Figure 6-6) and the snapshots (Figure 6-9). Figure 6-6 shows that the density of pyr_{13} near highly positively charged surface changes dramatically when organic solvents were added, thus it would be interesting to compare the N(pyr_{13}) atom density profiles in Neat and diluted systems near positive electrodes. Figure 6-11 shows that within 7.5 Å the number of N(pyr_{13}) atoms decreased when the organic solvents were added into the electrolytes with more reduction observed in EC containing system. The number of the N(pyr_{13}) atoms, and hence that of cations, in the layer between 7.5 Å and 10 Å however increased in corresponding to the reduction within 7.5 Å, indicating that the organic solvents molecules pushed away the pyr_{13} cations in the first layers into the second layers near positive electrodes. In addition, Figure 6-5 indicates that the Ntf_2 density near the positive electrode increased slightly as organic solvents were involved, leading to a much denser Ntf_2 layer with less space for more pyr_{13} cations.

6.4. Conclusion

Using an electroactive interface methodology, atomic MD simulations of $[pyr_{13}][Ntf_2]$/[Li][Ntf_2]/organic solvents mixtures in contact with uncharged and charged flat graphite electrodes have allowed us to reveal the behavior of ions and organic solvents near electrode surfaces. Even at zero potential, a tendency of the electrolyte to become highly structured at the electrode interface is observed in our simulations. Organic solvents are found to closely accumulate near the anode, enabling the formation

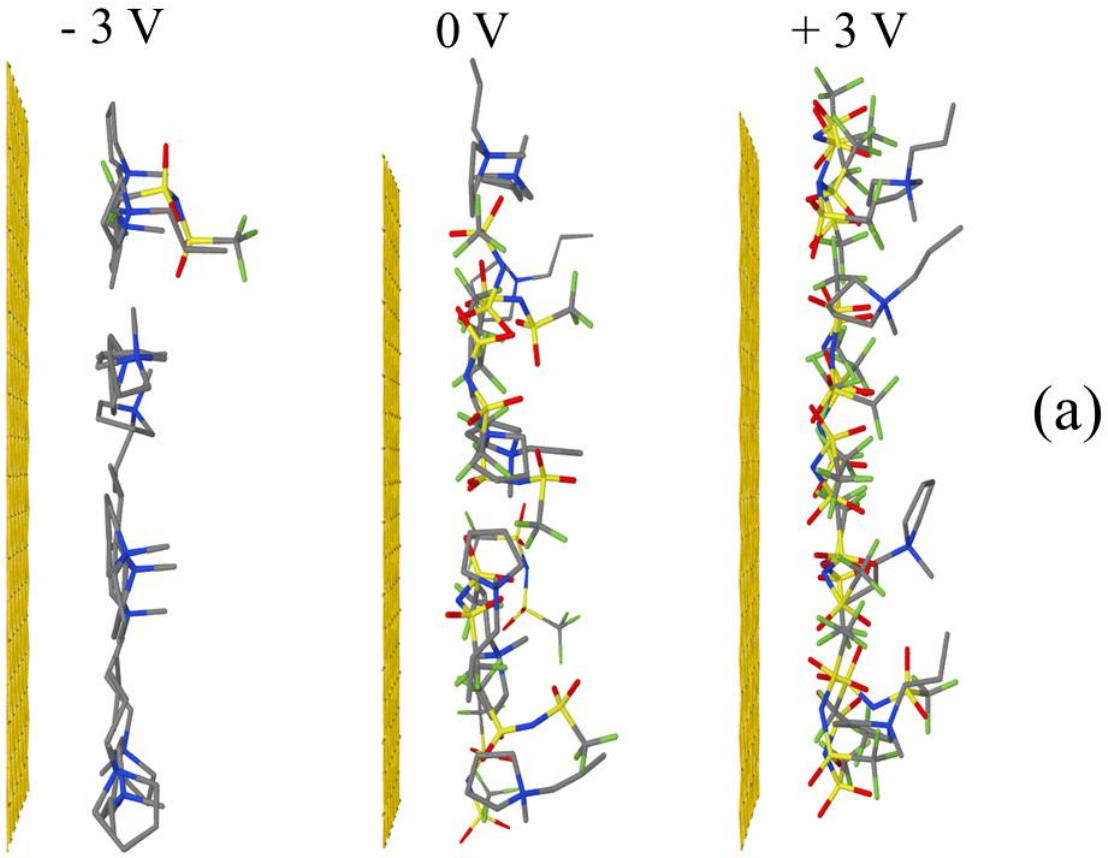

Figure 6-9. Snapshot images of ions near the electrode (<7.5 Å) at different potentials for Neat (a), 20% ACN (b) 20% EC (c). Organic solvents molecules are shown in a larger size.

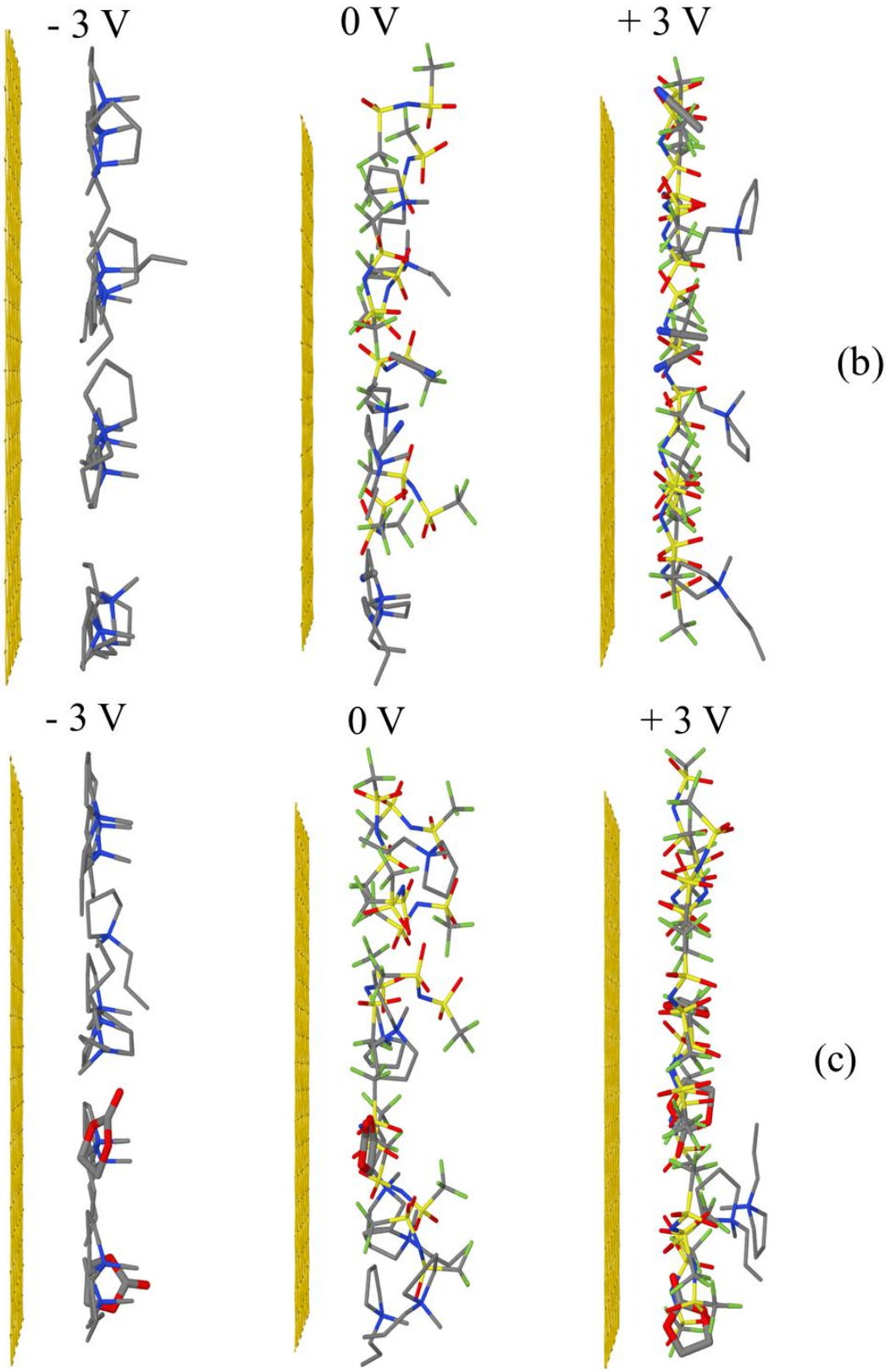

Figure 6-9. Continued

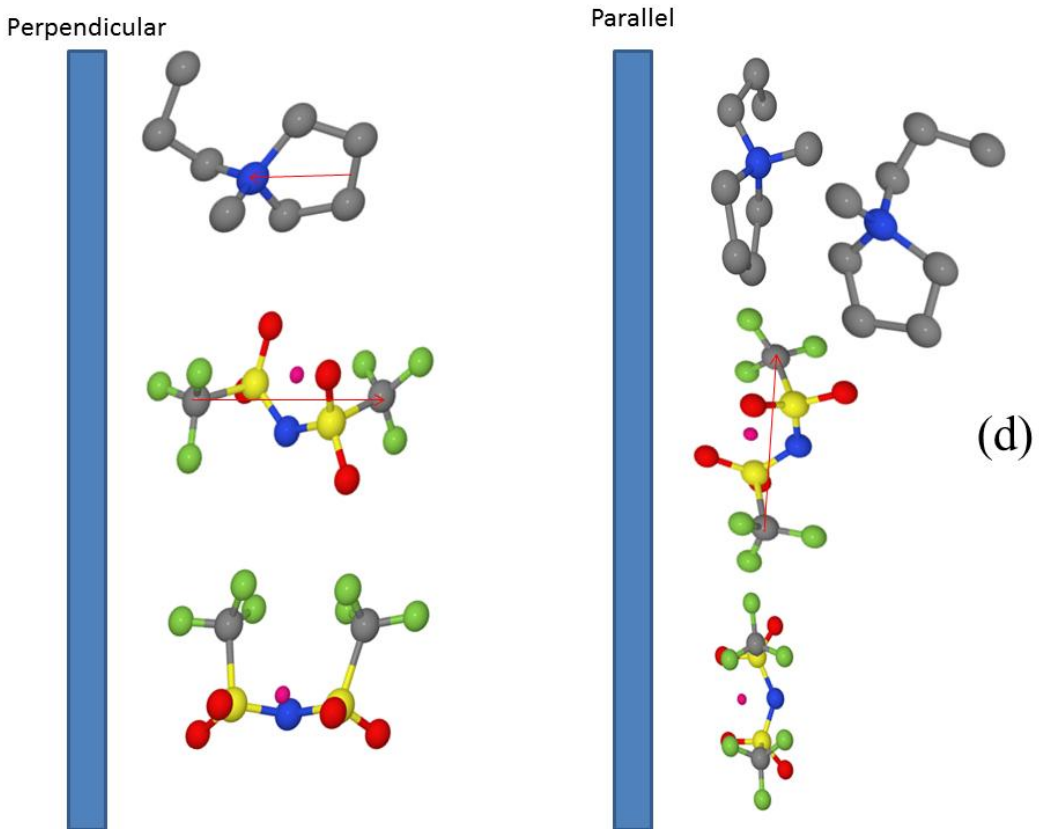

Figure 6-9. Continued

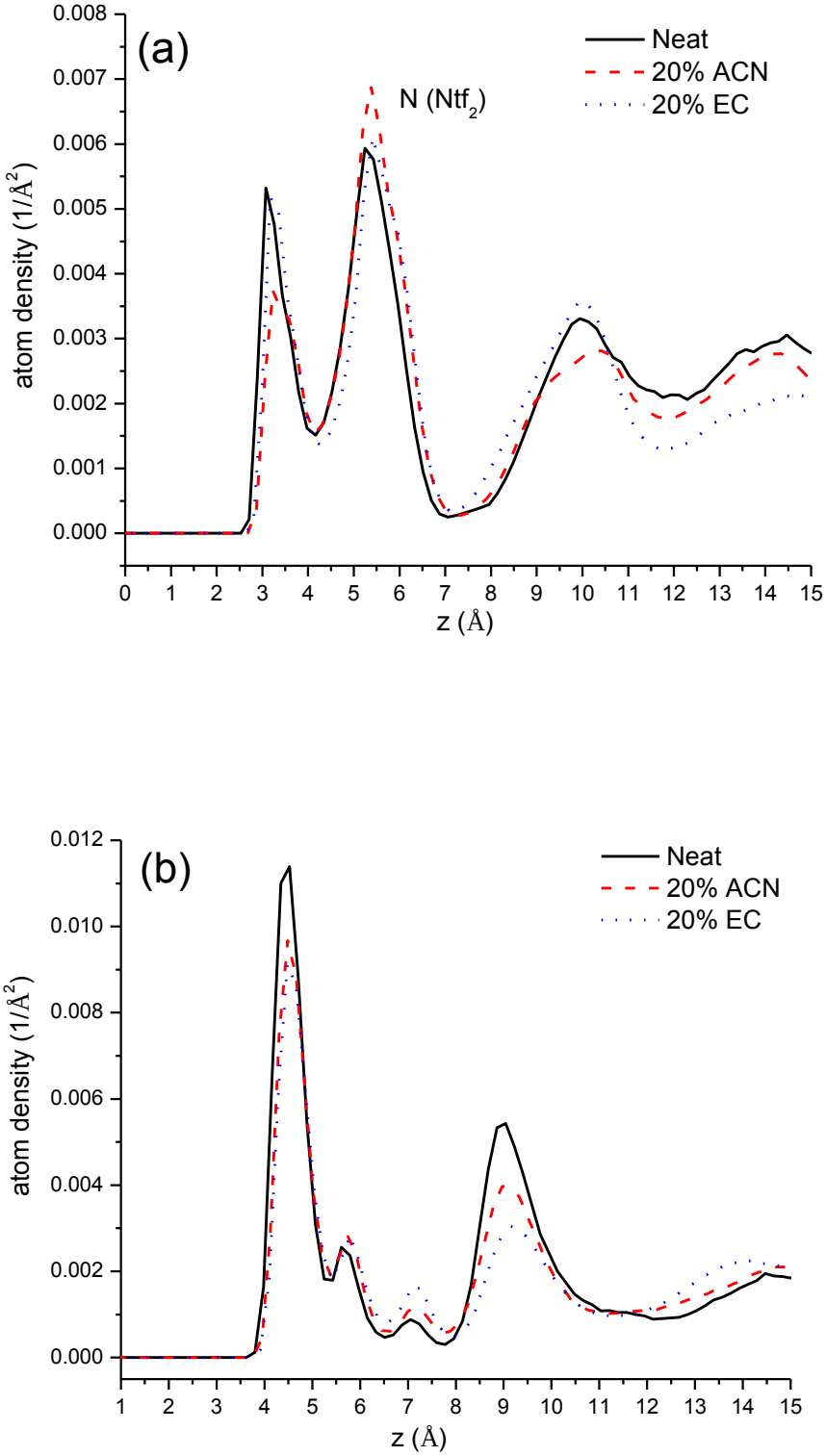

Figure 6-10. Comparison of atom densities as a function of distance in Z-axis for N (Ntf_2) (a) and N (pyr_{13}) (b) in Neat, 20% ACN, and 20% EC at ΔV=0 V.

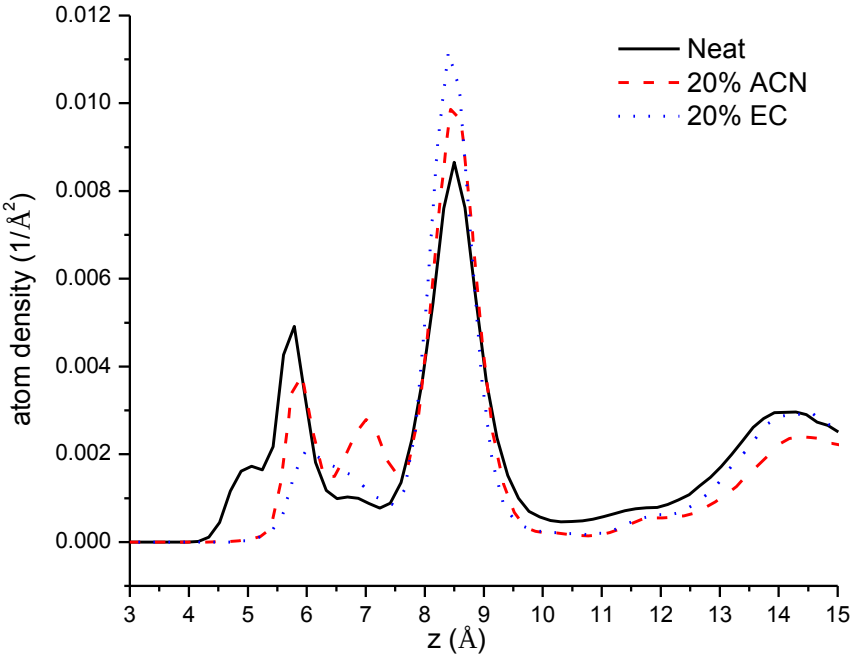

Figure 6-11. Comparison of N(pyr_{13}) atom densities near the positive electrode surface in Neat, 20% ACN and 20% EC electrolytes at ΔV=6 V.

of passive SEI layers which protect the ILEs from further decomposition. The anion orientation near uncharged surface in the [Li][Ntf_2] doped [pyr_{13}][Ntf_2] IL are found to be different in pure [pyr_{13}][Ntf_2] IL. About half of the anions near the surface are found to be parallel in the mixtures while most are tend to be perpendicular to the surface in pure ILs. When ionic liquid exists, Li^+ cations need to overcome an increased energy barrier in order to intercalate into the electrode surface. This would be a deadly hammer to the application of ILEs in lithium ion batteries.

6.5. References

(1) Bayley, P. M.; Lane, G. H.; Rocher, N. M.; Clare, B. R.; Best, A. S.; MacFarlane, D. R.; Forsyth, M. *Phys. Chem. Chem. Phys.* **2009**, 11, 7202.

(2) Bayley, P. M.; Best, A. S.; MacFarlane, D. R.; Forsyth, M. Phys. Chem. Chem. Phys. **2011**, 13, 4632.

(3) Katayama, Y.; Yukumoto, M.; Miura, T. *Electrochem. Solid-State Lett.* **2003**, 6(5), A96.

(4) Guerfi, A.; Dontigny, M.; Charest, P.; Petitclerc, M.; Lagacé, M.; Vijh, A.; Zaghib, K. *J. Power Sources* **2010**, 195, 845.

(5) Goodenough, J. B.; Kim, Y. *Chem. Mater.* **2010**, 22, 587.

(6) Von Cresce, A.; Xu, K. *Electrochem. Solid-State Lett.* **2011**, 14, A154.

(7) Xu, K.; von Cresce, A. U. *Langmuir* **2011**, 26, 11538.

(8) Mancini, M.; Nobili, F.; Dsoke, S.; D'Amico, F.; Tossici, R.; Croce, F.; Marassi, R. *J. Power Sources* **2009**, 190, 141.

(9) Smith, G. D.; Borodin, O.; Russo, S. P.; Rees, R. J.; Hollenkamp, A. F. *Phys. Chem. Chem. Phys.* **2009**, 11, 9884.

(10) (a) Vatamanu, J,; Borodin, O.; Smith, G. D. *J. Phys. Chem. B* **2011**, 115,3073; (b) Vatamanu, J.; Cao, L.; Borodin, O.; Bedrov, D.; Smith, G. D. *J. Phys. Chem. Lett.* **2011**, 2, 2267; (c) Vatamanu, J.; Borodin, O.; Smith, G. D.; Smith, G. D. *J. Am. Chem. Soc.* **2010**, 132, 14825; (d) Borodin, O.; Vatamanu, J.; Smith, G. D. *ECS Trans.* **2010**, 33, 583; (e) Georgi, N.; Kornyshev, A. A.; Fedorov, M. V. *J. Electroanal. Chem.* **2010**, 649, 261.

(11) Vatamanu, J.; Borodin, O.; Smith, G. D. *J. Phys. Chem. C* **2012**, 116 1114.

(12) Hoover, W. G. *Phys. Rev. A* **1985**, 31, 1695.

(13) Martynov, G. A.; *Fundamental Therogy of Liquids: Methods of Distribution Functions*, Adam Hilger, Philadelphia, **1992**.

(14) Vatamanu, J.; Borodin, O.; Smith, G. D. *Phys. Chem. Chem. Phys.* **2010**, 12, 170.

(15) Appetecchi, G. B.; Montanino, M.; Balducci, A.' Lux, S. F.; Winterb, M.; Passerini, S. *J. Power Sources* **2009**, 192, 599.

(16) Nádherná, M.; Reiter, J.; Moškon, J.; Dominko, R. *J. Power Sources* **2011**, 196, 7700.

(17) Vatamanu, J.; Borodin, O.; Bedrov, D.; Smith, G. D. *J. Phys. Chem. C* **2012**, 116, 7940.

CHAPTER 7

CONCLUSION

Using a recently developed polarizable force field, molecular dynamics simulations of ionic liquids and the ionic liquids/lithium salt and or organic solvent mixtures have been successfully studied. Comparison of results from MD simulations using polarizable and nonpolarizable models indicates again the nonpolarizable force field is not sufficient for simulations of ionic liquids. Incorporation of polarization in the force field is required for accurate prediction of the ILs properties, in particular, the transport properties. The properties of ionic liquids doped with lithium salt are thoroughly investigated by MD simulations. Excellent agreement between simulations and experiments indicates that MD simulations using the APPLE&P force field are powerful tool in investigation of ILEs. The structures of lithium coordination shell at different salt concentrations are elucidated in this dissertation. In addition, our simulations reveal that lithium salt doped ionic liquids have unusual dynamics that strongly depends on the doping level. A significant but unfortunate decrease in transport properties of all the ions in the systems are noticed upon the addition of lithium salt to the ionic liquid electrolytes. The lithium conductivity is observed not necessarily increase but reach a maximum as the lithium concentration increasing. Those observations may help in finding out the appropriate salt concentration for ionic liquid based lithium ion batteries. Incorporation of proper amount of organic

solvent is shown to be a potential way to modify the transport properties of ions in lithium doped ILs. When organic solvents EC and ACN are added into the lithium doped ILs the ion mobility is encouragingly enhanced with the most improvement in Li^+ cation, leading to higher conductivity in the diluted ILEs. Influence of the organic solvents on the structure of the ILEs is also investigated carefully in order to uncover the changes in Li^+ diffusion mechanisms. The selected organic solvents demonstrate their ability to change the Li^+ coordination by, at some degree, breaking the Li^+ - Ntf_2 correlation and coordinating to Li^+ together with the anions. The structure diffusion in the diluted electrolytes, therefore, contributes more to the Li^+ diffusion than in the undiluted ones. The structure and behavior of electrolytes near the electrode surface are significantly different from the bulk. Multilayer structures near the charged and highly charged graphite surface are thoroughly explored by MD simulations in this dissertation. The orientations of ions near the surface in lithium doped ILs are found to differ significantly from the pure ILs. Organic solvents accumulate most closely to the graphite surface which is believed to benefit the ionic liquids base lithium ion batteries since the decomposition or the organic solvent will form a stable SEI layer which ultimately protect the ionic liquids from further decomposition. MD simulations also reveal that a layer of organic ions near the electrode surface results in increased the energy barrier for Li^+ to reach the surface. This newly observed drawback of ILE may make implementation of ILEs in lithium ion batteries more challengeable.